SIMULATION OF ATOMISTIC PROCESSES DURING SILICON OXIDATION

THÈSE N^{O} 2788 (2003)

PRÉSENTÉE À LA FACULTÉ DES SCIENCES DE BASE

Institut de théorie des phénomènes physiques

SECTION DE PHYSIQUE

ÉCOLE POLYTECHNIQUE FÉDÉRALE DE LAUSANNE

POUR L'OBTENTION DU GRADE DE DOCTEUR ÈS SCIENCES

PAR

Angelo BONGIORNO

laurea di dottore in fisica, Università degli Studi di Milano, Italie
et de nationalité italienne

acceptée sur proposition du jury:

Prof. A. Pasquarello, directeur de thèse
Prof. A. Baldereschi, rapporteur
Prof. L. Forro, rapporteur
Dr M. Hybertsen, rapporteur
Prof. M. Stoneham, rapporteur

Lausanne, EPFL
2003

Contents

Version abrégée

Les couches minces de dioxyde de silicium (SiO_2) sur substrat de silicium monocrystallin (Si) forment les oxydes de portail dans les transistors ultramodernes basés sur le silicium. La compréhension *à l'échelle atomique* du processus d'oxydation du Si et de les propriétés de l'interface Si(100)-SiO_2 sont d'importance significative pour l'industrie microélectronique. Dans cette thèse, nous étudions ces deux sujets intimement couplés en utilisant principalement des calculs *ab initio*.

Nous commençons par considérer la structure de l'interface Si(100)-SiO_2. Des modèles atomique de l'interface sont construits en tenant compte de la densité des défauts de coordination, de la quantité et emplacement des atomes de Si partiellement oxydés, et du profil de densité de masse, comme obtenu par les expériences. Comme résultat nous obtenons un assortiment de modèles differantes par le degré de complexité dans la région de transition à l'interface Si(100)-SiO_2. Les propriétés de la structure de transition à l'interface sont examinées en interprétant des expériences de dispersion des ions d'hélium (He^+). En particulier, nous nous référons à une nouvelle série de mesures exécuté pour atteindre le maximum de sensibilité aux déplacements du substrat de Si à l'interface. Pour interpréter ces données expérimentales, nous exécutons des simulations de la dispersion des ions He^+ sur une série choisie de modèles de l'interface qui possèdent des caractéristiques structurales differentes dans la région de transition. Nous trouvons que des déplacements plus grands que 0.09 Å se propagent sur trois couches dans le substrat de Si. La structure de transition conforme à ces déformations inclut des dimers Si-Si parallèles à l'interface, des protrusions de O, et/ou une distribution désordonnée de liens à l'interface. Une structure de transition avec une distribution régulière des unités Si-O-Si à l'interface est en contradiction avec les expériences.

Le processus d'oxydation du silicium est approché en considérant la croissance de films d'oxyde épais. Dans ce régime, l'oxydation est limitée par la diffusion de l'espèce oxydante. Dans cette étude nous fournissons une description à l'échelle atomique de la migration d'oxygène à longue portée dans l'oxyde. La molécule O_2 est identifiée comme l'espèce oxydante qui diffuse à travers les interstices du réseau sans échanger

les atomes d'oxygène avec la matrice. L'énergie d'activation associée à la diffusion est trouvée en accord avec les valeurs expérimentales. Ces résultats nous mènent à étudier le taux de diffusion à travers une couche mince d'oxyde à l'interface. En particulier, nous examinons l'effet combiné d'un mécanisme de diffusion percolative et d'une couche d'oxyde dense localisée proche du substrat de Si. Nous trouvons que quand une couche mince d'oxyde dense se trouve à l'interface, pour des épaisseurs de l'oxyde plus grandes que 2 nm, le taux de diffusion de l'oxygène tombe au dessous de la valeur trouvée dans la SiO_2. Ces résultats soutiennent le modèle *blocking layer* introduit pour expliquer l'échec du modèle de Deal and Grove pour la description de la croissance de couches d'oxyde minces.

Finalement, les mécanismes responsables de l'oxydation à l'interface Si(100)-SiO_2 sont examinés. Ceci est examiné en deux étapes. Dans la première étape, nous étudions les propriétés des espèces d'oxygène chargées négativement dans le SiO_2. Nous comparons l'énergie de la molécule d'oxygène neutre avec celle des espèces négatives, soit dans l'état atomique soit dans moléculaire. Les propriétés énergiques et de dissociation de l'espèces O_2^- et O_2^{2-} sont aussi considérées. Nous trouvons que dans la SiO_2 les espèces d'oxygène négatives sont incorporées dans le réseau d'oxyde en exigeant des déformations significatives du réseau. L'investigation du processus de dissociation de l'espèce d'oxygène moléculaire négativement chargée souligne la dépendance des énergies de dissociation de la nature désordonnée du réseau et de la charge portée par la molécule. Dans une deuxième étape, nous etudions les réactions de l'oxygène à l'interface. Nous considérons la molécule O_2 neutre et les espèces moléculaire chargées négativement O_2^- et O_2^{2-}. Dans le cas de la molécule neutre, nous examinons aussi les effets du spin. Pour toutes ces espèces, nous étudions de façon séquentielle l'incorporation dans le réseau et la dissociation en espèces atomiques. Nous trouvons que à l' interface Si(100)-SiO_2 toutes ces espèces sont incorporées dans le réseau ou spontanément, ou en traversant des petites barrières d'énergie. À proximité de l'interface, la molécule neutre O_2 attaque et pénètre dans les liens Si-Si. Ce processus est favorisé par le transfert de charge des liens de Si-Si à l'espèce moléculaire. La molécule dans l'état de spin de triplet est incorporée préférentiellement dans le réseau en correspondance de la couche supérieure du substrat de Si. Les espèces chargées négativement sont incorporées spontanément dans n'importe quel lien Si-Si de l'oxyde, et n'importe quelle distance de l'interface. Leur incorporation est souvent associée à la formation de défauts, confirmant leur capacité de modifier le réseau d'oxyde. La dissociation et par conséquent l'oxydation de liens de Si-Si est spontanée, étant associé à des barrières d'énergie négligeables qui peuvent être traversés grâce à l'énergie gagnée pendant le processus d'incorporation. Ces résultats sont conformes à un assortiment d'observations expérimentales.

Abstract

Silicon dioxide (SiO_2) films grown on silicon monocrystal (Si) substrates form the gate oxides in current Si-based microelectronics devices. The understanding *at the atomic scale* of both the silicon oxidation process and the properties of the Si(100)-SiO_2 interface is of significant importance in state-of-the-art silicon microelectronics manufacturing. These two topics are intimately coupled and are both addressed in this theoretical investigation mainly through first-principles calculations.

We first address the atomic structure at the interface. We construct atomistic models of the Si(100)-SiO_2 interface accounting for the density of coordination defects, the amount and location of partially oxidized Si atoms, and the mass density profile, as measured in electron-spin-resonance, photoemission, and X-ray reflectivity experiments, respectively. A variety of model interfaces are obtained, differing by the degree of complexity in the transition region.

The nature of the transition structure at Si(100)-SiO_2 interface is investigated by addressing the inverse ion-scattering problem. In particular, we refer to a new set of ion-scattering measurements carried out in the channeling geometry to achieve sensitivity to Si displacements at the interface. To interpret these experimental data, we perform ion-scattering simulations on a selected set of model interfaces presenting different atomic-scale features in the transition region at the Si(100)-SiO_2 interface. Silicon displacements larger than 0.09 Å are found to propagate for three layers into the Si substrate. Transition structures consistent with these distortions include Si-Si in-plane dimers, O-protrusion, and/or disordered bond patterns at the Si(100)-SiO_2 interface. A transition structure with regularly ordered O bridges results inconsistent with experiments.

We then address the silicon oxidation process. We first focus on the diffusion limited regime occurring during the growth of thick oxide films. In particular, we provide an atomic-scale description of the long-range oxygen migration through the disordered SiO_2 oxide. The O_2 molecule is firmly identified as the transported oxygen species and is found to percolate through interstices without exchanging oxygen atoms with the network. The associated activation energy is found in agreement with experimental values. Then, we address the O_2 diffusion rate through the thin oxide layer at the Si-SiO_2 interface. In particular, we investigate the combined effect of a percolative diffusion mechanism and of a dense oxide layer located close to the silicon substrate. We find that when a thin densified layer is present at the Si(100)-SiO_2 interface, the O_2 diffusion rate drops below its value for bulk amorphous SiO_2 for oxide thicknesses larger than 2 nm. These results support the *blocking layer* model introduced to explain the failure of the Deal and Grove model in describing the oxidation kinetics of thin oxide films.

Finally, the *atomic scale* mechanisms responsible for oxidation at the Si(100)-SiO_2 interface are addressed. First we focus on the properties of negative oxygen species in amorphous SiO_2. We initially focus on the relative energetics of neutral and negative oxygen species in both the atomic and the molecular state. The energy landscape and the dissociation properties of the O_2^- and O_2^{2-} are also considered. We find that, in amorphous SiO_2, the negative oxygen species incorporate in the oxide network and are accommodated by significant network distortions. The investigation of the dissociation processes of the negatively charged molecular oxygen species in amorphous SiO_2 highlights the dependence of the dissociation energies on the disordered nature of the network and on the charge carried by the oxygen molecule. In a second stage, we address the atomistic processes occurring at the Si(100)-SiO_2 interface. We consider the neutral O_2 molecule and the negatively charged molecular species. In the case of the neutral O_2 molecule, different spin states are investigated. For all these species we study sequentially the network incorporation and the dissociation process. We find that at the Si(100)-SiO_2 interface all these species incorporate in the network either spontaneously or by crossing small energy barriers. In the vicinity of the interface, the neutral O_2 molecule attacks and penetrates into Si-Si bonds. This process is favored by the charge transfer from the Si-Si bonds to the molecular species. The triplet spin state of the O_2 molecule narrows the channels for network incorporation. Indeed, molecules in the triplet spin state preferentially incorporate in the network in correspondence of the upper layer of the Si substrate. Negatively charged species spontaneously incorporate in any Si-Si bond of the oxide, regardless from distance from the interface. Their incorporation is often associated to the formation of network defects, confirming their ability to modify the network. After the incorporation process, the dissociation and hence the oxidation of Si-Si bonds is spontaneous. We find either vanishing or very small dissociation energies. The energy required for crossing the small barriers is provided by the energy gained during the incorporation process. These results are consistent with a variety of experimental observations.

Chapter 1

SiO_2 grown on Si

1.1 Introduction

Silicon dioxide (SiO_2) films thermally grown on crystalline silicon (Si) substrates constitute the main material for gate dielectrics in metal-oxide-semiconductor devices [1]. SiO_2 has a high resistivity, an excellent dielectric strength, a large band gap, and a high melting point. Furthermore, SiO_2 is the native oxide of Si, it efficiently passivates the Si surface states, and forms a Si-SiO_2 interface with a very low concentration of defects. The outstanding properties of both SiO_2 and its interface with Si have allowed the Si-based metal-oxide-semiconductor field-effect transistor (MOSFET) to become the basic element of stable, reliable, large scale integrated circuits. Since the 1960s, with the appearance of the first MOSFET device and the advent of the integrated circuit semiconductor technology, the progressive down scaling of device dimensions have brought about outstanding scientific and technological challenges [1, 2, 3]. Nowadays, basic issues at the very forefront are limiting further evolution of the silicon technology [2]. In particular, MOSFET devices based on SiO_2 are close to fundamental limits. In this regime, an atomic-scale understanding becomes imperative [2, 3, 4].

A schematic cross-sectional view of a MOSFET is shown in Figure 1.1. In this structure, SiO_2 is used for several different purposes. The oxide labeled "gate oxide" is subject to the most stringent quality requirements. Indeed, this dielectric must support the electric field that controls the concentration of majority carriers in the semiconductor region near the Si-SiO_2 interface and thus enables conduction between source and drain (Fig. 1.1). Nowadays, gate dielectrics implemented in very-large scale integration fabrication are between 2 and 9 nm thick [2, 3, 4].

Notwithstanding all the progress made in physical and chemical deposition methods,

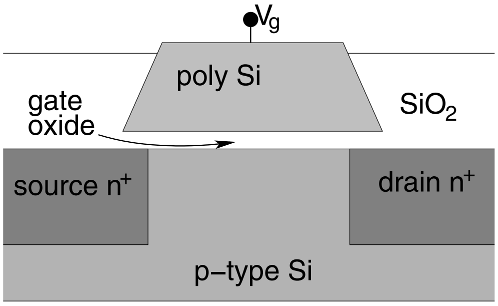

Figure 1.1: Schematic cross-sectional view of a MOSFET. The gate oxide, indicated by the arrow, is located in between the poly-silicon and the semiconductor substrate (p-type Si). V_g controls the conductivity of the p-type Si region near the Si-SiO_2 interface. Flow of current occurs between the source and drain regions.

as well as in physically and chemically stimulated thermal oxide growth, gate dielectrics continue to be based on thermally grown SiO_2 on crystalline Si substrates [5]. The reason is that, no matter how thin gate dielectrics become, the atomic processes during thermal growth lead to the formation of an oxide layer with a nearly perfect interface with the Si substrate. This leads to a density of interface electronic states sufficiently low to fulfill the very strict requirements of stability, reliability and lifetime presently put for MOSFETs [4]. Modern processing routes for the formation of thin gate dielectric layers require not only a very precise knowledge of the growth kinetics but also an atomic-scale understanding of the microscopic processes leading to the formation of the Si-SiO_2 interface. The study of these microscopic processes is the subject of the present theoretical investigation.

1.2 Thermal oxidation of silicon

A single Si crystal exposed to a gas of either O_2 (dry oxidation) or H_2O (wet oxidation) molecules at a certain pressure and temperature forms on its surface a layer of oxide. How does the oxide thickness grows with time? Which are the properties of both the oxide and the Si-SiO_2 interface? Which are the basic mechanisms leading to oxidation? To all these fundamental questions the scientific community has tried to respond since the advent of the silicon-device technology [6, 7, 8, 9, 10, 11, 12, 5, 13, 14]. During the last decades, both theoretical and experimental investigations have allowed us to achieve high level of understanding of the silicon oxidation process [6, 7, 8, 9, 10, 11, 12, 5, 13, 14]. However, many basic issues still remain open or require a thorough analysis.

The kinetics of silicon oxidation is usually presented adopting the phenomenological picture introduced by Deal and Grove about four decades ago [6]. This simple model has proved to be successful in describing silicon oxidation over a wide range of temperature and pressure conditions [6]. Although the Deal and Grove picture presents some limitations, it represents the appropriate framework for either introducing or addressing basic issues related to the silicon oxidation process [9, 10, 11, 12, 5, 13, 14].

1.2.1 The Deal and Grove model

According to the model introduced by Deal and Grove in the 1965 [6], the formation of a thermal oxide film on silicon is supposed to proceed through three sequential steps: (i) the insertion of an oxygen species from the vacuum into a preexisting oxide layer; (ii) the oxidant diffusion through the disordered oxide network toward the Si-SiO$_2$ interface, and finally (iii) the reaction of the oxidizing species near the Si substrate where, upon incorporation in the network, new oxide layers are formed [6] (see Fig. 1.2). Assuming a steady-state condition, the fluxes of entering (J_e), diffusing (J_d), and reacting (J_r) oxidizing species can be expressed in the following form:

$$J_e = h(C - C_0) \qquad J_d = D(C - C_s) \qquad J_r = kC_s \tag{1.1}$$

where h and k are the reaction rate constants of the oxidizing species at the vacuum-oxide and oxide-substrate interfaces, respectively; D is the diffusion coefficient of the oxidizing species in the oxide, while C_0, C and C_s are the oxidant concentration at the vacuum-oxide interface, in equilibrium in the oxide, and at the Si-SiO$_2$ interface, respectively [6].

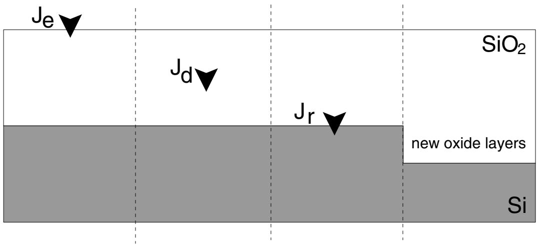

Figure 1.2: Schematic representation of the Deal and Grove model for the Si oxidation kinetics [6]. With J_e, J_d and J_r, we indicate the fluxes of oxidizing species entering the oxide, diffusing through it, and reacting at the Si-SiO$_2$ interface, respectively.

In the steady-state regime, the fluxes of particles J_e, J_d and J_r are supposed to be in equilibrium. This condition leads to a description of the oxidation kinetics in terms of the Deal and Grove equation:

$$X^2 + AX = Bt + X_i^2 + AX_i, \tag{1.2}$$

with

$$A = 2D(\frac{k+h}{hk}) \tag{1.3}$$

and

$$B = 2DC\Omega. \tag{1.4}$$

In Eq. (1.2), X is the oxide thickness, t the time, Ω the oxide volume per oxidizing species, while X_i is the thickness of an oxide film that can be considered either as already present on silicon before beginning thermal oxidation at $t = 0$ or, more properly, the thickness beyond which the assumptions of the Deal and Grove picture become valid [6].

The Deal and Grove model allows us to characterize the oxidation kinetics in terms of two limiting regimes [6]. At relatively large times and for thick oxide films, Eq. (1.2) reduces asymptotically to a parabolic law:

$$X^2 \cong Bt, \tag{1.5}$$

where B is referred to as the *parabolic rate constant* and depends only on the diffusivity and concentration of the oxidizing species in the oxide. In this *thick oxide regime* the oxide growth kinetics is controlled by the oxidant diffusion process through the oxide film. At the other extreme, for relatively small times and thin oxide films, the regime is denominated *thin oxide regime* and the oxidation kinetics follows a linear law:

$$X \cong \frac{B}{A}t, \tag{1.6}$$

where the ratio B/A is referred to as the *linear rate constant* and is equal to:

$$\frac{B}{A} = \frac{kh}{k+h}C\Omega. \tag{1.7}$$

In this regime, the oxidation kinetics is limited by reactions at the interfaces and therefore follows a linear dependence with time. The gas-phase transport coefficient h is usually orders of magnitude larger than k [6]. Hence, the oxidation kinetics in the thin oxide regime is almost entirely governed by the oxidant reaction rate at the Si-SiO_2 interface [6].

The Deal and Grove model has proved to be extremely successful in reproducing a variety of experimental data describing the silicon oxidation kinetics [6, 15, 16, 17]. In particular, the model predictions result of great accuracy for very thick oxide films and at sufficiently high temperatures [6]. Under these conditions, where the agreement stems clearly from the reliability of the Deal and Grove assumptions, important microscopic hints on the mechanisms governing the silicon oxidation process could be extracted by studying the dependence of the oxidation rate constants B/A and B on ambient conditions. In particular, according to Eqs. (1.3) and (1.4), the coefficient A appears to be almost independent of pressure, while B, which depends on pressure through C, increases linearly with the gas pressure [6]. By Henry's law, this latter result suggests that the dissolved oxidizing species in the oxide is in the same form as in the outer gas, namely O_2 and H_2O for dry and wet oxidation, respectively. Consistent results are also obtained by studying the temperature dependence of the parabolic rate constant B through the oxidant diffusivity in the oxide D (Eq. (1.4)). Indeed, B increases exponentially with temperature, with an activation energy of about 1.2 eV and 0.7 eV for dry and wet oxidation, respectively. These values are nearly identical to the measured activation energy for O_2 and H_2O diffusion in bulk amorphous SiO_2 [18, 19]. Similarly, estimates for the equilibrium concentration of oxidizing species in the oxide C agree well with independent measurements of the O_2 and H_2O solubility in SiO_2 [18, 19]. The overall consistency favors the picture in which molecular O_2 and H_2O are the oxidizing species during dry and wet oxidation, respectively.

Although the Deal and Grove model well describes the high temperature (> 1000 °C) growth kinetics of thick oxide films, it presents some limitations [15, 16, 17]. Indeed, the range of validity of the Deal and Grove assumptions is determined by the initial oxide thickness X_i at $t = 0$ in Eq. 1.2, which can be extracted by comparison with experimental data [6]. Whereas for wet oxidation X_i results to be identical to zero, in the case of dry oxidation it takes a value of about 200 Å [6]. These results suggest that, while for wet oxidation the Deal and Grove model applies in both the thin and thick oxide regime, different oxidation mechanisms from those accounted for in the Deal and Grove picture might prevail in the regime of dry oxidation and oxide thickness below $X_i \sim 200$ Å.

During wet oxidation, H_2O reacts with the SiO_2 network forming Si-OH groups, leading to an oxide of degraded electrical performance [5]. Hence, though wet oxidation is faster, the silicon oxidation for the manufacturing of Si-based devices is usually carried out in dry O_2 ambient. For this reason, in the following, wet oxidation will not be considered any longer. From now on, silicon oxidation will implicitly refer to thermal silicon oxidation in O_2 ambient.

1.2.2 The anomalous initial oxidation rate

After the seminal work of Deal and Grove [6], several accurate experimental investigations focused on the Si oxidation process providing a wide range of data for the oxidation kinetics [16, 20, 17]. All studies confirmed that for thick oxide films the Deal and Grove model appropriately describes the growth kinetics. However, for thin oxide films ($<$ 200 Å), an anomalous high oxidation rate was observed when compared with the prediction of the Deal and Grove model [16, 20, 17]. To facilitate the comparison between the prediction of the Deal and Grove model and the experimental oxidation data, it is convenient to consider the inverse of the oxidation rate. From Eq. (1.2) we have:

$$\frac{dt}{dX} = \frac{A}{B} + \frac{2X}{B}. \tag{1.8}$$

A schematic view of the comparison between experiment and Deal-Grove theory (Eq. (1.8)) is given in Fig. 1.3.

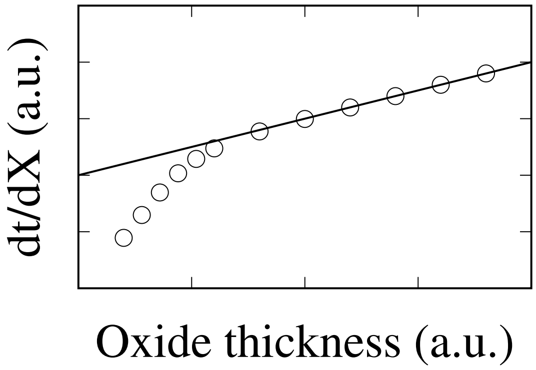

Figure 1.3: Schematic view of the inverse oxidation rate as a function of oxide thickness. The straight line reproduces the Deal and Grove predictions, as in Eq. (1.8). Circles represent the typical experimental behavior for the oxide growth kinetics in dry conditions. Arbitrary units are used for both the thickness and the inverse oxidation rate [16].

The anomalous initial growth regime (Fig. 1.3) was first attributed either to space charge effects [6, 21] or, erroneously, to microchannels in the vicinity of the Si-SiO_2 interface along which diffusion of the oxidizing species was favored [22]. However, preserving the basic assumptions of the Deal and Grove model, the anomalous initial oxidation regime can be more simply accounted for by supposing variable oxidation rate constants (Eqs. (1.3) and (1.4)) [9]. In fact, agreement between the Deal and Grove model and experiment can be recovered assuming a variable interfacial reaction rate constant, initially very high and gradually decreasing toward a constant value for thicker oxides. Alternatively, according to the *blocking layer* model, one might assume a variable B in Eq. (1.8), being smaller for thin oxide films. This hypothesis has been justified assuming the existence of an oxide layer close to the Si-SiO_2 interface where the diffusivity of the oxidizing species is smaller than in the remaining part of the film [9]. The presence of this blocking layer has been related to the compressive stress applied during growth to the oxide near the Si substrate, where the volume per Si atom has to approximately double going from crystalline Si to SiO_2 [23, 24, 25, 9, 20]. It is worth noting that, under these assumptions, the linear regime could be entirely eliminated ($k = \infty$), and the oxidation process could only consist of a diffusion-limited regime with a variable parabolic rate constant [9].

The analysis of the growth kinetics alone does not allow one to distinguish between the hypotheses proposed to explain the anomalous initial oxidation regime, nor between all the associated kinetic models introduced so far [26, 27, 20, 17, 28, 29, 30, 31, 32].

1.3 Transport phenomena during Si oxidation

While kinetics data only indirectly give access to the mechanisms governing silicon oxidation [6], ^{18}O tracer experiments provide direct information on the transport phenomena occurring during this process [33, 34, 35, 36, 37, 38, 39, 40]. In this type of experiments, a SiO_2 layer is first grown up to a thickness X_0 in O_2 ambient of natural isotopic composition (^{16}O). Next, the oxide undergoes further growth to a thickness of $X_0 + \Delta X$ in highly ^{18}O-enriched oxygen. Hence, the analysis of the ^{18}O depth location provides useful indication about the transport phenomena that occurred during the oxidation sequence. Using a variety of techniques for isotope depth location, ^{18}O tracer experiments have been carried out to study the growth of both thick and thin oxide films [33, 34, 35, 36, 37, 38, 39, 40]

After an oxidation sequence of ^{16}O followed by ^{18}O, almost all the heavy isotope is found close to the Si-SiO_2 interface, when the initial $Si^{16}O_2$ layer is sufficiently thick [33, 34, 37]. No exchange between the oxidant and the oxide network is observed. After the second oxidation, a few percent of all the ^{18}O is found near the external oxide surface. These pieces of evidence clearly suggest that the $^{18}O_2$ molecules diffuse interstitially through the oxide toward the Si-SiO_2 interface, in accord with the Deal and Grove assumptions. Moreover, the fact that no detectable interaction between the migrating molecule and the oxide is observed emphasizes the peculiar behavior of the external oxide surface at which ^{18}O can replace ^{16}O by exchange processes. Indeed, an ^{16}O regrowth after an ^{16}O/^{18}O oxidation sequence diminishes the amount of ^{18}O fixed near the external oxide surface [33, 34].

Very thin dielectric films (∼40 Å) grown by a ^{16}O/^{18}O oxidation sequence show overlapping isotope depth profiles across the oxide [33, 34, 37, 38]. This observation contrast with the Deal and Grove mechanism. Accordingly, numerous propositions have been advanced to explain this deviation [33, 34, 37, 38, 8]. In particular, transport through the thin oxide film has been assigned to network oxygen defects [9]. Oxygen vacancies (≡Si-Si≡ or E′ centers), peroxyl linkages (≡Si-O-O-Si≡) [36], valence alternation pairs (O_3^+ and O_1^-, where the subscripts identify the coordination number with neighboring Si atoms) [34] and charged oxygen species (O_2^-, O_2^{2-}) have been proposed as oxidizing species during oxidation of thin oxide films [9]. Moreover, in the context of the *reactive layer* model [8], also Si atoms were proposed as migrating species. In particular, the concept of *reactive layer* was introduced to account for both the oxygen isotopic distributions observed after sequential $^{16}O/^{18}O$ oxidation of thin films and the evidence of a thin transition region of non-stoichiometric oxide near the Si(100)-SiO_2 interface [8]. In this model, an intermediate thin layer (~10-20 Å) of a distinct 'reactive' oxide is supposed to be located in between the silicon substrate and the amorphous SiO_2. This layer was proposed to contain an excess of Si atoms, reacting readily with incoming O_2 molecules at the boundary with amorphous silica, and allowing oxide growth for out-diffusion of Si atoms from the substrate [8]. However, very recently, high-resolution Si-isotopic substitution experiments give direct evidence for Si immobility during silicon oxidation [41].

In spite of the numerous experimental investigations, there are no direct observations favoring a particular oxidizing species in the thin oxide regime. Basic questions remain on the microscopic mechanisms determining the growth of the thin oxide films on silicon.

1.4 The Si-SiO_2 interface

Because of the strict requirements of reliability and performance of MOS devices dictated by the semiconductor industry [2, 3, 4], the properties of both the SiO_2 film grown on Si by thermal oxidation and the Si-SiO_2 interfacial region constitute topics of considerable importance and interest [1]. Moreover, the structure of the Si-SiO_2 interface is intimately related to the oxidation mechanisms leading to its formation [42, 43]. Hence, both theory and experiments in this research area are particularly active [1, 44].

A general consensus exists on the nature of the oxide grown on Si. Sufficiently far from the Si-SiO_2 interface, the oxide acquires the same properties as those of silica [45]. The oxide is amorphous, namely without any long range order. However, as in the crystalline forms of SiO_2, the tetrahedral structure is preserved at short distances. In particular, the tetrahedral SiO_4 unit, a Si atom surrounded by four O atoms, constitutes the building block of amorphous SiO_2. Indeed, its structure is commonly assumed to be a continuous random arrangement of SiO_4 units (continuous random-network model) [46]. The situation and the degree of understanding of the interfacial region is quite different. At the Si-SiO_2 interface, the conversion of Si in stoichiometric SiO_2 requires a 120% increase in molar volume. It is therefore intuitive to assume that such a transition is attained through an interfacial oxide layer with properties different from those of an oxide distant from the Si-SiO_2 interface. Experiments support these considerations. Indeed, Si $2p$ core-level photoemission spectra of the Si-SiO_2 interface show, in addition to the lines corresponding to Si and SiO_2, the occurrence of three intermediate peaks. The total and relative intensities of these peaks contain information which is specific of the interfacial region. In fact, these peaks, approximately 1 eV apart, are associated to intermediate oxidation states of Si, denominated Si^{+1}, Si^{+2}, and Si^{+3} [47, 48, 49, 50]. According to a simple charge transfer picture, these intermediate states of oxidation correspond to Si atoms coordinated with 1, 2 and 3 oxygen atoms, respectively [47, 48, 51, 52]. Core-level photoemission measurements give about 1.8 monolayers for the total amount of these chemical moieties, distributed within a few Si-O bond lengths from the Si substrate [49, 50]. In addition, very recent X-ray reflectivity measurements suggest that, within a few percent, the oxide layer in proximity of the Si substrate is denser than regular amorphous SiO_2 [53, 54]. A mass density between 2.3 and 2.4 g/cm^3 has been estimated [53, 54].

On the theoretical side, despite more than two decades of modeling efforts [55, 56, 42, 57, 58, 59, 44], the atomic scale structure of the interface between crystalline Si and its amorphous oxide has remained elusive. Most of the proposed model structures fail to reproduce the full set of atomic-scale properties derived from experiment [44].

1.5 Outline and organization

The kinetics of the silicon oxidation process, the oxygen transport phenomena through the oxide during oxidation of thick and thin dielectric films, as well as the structural properties of the Si-SiO_2 interface, are all topics treated in this theoretical investigation. In Chapter 2, we generate model structures for the Si(100)-SiO_2 interface consistent with a large set of experimental data. Then, in Chapter 3, we present an investigation resulting from a close collaboration with an experimental group. The nature of the transition structure at the interface is elucidated by addressing the inverse ion-scattering problem. In Chapter 4, the oxygen transport phenomena in bulk amorphous SiO_2 are investigated and characterized. We provide insight into the O diffusion properties during Si oxidation in the thick oxide regime. Moreover, we highlight the importance of the SiO_2 network properties in determining the diffusion rate. We then address the *blocking layer* model to explain the kinetics in the initial stages of oxidation. Finally, in Chapter 5, we focus on atomic-scale transport and reaction phenomena occurring during the initial stages of Si oxidation.

Our investigation is carried out using a variety of theoretical methods. First-principles calculations based on density-functional theory as well as classical interatomic potential are used to describe energetic aspects. Furthermore, both molecular dynamics and Monte-Carlo techniques are employed for exploring the phase space associated to our systems. All these methods and approaches are described by many excellent reviews [60]. Across this presentation, we will mostly focus on the results obtained with these tools. Details of our technical implementation will only be provided when these are necessary for clarity.

Chapter 2

The Si(100)-SiO_2 interface

2.1 Introduction

The gate oxide in Si-based electronic devices has been designed to be thinner with each new generation of the technology [1, 4]. In the present generation, this oxide film has a thickness below 2 nm [61]. In this regime, the transition layer at the Si-SiO_2 interface constitutes a significant fraction of the total thickness and its detailed physical properties affect device performance [2]. The understanding of the Si-SiO_2 interface *at the atomic scale* has proved to be very challenging and to be intimately coupled to understanding the mechanism of SiO_2 film growth.

Several experimental techniques [62] have so far provided well defined atomic-scale information on the bonding pattern at the Si(100)-SiO_2 interface [44]. The amorphous nature of the oxide is confirmed by both transmission electron microscopy and X-ray scattering [62]. The density of the oxide near to the substrate is higher than that of vitreous silica by at most 10% [53, 54]. Electrical [63] and electron-spin-resonance [64] measurements give extremely low densities of interface defects consistent with an almost perfect bonding network across the interface. The interface region is further characterized by photoemission spectroscopy which reveals the occurrence of three intermediate oxidation states of Si [48, 65, 49, 50], corresponding to Si atoms with different O coordinations [51, 52].

A large variety of atomistic model structures of the Si(100)-SiO_2 interface have recently appeared in the literature [44, 51, 52, 42, 66, 59, 67, 68, 58, 69, 57]. However, none of these models matches the full list of atomic-scale properties mentioned above. The practical realization of such a model structure is nevertheless of prime importance. First, this would demonstrate the occurrence of atomic structures in which the information resulting from various experimental probes is consistently assembled. Second, this realization would define the present status of our experimental knowledge concerning the bonding pattern at this interface and provide a basis for future investigations.

In this chapter, we construct atomistic model interfaces of the Si(100)-SiO$_2$ interface with the intent of incorporating the available atomic-scale experimental data. To generate model structures, we use in sequence classical molecular dynamics simulations and first-principles relaxation methods. Our study reveals that the available experimental data are compatible with various structural models which significantly differ in the interfacial bonding patterns.

2.2 Atomic-scale information from experiments

Our target consists in generating model interfaces with the following atomic-scale properties derived from experiment. First, our model structure should reproduce the disordered nature of the oxide [62]. Second, our model structure should be consistent with the extremely low density of coordination defects (one defect out of 300 Si interface atoms) [63, 64]. Third, the mass density profile in our model structure should agree with X-ray reflectivity measurements, which estimate that the mass density of the oxide layer in proximity of the Si substrate ranges between 2.3 and 2.4 g/cm^3 [53, 54], slightly denser than vitreous SiO$_2$ obtained from the melt (2.2 g/cm^3). Fourth, the transition region in our model structure should contain Si atoms in intermediate oxidation states in accord with Si $2p$ core-level photoemission experiments [49, 50]. Following the conventional interpretation scheme [48, 65, 51, 52], recent photoemission experiments yield 1.8 monolayers (1 ML $= 6.5 \cdot 10^{14}$ atoms/cm^2) of partially oxidized Si atoms, distributed between Si^{+1}, Si^{+2}, and Si^{+3} moieties according to the ratio of 1:2:3 [49, 50]. From recent angle-resolved spectra obtained with synchrotron radiation [49, 50], one deduces in addition that the Si^{+1} and Si^{+2} moieties are located right at the interface, while the Si^{+3} ones are distributed within a few Si-O bond lengths from the interface.

2.3 Generation scheme for model interfaces

To generate model structures of the Si(100)-SiO$_2$ interface, we use a two-step procedure. In the first step, we construct a suitable topological connection between substrate and oxide. For this purpose, we use classical molecular dynamics [70] at relatively high temperatures ($\sim$3500 K) to evolve Si and O atoms in the presence of a template of fixed Si atoms representing the substrate. A slow quench (10 K/ps) to low temperatures provides us with oxides attached to the template without any coordination defect. By

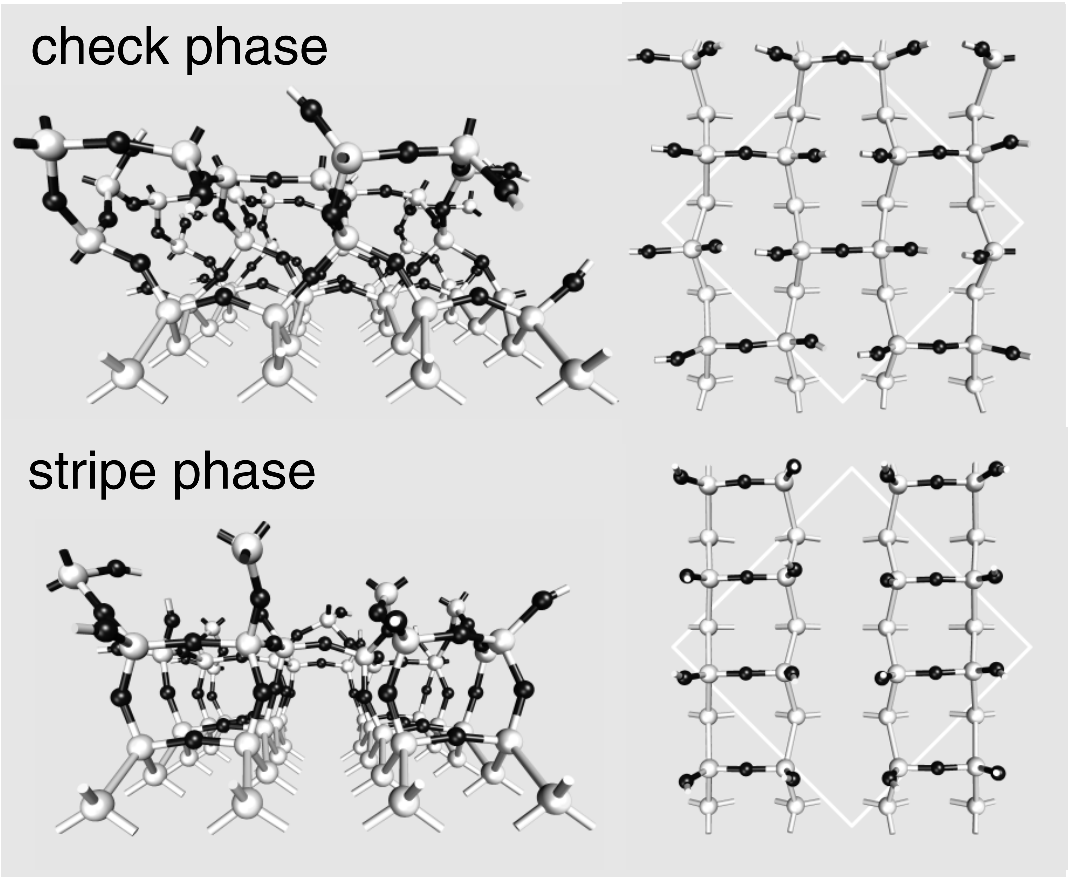

Figure 2.1: Side (right panel) and top (left panel) views of abrupt model structures with a regular pattern of O bridges at the Si(100)-SiO_2 interface in the check (top) and stripe (bottom) phase, respectively. Si and O atoms are indicated by light and dark spheres, respectively. The repeat unit containing $\sqrt{8} \times \sqrt{8}$ Si interface atoms is highlighted in the top views.

varying the positions of the Si atoms in the template, we obtain model structures showing different bonding patterns at the interface.

The template exposes two (100) opposite faces to the oxide within an orthorhombic super-cell. To preserve the directionality of the bonding around the Si atoms of the template, we insert auxiliary O atoms into the Si-Si bonds in the template. For the same purpose, in some cases, we also use an additional decaying three-body O-Si-O interaction [71] for the outer Si atoms of the template. The mass density of the oxide is controlled by setting from the outset the size of the simulation cell. From a single *oxide–template–oxide* superstructure generated using the classical scheme, we construct two model interfaces by 'cutting' the system halfway the template and halfway the oxide.

Then, the template in both models is extended by adding (100) Si monolayers. The final model structures are obtained by terminating the unsaturated bonds at the outer surfaces with H atoms. The final model structures for the Si(100)-SiO$_2$ interface are periodic in directions parallel to the interface with a repeat unit of $\sqrt{8} \times \sqrt{8}$ interface Si atoms. For a repeat unit of this size, the low experimental density of interface defects [64] is best described by a perfect bonding network, as is the case for the present model structures.

In the second step, the model structures are further optimized. First, the targeted distribution of partially oxidized Si atoms is achieved by removing a few O atoms from the oxide. This extends the range of partially oxidized Si atoms into the oxide region. Second, we recover optimal structural parameters performing a complete structural relaxation within a density-functional approach [72, 73, 74]. In our first-principles scheme, the electronic structure is described by using a plane-wave basis set for the valence wave functions and pseudopotentials to account for the core-valence interactions. We use a normconserving pseudopotential for Si (Ref. [75]) and ultrasoft pseudopotentials for O and H [76]. The exchange and correlation energy is accounted for within the Perdew-Wang generalized gradient approximation (GGA) [77]. We carry out structural relaxations adopting a damped molecular-dynamics scheme [72, 73, 78]. Energy cutoffs of 24 Ry and 150 Ry are used for the wave functions and for the augmented electron density, respectively. In our model structures of the Si(100)-SiO$_2$ interface, the substrate is represented by 9 monolayers of Si attached to an oxide of thickness ranging between 9 and 15 Å. The extremities of the slab are saturated by H bonds. The last two Si monolayers of the substrate are kept fixed during relaxation.

2.4 Model structures of the Si(100)-SiO$_2$ interface

2.4.1 Abrupt interfaces

We first consider the case of ideal structures with an *abrupt* interface between oxide and substrate. Despite their incorrect distribution of Si oxidation states, such models have often been addressed in the literature [51, 52, 66, 59, 67]. In particular, we here address only model structures with a regular pattern of O bridges at the Si(100)-SiO$_2$ interface. To this end, we use as templates a stack of 2 to 3 (100) crystalline Si planes. The Si atoms of the (100) planes exposed to the oxide are slightly displaced from crystalline sites along the [110] direction. In this way, we favor the generation of model structures with regular patterns of O bridges at the interface: the *stripe* phase of (2×1) symmetry and the *check* phase of $c(2 \times 2)$ symmetry [66, 59, 67] (Fig. 2.1).

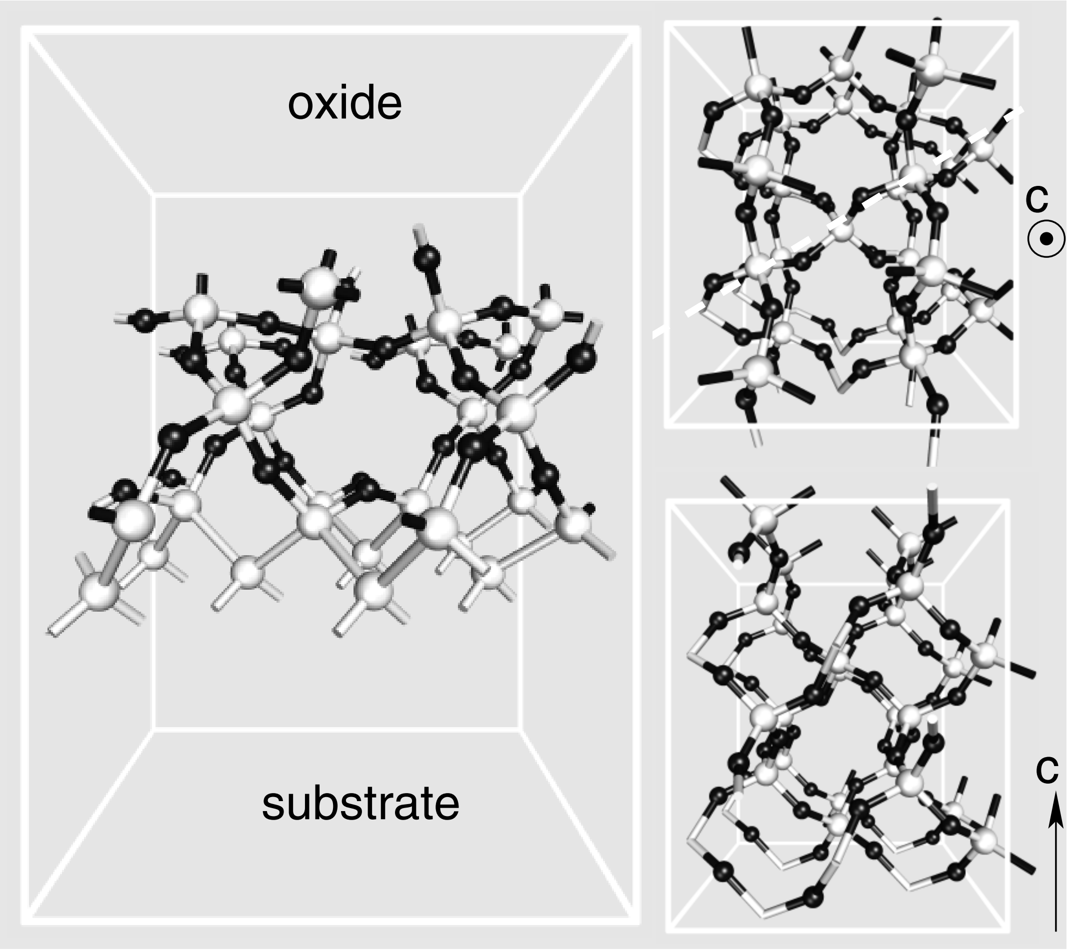

Figure 2.2: Left: side view of the abrupt model structure showing the ideal stripe phase of O bridges at the Si(100)-SiO$_2$ interface. Only a region near the interface is illustrated. Right: views along directions parallel (top) and perpendicular (bottom) to the *c*-axis of the quartz-like oxide. Si and O atoms are indicated by light and dark spheres, respectively.

For these model structures, the oxide in the immediate vicinity of the substrate shows a crystalline bond pattern, corresponding to that of tridymite (Fig. 2.1) and quartz (Fig. 2.2) for the stripe and check phase, respectively. The crystalline order persists for about 3 to 4 Si-O bond lengths into the oxide, before the disorder sets in.

2.4.2 Realistic model interfaces

To generate model structures of the Si(100)-SiO$_2$ interface with a more realistic distribution of partially oxidized Si atoms (Fig. 2.3), we adopt more involved templates.

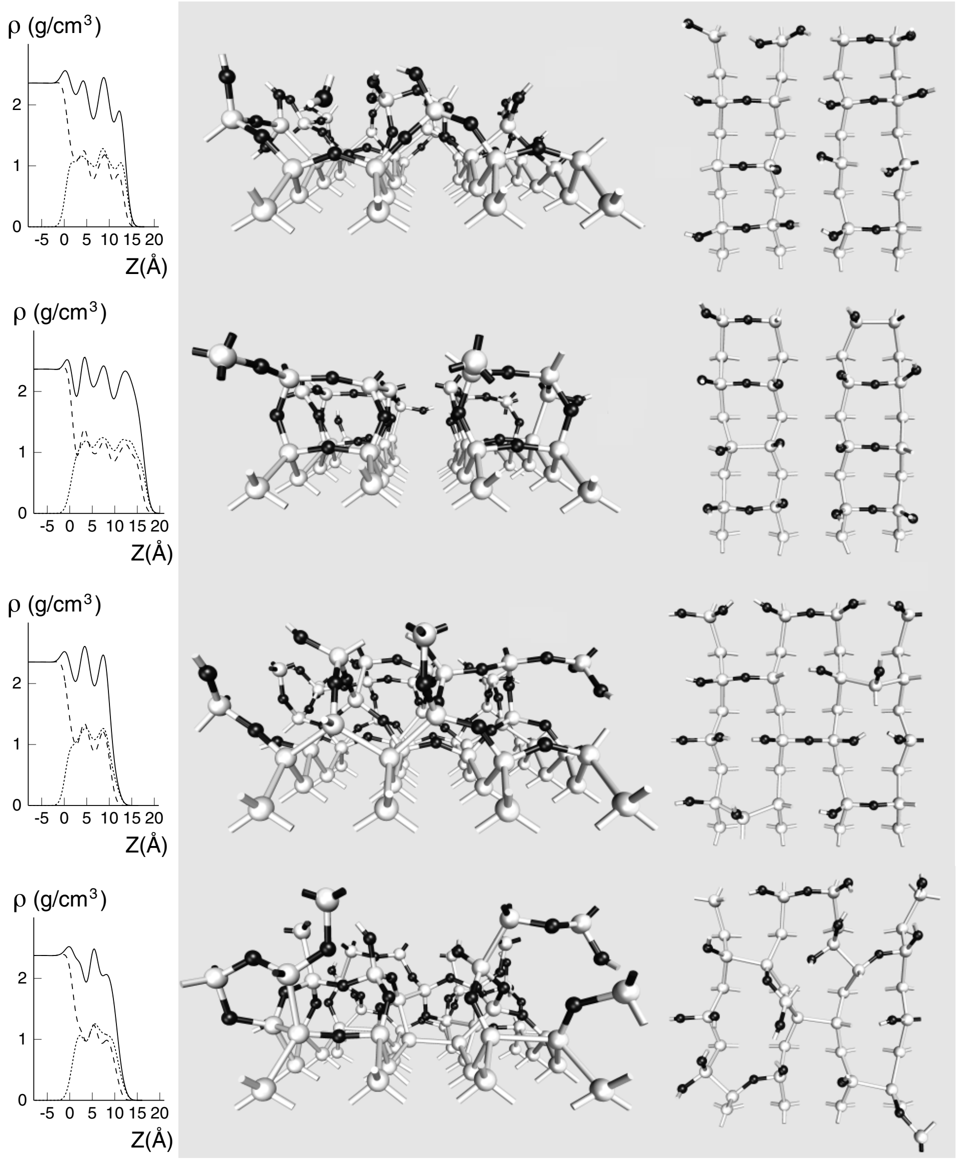

Figure 2.3: Model structures of the Si(100)-SiO$_2$ interface. Left panels: mass density profile across the oxide region for four Si(100)-SiO$_2$ model interfaces generated in this work. The density is averaged in planes parallel to the interface, broadened by a Gaussian with a standard deviation of 1 Å, and plotted along the z coordinate (solid line). Si (dashed) and O (dotted) contributions are shown separately. The origin of the z axis corresponds to the first oxidized Si monolayer. Middle panels report the side views of the transition region at the Si(100)-SiO$_2$ interface. Right panels show top views of the bond pattern near the upper layer of the Si substrate. O (Si) atoms are represented by dark (light) spheres.

	Si^{+1}-O	Si^{+2}-O	Si^{+3}-O	Si^{+4}-O
Si-SiO_2 models	1.68	1.66	1.65	1.63
model clusters	1.67	1.64	1.63	1.62
periodic systems	1.66	1.65	1.63	1.62

Table 2.1: Mean Si^{+n}-O bond lengths, $n = 1 \ldots 4$, as found in the present Si(100)-SiO_2 model interfaces. Corresponding values obtained for molecular clusters [74] and periodic systems [79] are also reported. Lengths are in Å.

	Full		Suboxide	
	μ	σ	μ	σ
Si-O-Si angles	145.4°	13.1°	146.5°	12.7°
Angles on Si	109.4°	4.9°	109.3°	8.8°

Table 2.2: Mean (μ) and standard deviation (σ) of bond-angle distributions for the present Si(100)-SiO_2 model interfaces. Partially oxidized Si atoms are analyzed separately.

To increasing order of complexity, we consider templates containing more sizeable displacements from crystalline positions, Si-Si in-plane dimer bonds, and/or Si-Si bonds protruding into the oxide. We also use a template presenting a disordered Si-Si bonding arrangement, as found with a first-principles molecular dynamics simulation [42]. In this way, we generate several different model structures, four of which are shown in Fig. 2.3. Although the structures of the resulting oxides do not show any crystalline order, the mass density profile across the SiO_2 component shows interesting features (Fig. 2.3). Indeed, for model structures presenting a *nearly* abrupt transition region, the mass density shows regular oscillations in the direction perpendicular to the interface with a period of about 4 Å (first three models in Fig. 2.3). This regularity in the mass density profile across the oxide component is less apparent or completely lacking in model interfaces with a transition region showing structural disorder and extending over more than one monolayer (fourth model in Fig. 2.3).

Average structural parameters for bond lengths and bond angles are given in Table 2.1 and Table 2.2, respectively. Si-O bond lengths associated to partially oxidized Si atoms are generally longer than the mean bond length in SiO_2, and tend to decrease as the Si oxidation state increases (Table 2.1). The same trend has also been observed in model clusters [74] and periodic systems [79]. Bond angle distributions do not show any particular dependence on Si oxidation state or on distance from the interface. The

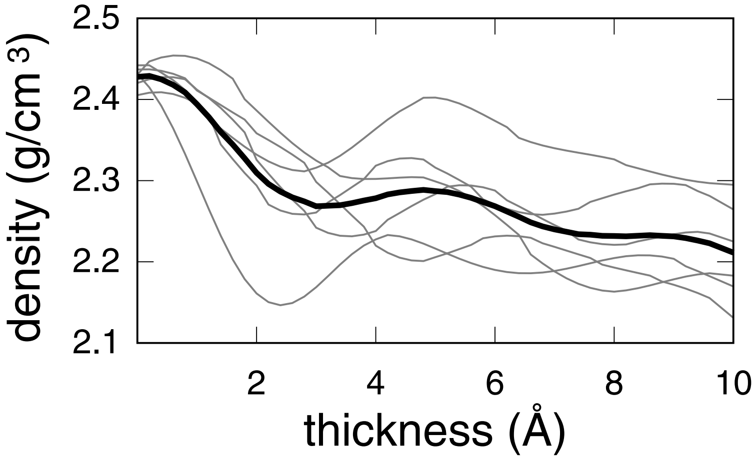

Figure 2.4: Mass density profile (gray) for the interface models generated in this work, together with their average profile (black). The mass density is given for layers of increasing thickness starting at the interface and extending into the oxide.

tetrahedral coordination of the Si atoms is well preserved, both in the oxide and in the suboxide region (Table 2.2). The width of the distribution of bond angles centered on the Si atoms is smaller than in previous models [44], indicating a lower degree of local strain [80, 81]. The mean Si-O-Si bond angle is close to that of vitreous silica [82].

All the model structures contain the *same* distribution of partially oxidized Si atoms, in accord with recent photoemission data [49, 50]. More specifically, our model structures contain 0.3, 0.7, and 0.9 ML of Si^{+1}, Si^{+2}, and Si^{+3} moieties, respectively. The Si^{+1} and Si^{+2} are located right at the interface while the Si^{+3} moieties are distributed in the oxide within a range of 3 to 4 Si-O bond lengths from the interface (Fig. 2.3).

Figure 2.4 shows the mass density profile across the transition region for all our model interfaces. The mass density is evaluated for layers of increasing thickness starting at the interface and extending into the oxide. Individual models show fluctuations of about ± 0.1 g/cm^3 with respect to the mass density profile averaged over our models (Fig. 2.4). The average mass density is found to decay slowly from about 2.4 g/cm^3 in the immediate vicinity of the interface to 2.2 g/cm^3 for an oxide thickness of 10 Å. These results are in agreement with X-ray reflectivity experiments which indicate the occurrence of a thin interfacial oxide layer of mass density ranging between 2.3 and 2.4 g/cm^3 [53, 54].

2.5 Summary

While all our generated models agree with the identified set of experimental data, their degree of structural order in the transition region varies considerably (Fig. 2.3). In particular, in models obtained by introducing minimal modifications to the upper Si layer of the substrate, structural order extends from the upper layers of the substrate to the near-interface oxide region. At variance, models resulting from templates with a disordered pattern of Si-Si bonds and O bridges in the upper Si layer of the substrate present oxides where disorder sets in right at the interface. This variety of model interfaces shows that the degree of order/disorder in the transition region cannot be distinguished by the available experimental data [53, 54, 63, 64, 49, 50]. This ambiguity also reflects our limits in understanding the oxidation mechanisms which lead to the formation of the Si(100)-SiO_2 interface [42, 59].

Chapter 3

Transition structure at the Si(100)-SiO_2 interface from analysis of ion scattering

3.1 Introduction

In the previous chapter, we introduced a two-step procedure based on classical molecular dynamics and a first-principles relaxation scheme for generating realistic model structures of the Si(100)-SiO_2 interface. Hence, accounting for several pieces of atomic-scale information derived from experiments, we were able to construct a variety of models presenting important differences in the bond pattern at the interface. Such differences are manifested by both the degree of structural order in the near-interface oxide and the amount of distortions in the upper layers of the Si substrate. This degree of complexity in the transition region could not be distinguished by the available experimental data [53, 54, 63, 64, 49, 50].

Ion-scattering experiments performed in the channeling geometry are particularly sensitive to the Si side of the Si-SiO_2 interface. From early measurements at a selected ion energy [83, 84], the structure at the interface could be characterized in terms of *excess silicon yield*. This quantity gives an estimate of the number of Si atoms out of register with respect to their ideal lattice positions. Hence, ion-scattering experiments are particularly suitable for measuring the nature of the atomic arrangements at the Si(100)-SiO_2 interface.

In the following, we set out to interpret a new set of ion-scattering data in terms of atomistic models. In particular, we introduce a new scheme to perform ion-scattering

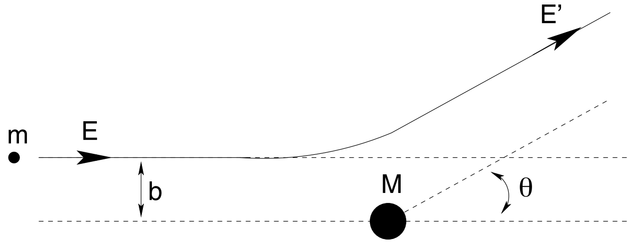

Figure 3.1: Schematic picture of the scattering process between a light energetic ion and a heavy atom. For simplicity, the motion of the heavy atom is not shown.

simulations on atomistic models. Then, we consider several model structures for the Si(100)-SiO$_2$ interface presenting important differences in the bonding pattern at the interface and address the inverse scattering problem by comparing experimental and calculated ion-scattering yields.

3.2 Rutherford ion scattering experiments

3.2.1 Basic principles

Energetic ions (He$^+$ with a kinetic energy of the order of $\sim$ 1 MeV) moving across a solid may have close ($\sim 10^{-4}$ Å) impacts with lattice atoms. These encounter events originate billiard type collisions leading to remarkable deviations of the ion trajectories [85, 86, 87].

An ion of initial energy E, elastically scattered at an angle θ by an atom of the solid, carries after the scattering event an energy E' given by:

$$E' = E\ K_M(\theta) = E\left(\frac{\sqrt{M^2 - m^2\sin^2\theta} + m\cos\theta}{M + m}\right)^2, \tag{3.1}$$

where $K_M(\theta)$ is the kinematic factor, and m and M are the masses of the ion and the atom, respectively (see Fig. 3.1). Thus, the mass of the scattering atom determines the backscattered ion energy E'. In Rutherford ion-scattering experiments, a beam of light energetic ions is focused on a solid and the backscattered ions are detected at a specific angle θ. Through the mass sensitivity of the energy of these backscattered ions (Eq. (3.1)), these experiments can therefore distinguish the occurrence of different elements in the solid. Moreover, since the differential cross-section associated to the scattering process ($d\sigma/d\Omega$, the number of projectiles scattered per unit of area and time within the solid angle between θ and $\theta + d\theta$) is a known function of the ion energy and the scattering angle, ion-scattering experiments allow for quantitative analysis. In particular, the total number of particles of mass M_0 and surface density N_0 (atoms/cm^2) may be extracted

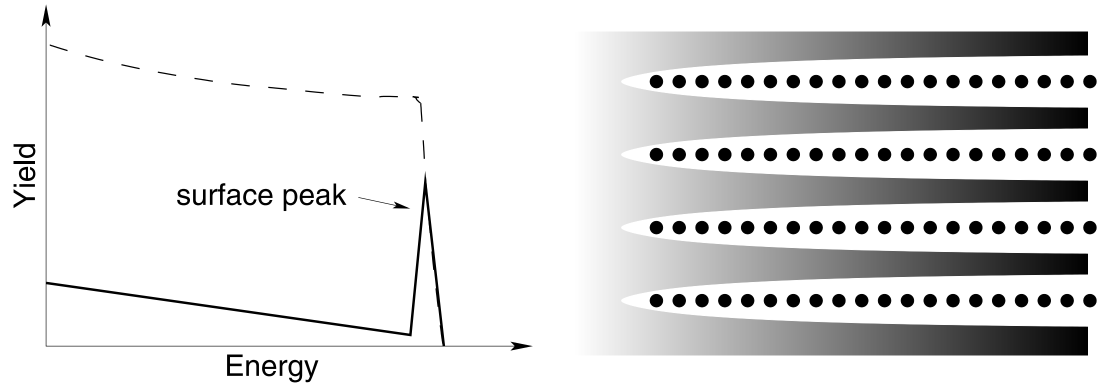

Figure 3.2: Left panel: schematic representation of the energy spectrum obtained from ion-scattering experiments performed on a single crystal in the channeling (solid line) and in the non-channeling (dashed line) geometry. Right panel: schematic representation of the channeling effect. A uniform ion flux invests the crystalline structure from the left. As it penetrates into the crystal, the flux concentrates within the channels (increasing darkness).

from the measured ion scattering yield, Y_0, by:

$$Y_0 = N_0 \, \frac{d\sigma}{d\Omega} \, \Delta\Omega \; Q, \tag{3.2}$$

where Q is the measured flux of incident ions and $\Delta\Omega$ the width of the solid-angle acceptance of the detector.

As the energetic light ions penetrate into the solid, energy is dissipated primarily through inelastic collisions with the electronic cloud. The rate of energy loss, dE/dx, is a function of the incident energy and of the atomic parameters of the projectile and of the host. For He$^+$ projectiles, in the 0.5- to 2.0-MeV energy region, dE/dx is relatively independent of energy and a simple analysis of depth effects is possible. In particular, in the approximation of constant dE/dx, the final energy $E'(x)$ of a particle at normal incidence that backscatters from a depth x is given by:

$$E'(x) = K_M(\theta) \, \left[E - x\frac{dE}{dx} \right] \; - \; \frac{x}{\cos\theta} \, \frac{dE}{dx}. \tag{3.3}$$

Thus, ions backscattered at different depths emerge from the solid (at a given angle θ) with different energies, resulting in a continuous energy spectrum. The depth resolution in ion-scattering experiments is determined by the energy resolution of the detector, the rate of energy loss dE/dx, and the geometry. Typical depth resolutions are of the order of 30-100 Å. The approximate constancy of dE/dx and the fact that $d\sigma/d\Omega$ almost corresponds to that of a pure Rutherford scattering have made the 1.0 MeV energy region the dominant one for materials applications of ion scattering [85, 86, 87, 83, 88, 89, 84, 90, 91, 92, 93, 94, 95, 96, 97, 98].

When ion-scattering experiments are performed on an amorphous target, the ions of the beam undergo multiple small-angle uncorrelated deflections. Hence, each atom of the solid can be assumed to be invested by an uniform flux of ions. Accordingly, the continuous energy spectrum is featureless and is simply determined by the thickness of the probed target (Fig. 3.2) [85, 86]. At variance, when the beam is focused on a single crystal and aligned along a major symmetry axis (*channeling geometry*), the ion-scattering energy spectrum results drastically modified (see Fig. 3.2). In this case, the impact parameter distribution is uniform only for the atoms of the first surface layers. Small angle scattering events determine the impact parameter for the second atom in the column along the crystal symmetry axis. Further correlated scattering events proceed along the column enhancing the non-uniformity of the ion flux with depth [85, 86]. In particular, as ions penetrate into the crystal, the flux distribution focuses within the channels parallel to the crystal symmetry axis (*channeling effect* [99]). The scattering probability therefore rapidly reduces with depth and the energy spectrum mainly consist of a peak, the surface peak, originating from the first monolayers at the surface (Fig. 3.2). Ion-scattering experiments performed in the channeling geometry carry important information on the surface structure (Fig. 3.2) [83, 89, 84, 90, 91, 92].

3.2.2 The excess Si yield at the Si-SiO$_2$ interface

Since energetic ions penetrate for microns into a solid, they can also be used as a probe of the atomic structure at the Si-SiO$_2$ interface [83, 93, 96, 97, 98]. When ion-scattering experiments are performed in the channeling geometry, the detected energy spectrum consists of two peaks, originating from O atoms in the oxide and Si atoms in both the oxide and substrate, respectively (see Fig. 3.3).

The O peak corresponds to the thickness of the oxide. Hence, assuming a perfect stoichiometry, the integrated O yield ($Y_{\rm O}$) corresponds to twice the yield from Si atoms in the oxide. Moreover, the yield associated to an ideally terminated Si crystal ($Y^{\rm ideal}$) can be derived from simulations (see Sec. 3.3.5). Accordingly, from the total integrated Si yield ($Y_{\rm Si}$), it is possible to substract contributions of Si atoms in the oxide and substrate, leaving a quantity associated only to the interfacial Si-SiO$_2$ region. In particular,

$$\Delta Y = Y_{\rm Si} \; - \; Y_{\rm O}/2 \; - \; Y^{\rm ideal} \tag{3.4}$$

is defined as the *excess Si yield* [83, 84], and consists of a genuine interface property associated to both (i) Si atoms in the upper layers of the substrate out of register

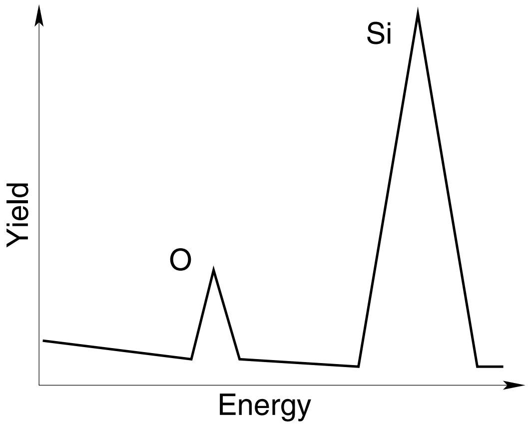

Figure 3.3: Schematic representation of energy spectra obtained from ion-scattering experiments performed on the Si-SiO$_2$ interface. Both peaks can accurately be converted to areal atomic densities.

with respect to their ideal lattice positions, and (ii) Si atoms in the oxide carrying an intermediate oxidation state. The latter contribution stems from the partial cancellation in Eq. (3.4) between the total Si yield Y_{Si} and the term $Y_{\mathrm{O}}/2$ for the suboxide. However, obtaining atomic-scale information from the excess Si yield is not trivial and requires the solution of the inverse scattering problem.

3.2.3 Ion-scattering experiments at Si-SiO$_2$ interface

In the present chapter, we interpret a new set of ion-scattering data in terms of atomistic models. The measurements were taken in the group of L.C. Feldman (Vanderbilt University, Department of Physics and Astronomy, Nashville, Tennessee).

Rutherford ion scattering experiments were carried out at room temperature on oxides grown via a high quality rapid thermal oxidation process, known to produce device quality dielectric layers. The samples were oriented in a two axis goniometer and probed with a He$^+$ beam by incidence along the normal $\langle 100 \rangle$ direction. To enhance surface sensitivity, a grazing exit angle geometry was used with the detector at a scattering angle of approximately 95°. Absolute yields giving the amount of Si and O atoms were obtained with an estimated error of $\pm$ 5%.

In Fig. 3.4, we give measured ΔY for ion energies ranging between 0.4 and 1.0 MeV. In this regime, the measurements are sensitive to Si displacements between 0.09 and 0.14 Å [90, 86].

3.3 Ion-scattering simulations

To interpret the experimental excess Si yields and extract atomic-scale information on the structure of the Si(100)-SiO$_2$ interface, we need a simulation scheme able to

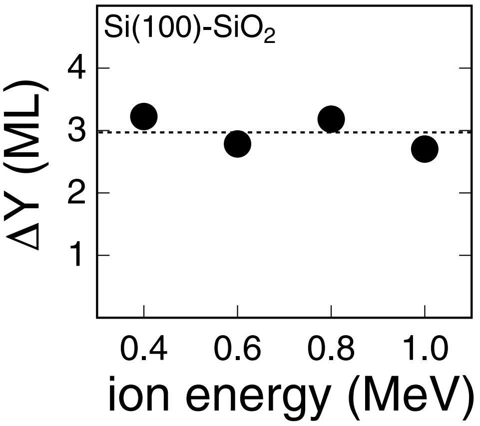

Figure 3.4: Measured excess Si yields vs ion energy for the Si(100)-SiO$_2$ interface. Excess Si yields are expressed in [100] monolayers (1 ML = $6.8 \cdot 10^{14}$ atoms/cm^2). Excess Si yields fluctuate around 3 ML with a standard deviation of 0.3 ML.

compute ΔY from atomistic models. We use a classical scheme based on the theoretical framework presented by Barrett [100].

3.3.1 The simulation scheme: Basic approximations

Our scheme is designed to model ion-scattering experiments carried out in the channeling geometry. Hence, ions impinge on the model system parallelly to a crystal symmetry axis. Ion trajectories are reconstructed adopting the binary collision approximation [101]. Accordingly, trajectories consists of connected straight-lines segments, representing the sequence of asymptotes arising from the cascade of binary collisions. The ions are followed during the penetration along the crystalline columns. Intra-column scattering events have a small cross section and are therefore not accounted for during the simulations [90]. Backscattered ions are detected at $\theta = 180°$ within a solid angle of width $\Delta\theta$.

The motion of the ions is treated classically. This approximation is valid for He$^+$ ions with kinetic energies in the range considered in the present study [100, 99]. The interaction between He$^+$ and the atoms of the atomistic models is described by a screened Coulomb potential:

$$V(r) = \frac{zZ}{r}\phi(r/a) \tag{3.5}$$

where $\phi(r/a)$ is the Thomas-Fermi screening function, a the screening length, z and Z the nuclear charges of the ion and the scattering atom, respectively. For $\phi(r/a)$, we use the approximate form proposed by Molière [100, 99]:

$$\phi(r/a) = \sum_{i=1}^{3} \alpha_i \exp(\beta_i r/a) \tag{3.6}$$

where $\{\alpha_i\} = \{0.1, 0.55, 0.35\}$ and $\{\beta_i\} = \{6.0, 1.2, 0.3\}$. The value for a used for fully ionized ions coincides with the Thomas-Fermi screening length (a=0.8853 a_0 $Z^{-1/3}$), while for partially ionized ions, such as He$^+$, we adopt the value derived by Firsov (a=0.8853 a_0 $(z^{1/2} + Z^{1/2})^{-2/3}$, a_0 is the Bohr radius) [102].

Ions impinging parallelly to a crystal symmetry direction undergo small-angle collisions along the crystalline columns. Apart from the collision event which eventually determines the backscattering, forward scattering events along the colums are associated with relatively large impact parameters and with small kinematic energy transfers upon impact with the heavier scattering atom. Therefore, it is a good approximation to assume that the scattering atoms are immobile. Under this assumption, in a binary collision, the ion trajectory is deflected in the plane containing both the ion and the scattering atom by:

$$\theta = \pi - 2\int_{R_{\min}}^{\infty} \frac{b\,dr}{r\,g(r)} \qquad \text{where} \qquad g(r) = \sqrt{r^2 - \frac{r^2 V(r)}{E_0} - b^2}, \tag{3.7}$$

E_0 is the ion energy, b the impact parameter, $R_{\min}$ the apex of the trajectory defined by $g(r) = 0$, and $V(r)$ the potential in Eq. (3.5). We also neglect the energy loss of the ions due to inelastic scattering with valence ($\sim$ 10 eV) or core ($\sim$ 100 eV) electrons [101, 85, 86].

For a given atomic configuration of the model system, the ion-scattering yield is obtained in two steps. In the first step, basins for backscattering at 180° are identified by a steepest ascent procedure. We proceed as follows. We consider an ion trajectory which enters the surface at normal incidence from a point $\mathbf{r} \equiv (x, y)$ and "back"scatters at an angle θ. Then, we numerically evaluate the gradient of the function $\theta = \theta(\mathbf{r})$ at $\mathbf{r}$ and move the impinging point $\mathbf{r}$ along the direction of increasing scattering angle θ. The size of the step is chosen at random between zero and a maximal value which depends on the value of the calculated gradient. This maximal value is chosen to correspond to half the displacement required to reach θ=180° under the assumption of linearity. Hence, by iteration, the point $\mathbf{r}$ is constantly driven toward a region where ions backscatter at an angle near to 180°. To identify all the significant basins for backscattering, this procedure is carried out starting from many different initial points.

In the second step, the regions around the identified basins for backscattering are uniformly sampled. In this way, for each atomic configuration of the model system, we calculate the cross section $\Sigma_\pi(\Delta\theta)$ associated to backscattering at 180° within an acceptance angle $\Delta\theta$. To obtain the corresponding ion-scattering yield, we refer Σ_π to the atomic cross section σ_π:

$$Y = \frac{\Sigma_\pi(\Delta\theta)}{\sigma_\pi(\Delta\theta)}. \tag{3.8}$$

In this way, a direct comparison with experimental data can be carried out. We note that the present procedure provides us with a numerically *exact* determination of the ion-scattering yield.

The thermal motion of the investigated atomistic system is modeled by displacing the atoms isotropically, randomly, and independently [90, 86]. Vibrational correlations do not significantly affect the calculated ion-scattering yields [103] and are not included in our the simulations. Displacements are mapped according to a Gaussian distribution with a standard deviation corresponding to the experimental mean square displacement at ambient temperature. The total yield is obtained by an average of instantaneous yields associated to a sequence of different thermal atomic configurations of the model system.

3.3.2 Two atom model

The basic physical aspects of ion scattering can be introduced by considering a beam of parallel ions hitting a system consisting of two atoms: the *two atom model* [85, 86, 104]. The two atoms are held fixed at a distance d and the ion beam is aligned with their conjoining direction (see Fig. 3.5). Ions incident on the top atom with small impact parameters undergo large angle scattering. The rare close encounters of this type contribute to the backscattering yield near 180°. For large impact parameters, the impinging ions undergo small deflections and proceed forward to determine the ion flux distribution for the next atom (Fig. 3.5). In particular, trajectories with an impact

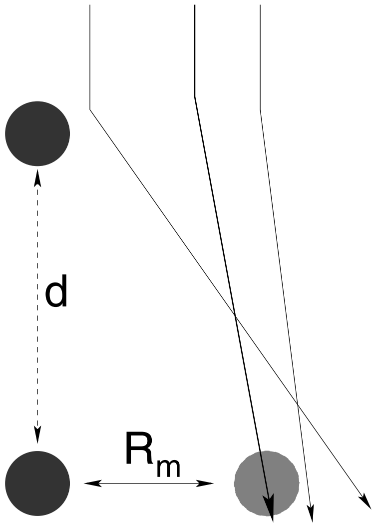

Figure 3.5: Scheme of the two atom model. Atoms are represented by black circles. The ions impinge parallelly to the direction defined by the two atoms. Ion trajectories (straight-lines segments) are deflected by the top atom. When the second atom falls apart from its original position by more than the critical distance R_m (shaded sphere), it starts to being exposed to the deflected ion beam. The ion trajectory which mostly approaches the second atom is thickened.

parameter b with respect to the top atom lie at distances:

$$R(b) = b + d \tan \theta(b) \tag{3.9}$$

in the plane perpendicular to the beam and in correspondence of the second atom. Around a critical impact parameter b_0, $R(b)$ in Eq. (3.9) becomes stationary with respect to b, acquiring its minimum value R_m (the *Molière radius*). R_m corresponds to the radius of the shadow cone cast from the top atom onto the second one. The deflected ion beam invests the second atom only when it falls apart from its original position by more than the Molière radius. Outside the shadow cone cast from the top atom, the ion flux reaching the second atom results enhanced and nonuniform. In particular, close to R_m the flux results particularly peaked.

For an unscreened Coulomb potential, an analytical expression exists for the shadow-cone radius R_c:

$$R_\mathrm{c} = 2\sqrt{\frac{zZd}{E_0}}. \tag{3.10}$$

Near R_c, the ion flux at the level of the second atom diverges as $(r - R_\mathrm{c})^{-1/2}$. For a Molière potential, R_m can be expressed as a function of R_c in a general way [105, 88], or computed numerically. In the case of He^+ ions scattered by Si atoms, R_m assumes the values of 0.1332 Å, 0.1110 Å, 0.0973 Å, and 0.0878 Å, for ion energies of 0.4 MeV, 0.6 MeV, 0.8 MeV and 1.0 MeV, respectively. The experimental mean square displacement for Si at ambient temperature is $\langle u_x^2 \rangle^{1/2} = 0.075$ Å [106]. Therefore, shadowing and flux enhancement effects play an important role in determining the ion-scattering yield.

3.3.3 The anomalous yield enhancement

Ion-scattering experiments report an unusual enhancement of the backscattering yield at 180° when narrow acceptance angles are employed [107]. This anomalous yield enhancement is observed both for amorphous targets and, under channeling conditions, for crystalline materials. The augmented yield originates from backscattering in a region near the surface. Moreover, this effect disappears either for scattering at angle different from 180° or for wide acceptance angles [107]. Several theoretical investigations have addressed this intriguing anomalous effect [108, 109, 110, 111, 104, 112, 113]. To explain the ion-scattering yield enhancement near 180°, concepts as flux peaking [111, 104, 112, 113] and reversibility of ion trajectories have been invoked [108, 109, 110]. These suggestions were corroborated by simulations based on the *stochastic model* for calculating the ion-scattering yield [112, 114]. In these simulations a uniform flux of classical ion trajectories is directed toward a model system and followed during penetration. In this way, the ion flux distribution is constructed at any depth. Hence, the ion-scattering yield is extracted assuming the reversibility of ion trajectories and the statistical equilibrium for the distribution of the ion flux within the solid [112]. In particular, equal probabilities are assigned to the process of ions incident on a solid reaching a particular atomic site and to that of ions starting from a particular atomic site and emerging from the solid back along the incident direction [112]. However, in a recent experimental investigation, the *stochastic model* has been severely criticized [114]. In particular, it has been pointed out that, although this model provides results consistent with experimental measurements, the approximations introduced by the *stochastic model* may neglect other contributions to the yield enhancement near 180°. In fact, while the *stochastic model* properly accounts for both the flux peaking effect and the reversibility of inward and outward trajectories, it completely neglects beam focusing effects [114]. This last phenomenon is expected to contribute significantly to the anomalous yield enhancement [114].

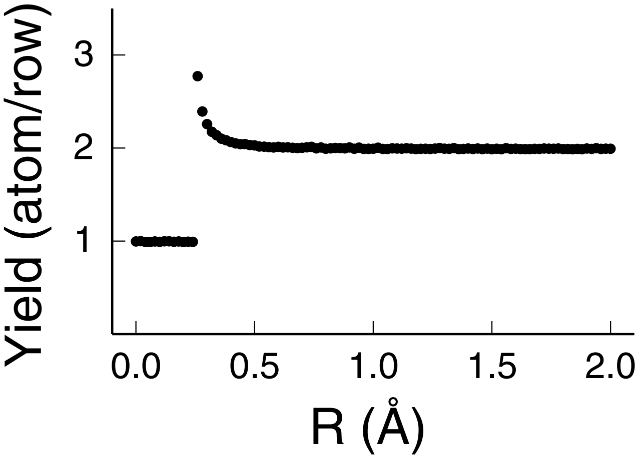

Figure 3.6: Ion-scattering yield for a two-atom model vs. distance between the projections of the two atoms in a plane perpendicular to the ion beam. The yield is expressed in atoms per row. The simulated angular aperture of the detector is of 20°.

In this section, we use our simulation scheme to address the issue of yield enhancement near 180°. Our scheme allows for accurate calculations of ion-scattering yields without introducing assumptions on the ion flux distribution as in the *stochastic model*. We consider the *two atom model* invested by He$^+$ ions with an energy of 0.1 MeV. We consider two Si atoms separated by a distance equal to the crystal lattice parameter. The two atoms are initially aligned with the ion beam. The Molière radius is R_m=0.24086 Å. In the following, we consider configurations in which the bottom atom is displaced from its original position in the plane perpendicular to the ion beam. This distance is indicated by R.

In Fig. 3.6, we report the ion-scattering yield with respect to the distance R. For distances R smaller that the Molière radius, the yield corresponds to that of a single isolated atom, whereas, for separations greater than about twice R_m it correctly doubles.

For R slightly greater than R_m, the yield appears strongly enhanced. The enhancement is limited to a narrow region near R_m. As reported in previous theoretical investigations [108, 109, 110, 111, 104, 112, 113], this enhancement is related to the peaking of the ion beam [112, 113] in correspondence of R_m and is favored by the reversibility of the ion trajectory backscattered at 180° [108, 109, 110, 111]. However, this enhancement effect is intrinsic to the multiple scattering process and does not appear related to the angular aperture of the detector. Indeed, the yields reported in Fig. 3.6 have been obtained using an acceptance angle as wide as 20°. Hence, these calculations are consistent with the ion-scattering simulations based on the *stochastic model* which account for the backscattered ion flux, regardless of the width of the solid-angle acceptance around 180°.

We now address the role played by the angular aperture of the detector in enhancing the ion scattering yield. To this end, it is useful to analyze the nature of the ion trajectories backscattered at 180° for the *two atom model.* Hence, we locate the bottom atom at various in-plane distances R. For each configuration of the two atoms, we determine the scattering angle for varying impact parameters along the direction defined by the two atoms (see Fig. 3.7).

When the bottom atom lies within the shadow cone, trajectories at 180° arise only from scattering with the top atom. For distances well above R_m, namely well outside the shadow cone cast by the top atom, two classes of backscattering trajectories at 180° originate from the bottom atom. The first class comprises those hitting the bottom atom with a impact parameter equal to zero. In this case, the ingoing and outgoing part of the trajectory are superimposed. At variance, the second class of trajectories originates from a billiard type collision involving both atoms. These trajectories are almost atop of one atom and scatter backward from near to the other one. When the separation between the atoms increases, the cross section associated to this second type of trajectories decays rapidly.

When the bottom atom is located exactly at a distance of R_m in the plane perpendicular to the direction of the impinging ions, the different classes of backscattering trajectories associated to the bottom atom merge together. The interval of impact parameters for backscattering events at angles close to 180° broadens. Moreover, at b for for which Eq. (3.9) corresponds to R_m, the derivative of the scattering angle with respect to the impact parameter vanishes. This behavior has deep consequences on the ion scattering yield for varying acceptance angles $\Delta\theta$ around 180°. In fact, for $\Delta\theta$ approaching zero the atomic cross section σ_π relative to the top atom goes as $\sim \Delta\theta^2$, whereas that associated to the bottom atom vanishes as $\sim \Delta\theta^{3/2}$. Accordingly, as $\Delta\theta$ reduces to zero, the ion-scattering yield Y defined by Eq. (3.8) diverges to infinity as $\Delta\theta^{-1/2}$ (Fig. 3.8). This behavior is confirmed by numerical analysis of the Ys at small

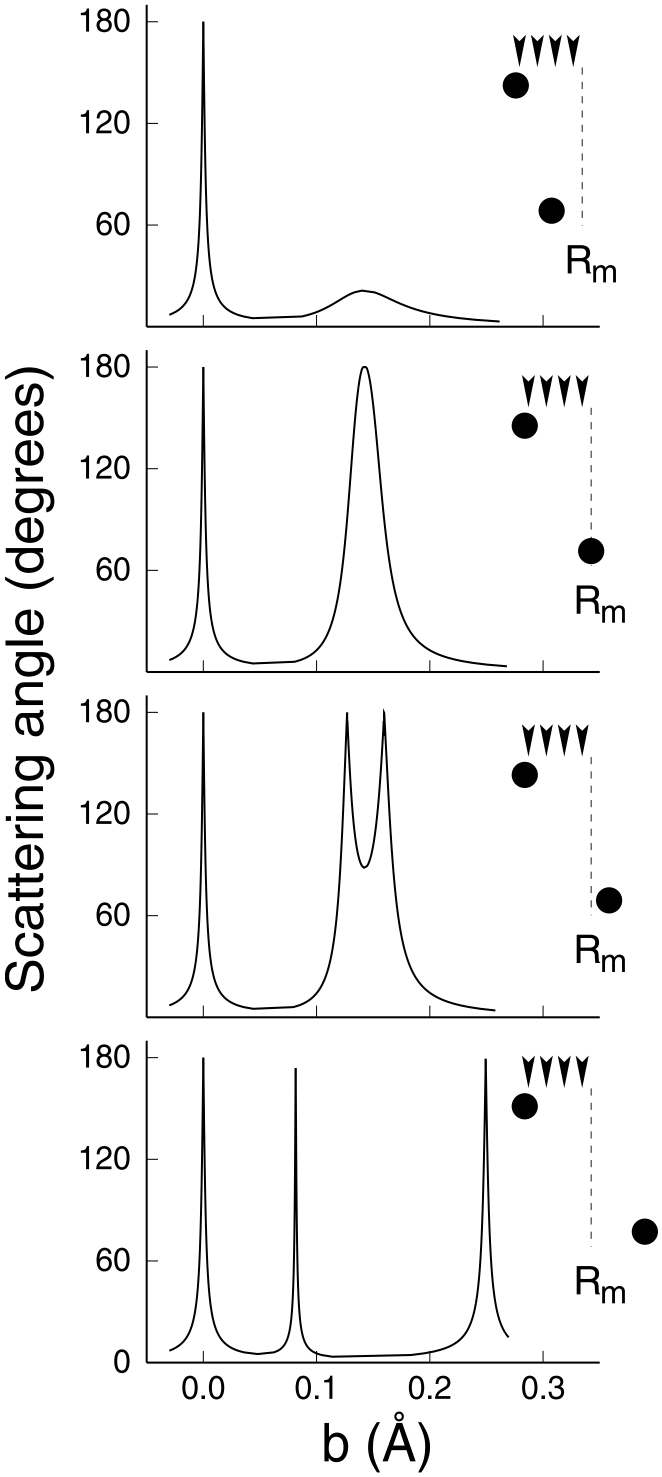

Figure 3.7: Scattering angle vs. impact parameter for a system of two atoms. The top atom is located at the origin. The bottom atom is initially located at a distance corresponding to the Si lattice parameter along the direction of the ion beam. We consider four different displacements of the bottom atom in the plane perpendicular to the direction of the beam: 0.23 Å (top panel), 0.24086 Å (second panel), 0.24286 Å (third panel), and 0.29 Å (bottom panel). The impact parameter is varied along the direction defined by the two atoms, perpendicularly to the ion beam. The energy of the ions is 0.1 MeV and the corresponding Molière radius is 0.24086 Å. At the right top corner of each figure, the two atom configuration is sketched.

$\Delta\theta$. This effect appears particularly pronounced when the bottom atom is at R_m. For increasing R, the yield rapidly decreases (see Fig. 3.8, left panel).

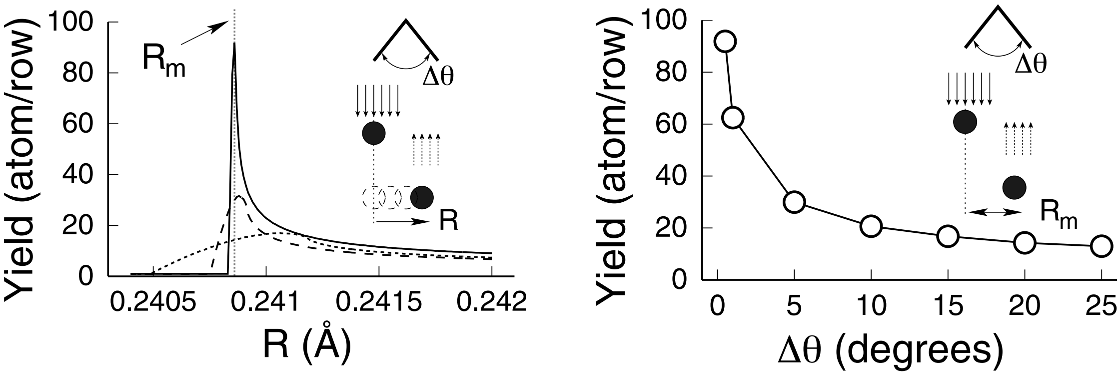

Figure 3.8: Left panel: yield vs. distances near R_m. Curves shown refer to results obtained using acceptance angles of 0.5° (solid), 5° (dashed), and 20° (dotted). The location of R_m is also indicated by a dotted vertical line. Yields are in atoms per row. Right panel: yield vs. acceptance angle of the detector. The relative distance in the plane perpendicular to the ion beam between the two atoms coincides with R_m.

The present analysis of the *two atom model* gives deep insight in the yield enhancement effect. In particular, yield enhancement arises when atoms are located at or near to the region where the ion beam is focused by previous ion encounters. In the case of the *two atom model*, this occurs when the bottom atom is located at a distance of R_m in the plane perpendicular the ion beam. For this atomic configuration, the ion beam is focused onto the bottom atom by the small-angle collisions with the top one. Accordingly, the cross section associated to backscattering at 180° relative to the bottom atom shows a strong enhancement for R=R_m. In particular, as a function of the acceptance aperture $\Delta\theta$, it vanishes more slowly than the atomic cross section. This effect leads to the increase of the total ion-scattering yield at small acceptance apertures $\Delta\theta$.

When atoms move at finite temperature, atomic configurations corresponding to large yield enhancements occur rarely and the total yield is mostly determined by shadowing effects. Nevertheless, for very small acceptance angles, these rare events can raise significantly the average yield. To corroborate these statements, we report the results of ion-scattering simulations for a system consisting of a row of three Si atoms, separated by the crystal lattice parameter. Ions impinge along the row direction with an energy of 0.1 MeV. To favor the occurrence of atomic configurations leading to yield enhancements, we arbitrarily set the mean square displacement equal to R_m. As shown in Fig.

3.9 (left panel), yields associated to individual thermal configurations are concentrated at low values, between one (only the top atom being exposed to the beam, the remaining atoms falling within its shadow cone) and three (the atoms being well separated and are uniformly invested by the beam). However, configurations giving highly enhanced yields clearly occur. The narrower the acceptance aperture of the detector, the larger the weight associated to these rare events (Fig. 3.9, left panel). Accordingly, the average yield associated to this model system raises from about 2.7 atom/row up to 3.5 atom/row, when the acceptance angle is reduced from 20° to 0.1° (Fig. 3.9, right panel). We note due to the large weight associated to rare events, the average yield in Fig. 3.9 (right panel) converges more slowly for smaller acceptance apertures.

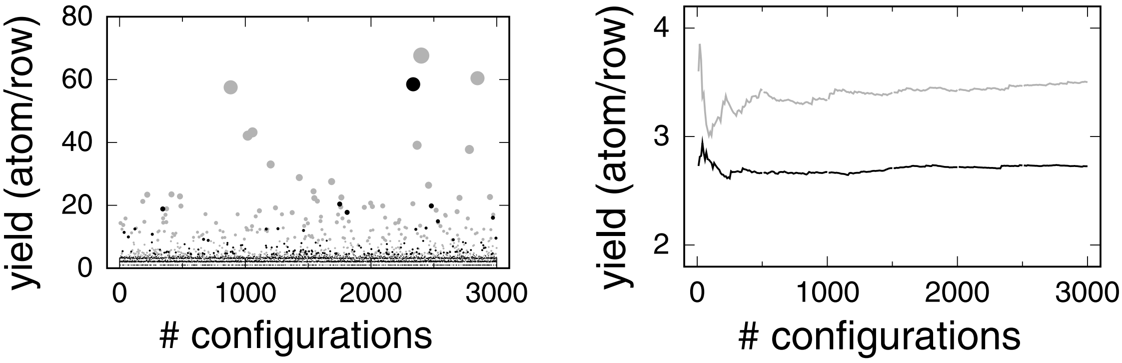

Figure 3.9: Instantaneous (left panel) and average (right panel) yield for a row of three Si atoms, vibrating randomly and independently with a mean-square displacement of 0.24086 Å. Ions of 0.1 MeV impinge along the direction of the row. Black (gray) symbols refer to calculations carried out using an acceptance aperture of 20° (0.1°). To emphasize the yield enhancements, the radii of the discs are taken proportional to the corresponding values of the yield.

3.3.4 Yield from an ideally terminated Si(100) crystal

We here apply our simulation scheme to calculate ion-scattering yields from an ideally terminated Si(100) crystal (Y^{ideal} in Eq. (3.4)). These quantities are fundamental to extract excess Si yields (ΔYs) for the Si(100)-SiO$_2$ interface.

The calculated yields are shown in Fig. 3.10. These values have been obtained using an acceptance aperture of 20°, sufficiently large to neglect enhancements effects occurring close to the exit angle of 180° [107]. To generate thermal configurations, we adopt the experimental mean square displacement for Si at ambient temperature

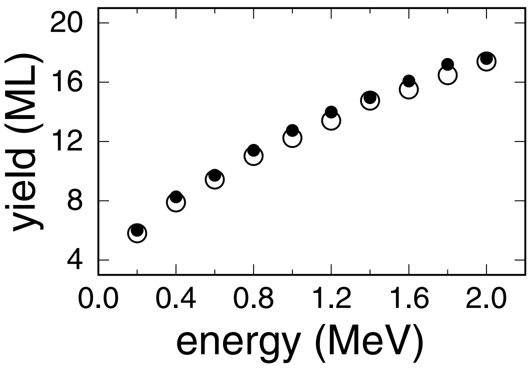

Figure 3.10: Ion-scattering yields vs. ion energy from an ideally terminated Si crystal. Si yields are expressed in [100] monolayers (1 ML = $6.8 \cdot 10^{14}$ atoms/cm^2). Open symbols refer to present calculations while full dots to values obtained with the *stochastic model* [86].

($\langle u_x^2 \rangle^{1/2} = 0.075$ Å) [106]. This procedure well reproduces documented results obtained using the *stochastic model* [90, 86] (Fig. 3.10).

3.3.5 Ion-scattering simulations on reference systems

To assess the accuracy of the ion-scattering simulation approach, we here address Si(100) systems of known structure. For the clean Si(100)-2×1 surface, a recent measurement with ion energies of 0.8 MeV found a Si yield of 13.4 ML [96], in agreement with our calculated yield of 13.1 ML. For the Si(100)-1×1:H surface [115], theory and experiment [90, 86] agree closely over the range of ion energies extending between 0.4 MeV and 1.0 MeV (see Fig. 3.11). We find a maximal error of 0.5 ML. For the Si(111)-1×1:H surface, this simulation method reproduces the experimental yields with a similar degree of accuracy [116]. Hence, differences between experiment and simulation are not meaningful when smaller than ∼0.5 ML.

3.4 Ion-scattering simulation at the Si(100)-SiO$_2$ interface

To address the inverse scattering problem, we here select several atomistic model structures of the Si(100)-SiO$_2$ interface, generated according to the procedure described in Sec. 2.3. These models show atomic-scale features consistent with various experimental probes [53, 54, 63, 64, 49, 50]. However, they present very different bond patterns at the Si(100)-SiO$_2$ interface. The bonding arrangements in the interfacial region affect the distortions propagating into the upper layers of the substrate. These distortions are directly linked to the excess Si yields measured by ion-scattering experiments. The comparison between calculated and measured yields provides insight into the structural

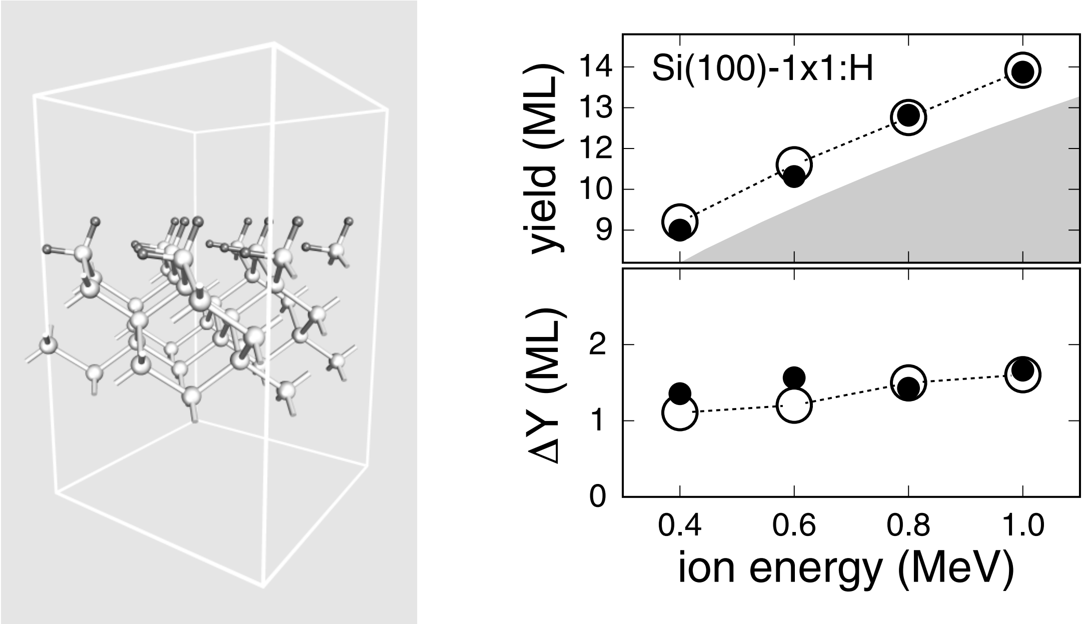

Figure 3.11: Left: canted-row structure for the Si(100)-1×1 dihydride. Only the upper [100] layers near the surface are shown. Si (H) atoms are represented by light (dark) spheres. The atomistic structure has been relaxed using the first-principles scheme described in Sec. 2.3. Right: comparison between experimental (full symbols) and calculated (open symbols) ion-scattering yields for the Si(100)-1×1:H surface. In the upper panel, the contribution corresponding to the unperturbed Si substrate is shaded. In the bottom panel, only the excess Si yields are reported.

properties of the Si(100)-SiO$_2$ interface and into the amount of distortions on the Si substrate side of the interface.

3.4.1 Model interfaces under investigation

We consider interface models periodic in the plane of the interface, with a $\sqrt{8} \times \sqrt{8}$ Si repeat unit. They consist of ~12 Å of oxide at a density of 2.3 to 2.4 g/cm^3, in agreement with X-ray reflectivity measurements [53, 54]. We use 17 Si monolayers (MLs) for the substrate to achieve fully converged results in the ion-scattering simulations. In the relaxation process, the bottom termination of the substrate is selfconsistently coupled to a Keating model [117].

To match recent photoemission data [49, 50], we consider three model interfaces all containing about 1.9 ML of Si atoms in intermediate oxidation states, distributed between Si^{+1}, Si^{+2}, and Si^{+3} as 1 : 1.7 : 2.3. The Si^{+1} and Si^{+2} lie at the interface, while the Si^{+3} are located in the oxide within a few bond lengths. However, the model interfaces differ considerably in their interfacial bonding at the Si termination (Fig. 3.12). In model A, the termination is nearly abrupt and closely corresponds to that of an ideal Si lattice. The bond density mismatch at the interface is accommodated by O bridges. The structure shows a slight departure from the ordered *stripe* phase [59] to accommodate the intermediate oxidation states [49, 50]. The terminating Si layer contains 3 Si^{+1} and 5 Si^{+2} moieties per unit cell. The 7 Si^{+3} moieties are either directly attached to the Si^{+1} moieties or located higher in the oxide. In model B, the terminating Si layer shows a high density of *in-plane* Si-Si dimers. To match the experimental suboxide distribution [49, 50], we introduced O atoms in four of the backbonds of these dimers. The Si^{+1} and Si^{+2} moieties are distributed in the upper two layers of the substrate, while the Si^{+3} are partially in the terminating Si layer and partially higher in the oxide. In model C, the structure of the terminating Si layer is inspired by a model generated previously by first-principles molecular dynamics [42]. The occurrence of several in-plane Si-Si dimers and their disordered arrangement give rise to a transition region of two monolayers which contains most of the partially oxidized Si atoms (Fig. 3.12). Additional Si^{+3} moieties are found higher in the oxide. Model C also contains an extra Si atom with respect to a crystalline monolayer. This atom is in a Si^0 state and falls in the middle of the transition region (Fig. 3.12) [42]. The degree of complexity in the bonding arrangements at the Si(100)-SiO_2 interface reflects on the distortions of the upper layers of the Si substrate. Indeed, in model A, the nearly regular bond pattern at the interface induces gentle distortions which are almost entirely absorbed by the upper Si monolayer of the substrate (Fig. 3.12). At variance, in model C, the disordered pattern at the Si(100)-SiO_2 interface leads to displacements which persist down to the fourth Si monolayer below the interface. The amount of Si monolayers displaced with respect to the lattice positions clearly affect the excess Si yield determined by ion scattering. Therefore, the comparison between calculated and experimental ΔYs provides outstanding information on the distortions in the Si substrate, and indirectly on the degree of complexity of the bond pattern at the Si(100)-SiO_2 interface.

3.4.2 Comparison between experiments and simulations

Ion-scattering yields are calculated for the selected atomistic model structures of the Si(100)-SiO_2 interface. As mean square displacement for Si at ambient temperature, we adopt the experimental value of $\langle u_x^2 \rangle^{1/2} = 0.075$ Å [106]. Since this value lies close to the theoretical estimate of 0.081 Å for Si atoms in amorphous SiO_2 [118], it is also expected to properly describe the partially oxidized Si atoms. The ion-scattering simulations are

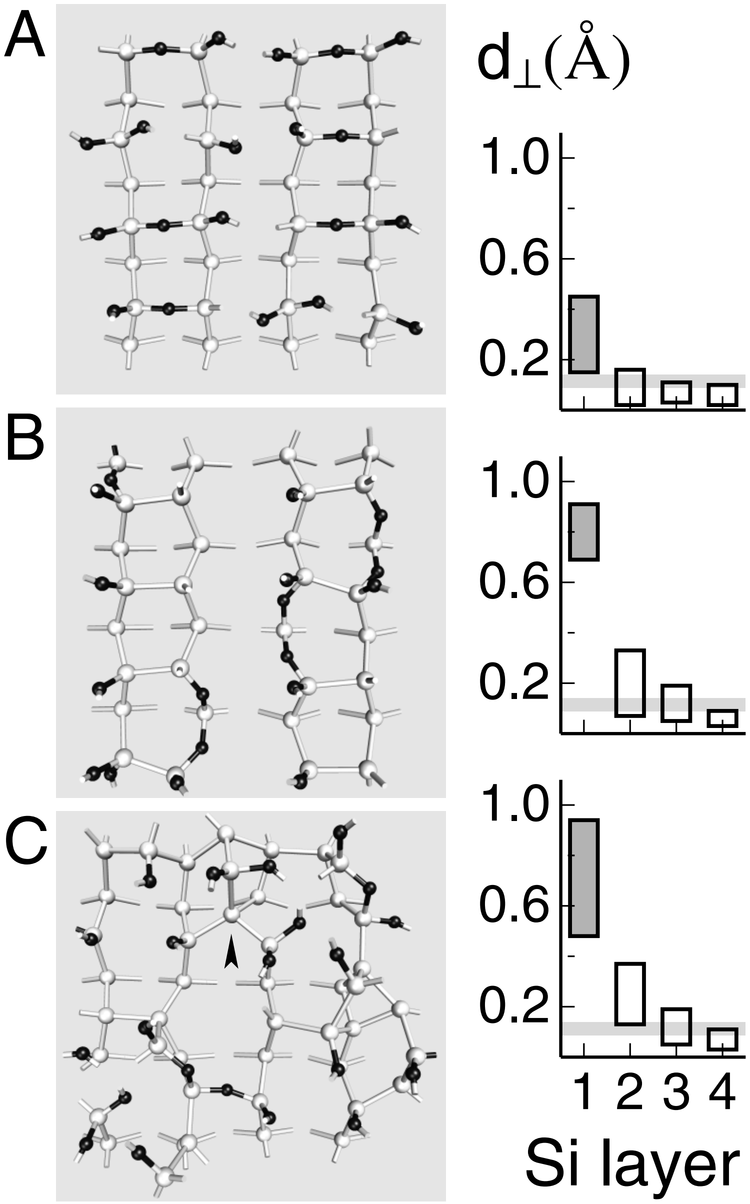

Figure 3.12: Top views of transition structures in models A, B, and C. Light (dark) spheres indicate Si (O) atoms. Respective in-plane displacements for the upper 4 Si layers are given on the right. For each layer, a box is centered on the mean displacement with a vertical height giving the rms deviation. The first layer (dark box) contains partially oxidized Si atoms. The extra atom in model C, indicated by an arrow, was not considered as part of the substrate. The horizontal band indicates the sensitivity of ion-scattering measurements to atomic displacements.

designed to directly provide values for ΔY, as derived in experiments (see Sec. 3.2.2). In particular, oxygen atoms and fully oxidized Si atoms are omitted from the outset in our simulations, to account for their statistically uniform distribution. Partially oxidized Si atoms, Si^{+x} with $x = 1, 2, 3$, are treated in the same way as non-oxidized Si atoms. To every Si^{+x}, we associate a number of O atoms equal to $x/2$, which is then accounted for in the calculation of ΔY, following the experimental definition of ΔY (Eq. (3.4)). More specifically, the simulated excess Si yield $\Delta Y_{\rm sim}$ is extracted as follows:

$$\Delta Y_{\rm sim} = Y_{\rm Si} \; - \; Y^{\rm ideal} \; - \; \sum_{x=1}^{3} N_x \, \frac{x}{4}, \tag{3.11}$$

where N_x is the number of Si atoms in the oxidation state x.

Excess Si yields are obtained by simulation for varying ion energies and are compared to measured values in Fig. 3.13. The calculated excess Si yields do not vary significantly with ion energy. We therefore averaged ΔY over ion energy, and obtained 3.0±0.3 ML from our experimental data. This value should be compared with corresponding values of 1.4±0.1, 2.7±0.1, and 3.6±0.2 ML obtained by simulation for models A, B, and C, respectively. This comparison indicates that the average yield for model A severely underestimates the experimental value, effectively ruling out model A as an acceptable structure for the Si(100)-SiO$_2$ interface. The yields for models B and C are both consistent with the experimental yields. Our results suggest that the bonding pattern at the Si(100)-SiO$_2$ interface is intermediate between those of models B and C.

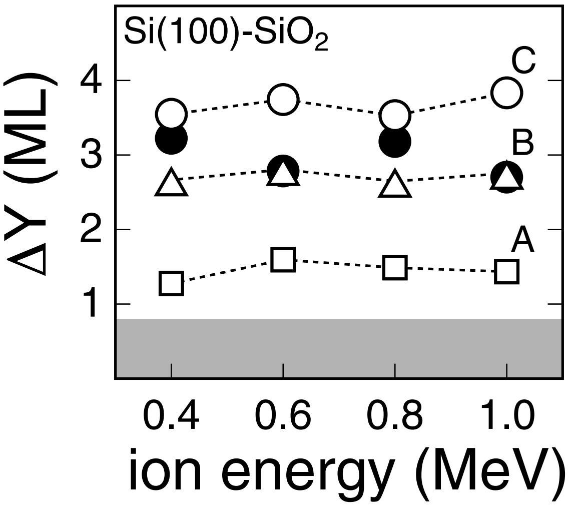

Figure 3.13: Measured (full circles) and calculated excess Si yields vs ion energy for the Si(100)-SiO$_2$ interface. The calculated values are obtained for models A (squares), B (triangles) and C (circles), the contribution from partially oxidized Si atoms is shown by a shaded band.

The contribution to the excess Si yield from partially oxidized Si atoms, $\Delta Y^{\rm subox}$, is obtained under the well-justified assumption that these Si atoms do not interfere with

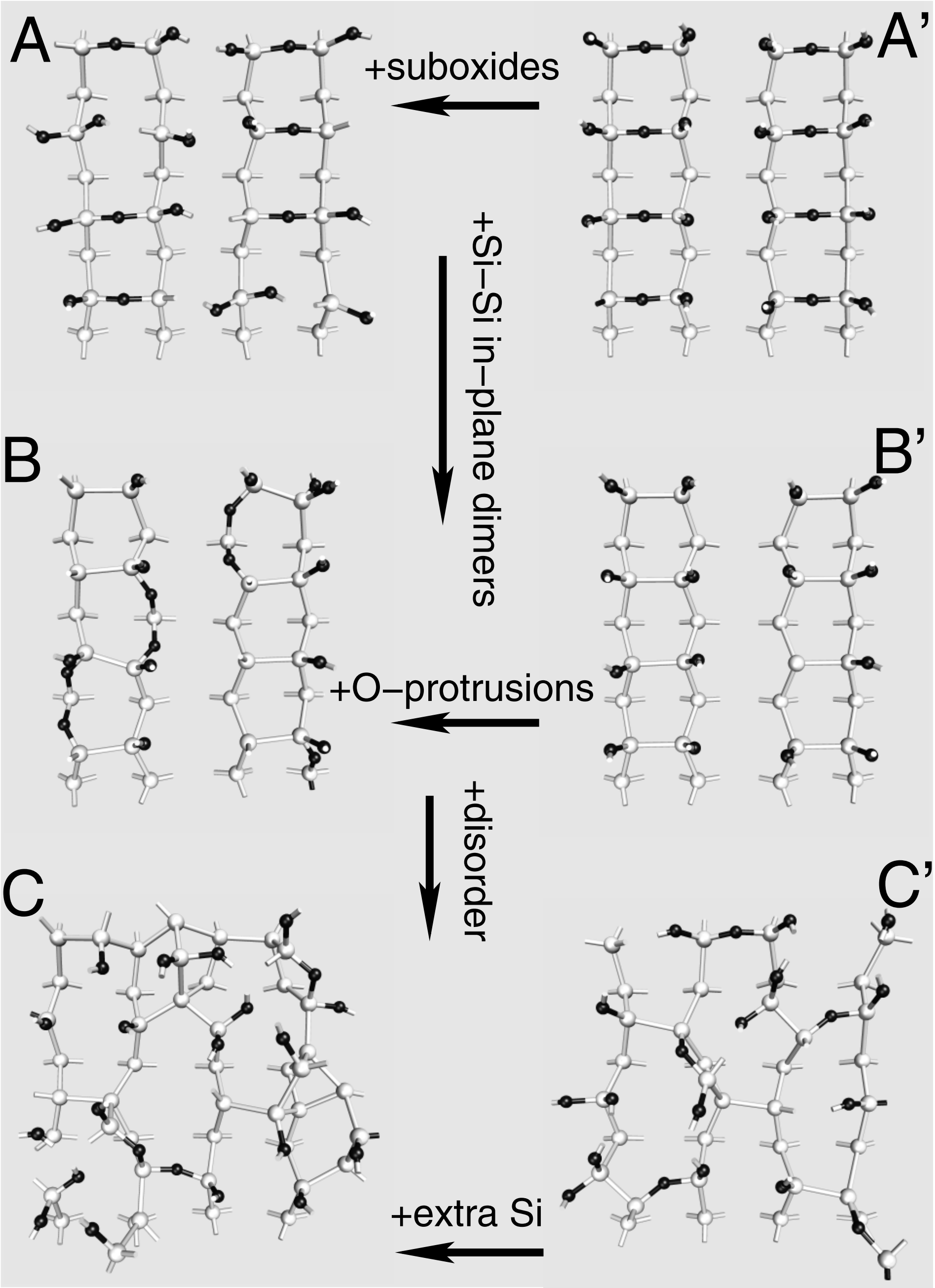

Figure 3.14: Top views of transition structures in models A, B, C and those obtained introducing minor variations, A′, B′, and C′, respectively. Light (dark) spheres indicate Si (O) atoms. Arrows and relative comments indicate the basic differences between the bond patterns.

the scattering at substrate columns. This is satisfied in our models since the in-plane displacements of partially oxidized Si atoms are generally much larger than the Molière radii considered here (Fig. 3.12). Applying the counting rule given above to isolated Si atoms in intermediate oxidation states, we find

$$\Delta Y^{\mathrm{subox}} = 0.75\, N^{+1} + 0.5\, N^{+2} + 0.25\, N^{+3}, \tag{3.12}$$

We note that the contribution $\Delta Y^{\mathrm{subox}}$ to the ion-scattering yield is noticeably smaller than the total number of Si atoms in intermediate oxidation states ($N^{\mathrm{tot}} = N^{+1} + N^{+2} + N^{+3}$) because of the weighting factors in the definition of $\Delta Y^{\mathrm{subox}}$. For models A, B, and C the amount and distribution of Si atoms in intermediate oxidation states coincide, and therefore give the same value of 0.8 ML for $\Delta Y^{\mathrm{subox}}$ (Fig. 3.13), to be compared with $N^{\mathrm{tot}} = 1.9$ ML. Data from different photoemission experiments give $\Delta Y^{\mathrm{subox}}$ differing from 0.8 ML by at most 0.15 ML [49, 50, 48, 65].

The differences in the calculated ΔY for the three models originate solely from displacements of substrate Si atoms (Fig. 3.12). In model A, the O bridges cause significant displacements only in the first layer of the substrate leaving deeper ones unperturbed. In models B and C, important distortions propagate for several layers into the substrate.

To further understand the role of particular bonding configurations, we consider three other models, A′, B′, and C′, derived by introducing minor variations with respect to their original counterparts (Fig. 3.14). Model A′ corresponds to an ideally abrupt interface, with the terminating Si layer consisting of Si^{+2} moieties bridged by O atoms and without any other intermediate oxidation state. Model B′ differs from model A′ by the terminating Si layer which consists of Si^{+1} moieties forming in-plane dimer bonds with each other. Model C′ is obtained from the same surface template as for model C, with the omission of the extra Si atom [42].

For models A′, B′, and C′, we obtained average excess Si yields of 0.9, 1.4, and 2.9 ML, respectively. These yields are compared in Fig. 3.15 to those of the previous models and to the experimental yield. Since the respective contributions $\Delta Y^{\mathrm{subox}}$ from intermediate oxidation states (0.75, 0.5, and 0.8 ML) do not vary significantly with respect to those of the previous models (0.8 ML), the variations in ΔY should mainly be assigned to different Si displacements. Models A and A′ only differ by their suboxide distributions, and their yields are found to be close. The low yields calculated for models A′ and B′ show that ideally abrupt interfaces, either with O bridges or in-plane Si dimers in the terminating Si layer, are unable to account for the measured yield. The noticeable difference between the yields of models B′ and B result from the oxidized backbonds in model B, which significantly perturb the Si lattice. The decrease in yield from model C to model C′ quantifies the effect of an extra Si atom in the transition region.

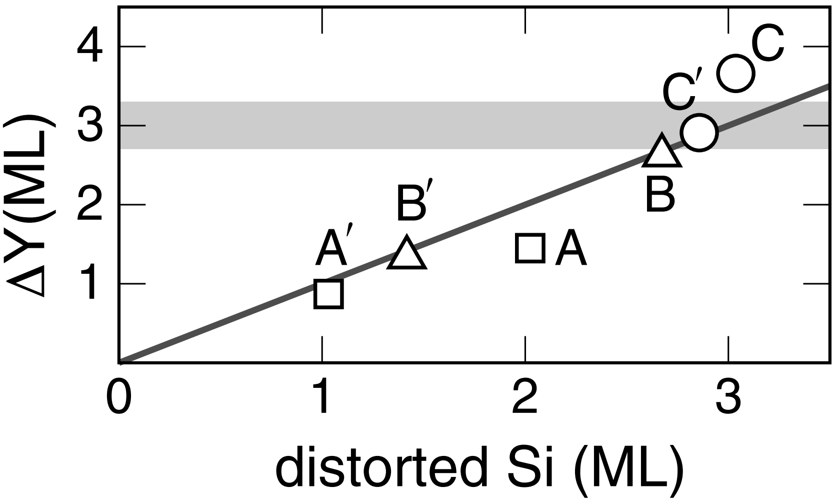

Figure 3.15: Average excess Si yields for all model structures considered here vs number of Si atoms distorted by more than 0.09 Å. The horizontal band corresponds to the experimental result. The line is a guide to the eye.

For each model, we quantify the extent of Si displacements by counting the number of Si atoms of the substrate displaced from regular lattice sites by more than 0.09 Å, corresponding to the sensitivity of our ion-scattering experiment. The plot of excess Si yield vs the number of displaced Si atoms shows a nearly linear trend, indicating a close correlation. To reproduce the experimental yield of about 3 ML, the extent of the Si displacements should match those of models B and C. This level of distortion is achieved in these models by severely perturbing the terminating Si layer, either by backbond oxidation (model B) or by formation of a disordered bonding pattern (model C). Abruptly terminating Si substrates (models A′ and B′), even when moderately perturbed to accommodate intermediate oxidation states (model A), do not present sufficiently large Si displacements.

3.5 Summary

The combination of ion-scattering experiments and theoretical modeling gives new insight into the atomic structure at the Si(100)-SiO$_2$ interface. Significant distortions are found to propagate from the interface into the Si lattice. These distortions are inconsistent with transition structures in which the Si termination is nearly abrupt. The extent of distortions can be accounted for by a terminating Si layer with oxidized backbonds or a disordered bonding pattern. The Si distortion reported here may affect electronic transport close to the interface and contribute to lowering the inversion-layer mobility as compared to its bulk value [119, 120].

Chapter 4

Oxygen diffusion through the oxide layer

4.1 Introduction

The Deal and Grove model assumes that an oxygen species enters the SiO_2 layer, diffuses through the disordered oxide toward the Si-SiO_2 interface, and finally reacts at the Si substrate where new oxide layers are grown [6]. While this model fails in reproducing the oxidation rate during the initial stages, it successfully describes the kinetics of silicon oxidation for thick oxide films [6, 15, 16, 17]. In this regime, the oxide growth is entirely governed by the oxygen diffusion process [6]. Kinetic data for the growth of thick oxide films show that the oxygen solubility depends linearly on pressure and that the activation energy for diffusion is around 1.2 eV [6, 15, 16, 17]. Both observations result in agreement with early oxygen permeation experiments on a silica membrane [18]. Accordingly, these pieces of evidence led respectively (i) to identify the undissociated oxygen molecule as the diffusing species, due to the first-order reaction between external gaseous O_2 and the dissolved species in SiO_2, and (ii) to envisage an O_2 migration through the network without any particular interaction, by similarity with argon, an atom of approximately the same size and activation energy for diffusion in silica [121].

Direct experimental observations have either supported or contrasted the interpretations provided within the Deal and Grove description of the oxygen diffusion process. In fact, while nuclear reaction resonance [33, 34, 7, 36], secondary ion mass spectrometry [35] and medium energy ion scattering experiments [37] based on ^{16}O-^{18}O sequential oxidation all confirmed that the bulk of the oxide does not incorporate oxygen during oxidation and that the new oxide essentially grows at the Si-SiO_2 interface, these experiments also revealed the occurrence of oxygen exchange processes at the external SiO_2 surface. In addition, more recently, oxygen exchange processes were also found to occur at the Si-SiO_2 interface [40, 122], providing support to an interpretation of the oxidation process which favors atomic oxygen as the transported species through the oxide [123].

A few model pictures have so far been proposed for the diffusion mechanism of O_2 in amorphous SiO_2 [124, 12, 125]. However, the suggested mechanisms contrasted, on the one hand, with the homogeneous nature of a continuous random network, generally assumed as structural model of amorphous SiO_2, and, on the other hand, with a diffusion mechanism based on hopping events between solubility sites [124, 125].

Theoretical investigations based on density functional theory appear particularly suitable for providing insight in processes involving oxygen species in SiO_2 [126, 127, 128, 129, 130, 131, 132, 133, 134, 135]. So far, many studies have been devoted to investigating the relative energetics of both neutral and charged oxygen species in α-quartz [126, 127, 128, 129, 130, 133, 135]. The same crystalline structure has been adopted to study the diffusion properties of the peroxyl linkage [126, 129], an atomic network oxygen species favoring oxygen exchange processes [36]. More recently, the effects of the disordered nature of the oxide on the energetics of several oxygen species have been addressed [131, 132]. However, neither the nature of the oxygen diffusing species in amorphous SiO_2 nor the mechanism adopted for the migration in a disordered matrix have yet firmly been elucidated.

In this chapter, we provide an atomic-scale description of oxygen diffusion through the oxide layer during silicon oxidation. In particular, we first focus on the oxygen diffusion process occurring in a region distant from the Si-SiO_2 interface, where the oxide acquires the same properties as amorphous SiO_2 [45]. We adopt in sequence first-principles calculations, classical molecular dynamics, and Monte-Carlo simulations to span the relevant length and time scales for an appropriate description of the long-range diffusion process in a disordered network. Then, we address the oxygen diffusion rate through the oxide layer at the Si-SiO_2 interface. In particular, we investigate the combined effect of disorder and of a dense oxide layer located close to the silicon substrate.

4.2 Model samples for amorphous SiO_2

The oxide distant from the Si-SiO_2 interface corresponds to regular amorphous SiO_2. Hence, we here represent the structural properties of the oxide by a set of independent model structures of amorphous SiO_2. Each model is generated using a classical molecular dynamics approach. In this scheme, the interactions between Si and O atoms are described by the classical potentials proposed in Ref. [70]. We use periodically repeated cubic cells of fixed volume, corresponding to the experimental density of silica (2.2 g/cm^3). Starting from random atomic positions, models of liquid SiO_2 are equilibrated at 3500 K for more than 300 ps. Amorphous structures are then obtained by quenching from the melt with a cooling rate of approximately 7 K/ps [136]. Full simulations lasted from 500 ps to 1 ns, depending on the size of the model structure. We constructed a large set of model structures containing between 72 and 144 atoms in the periodic cell. The full set of models spans an equivalent bulk volume of 574 SiO_2 units.

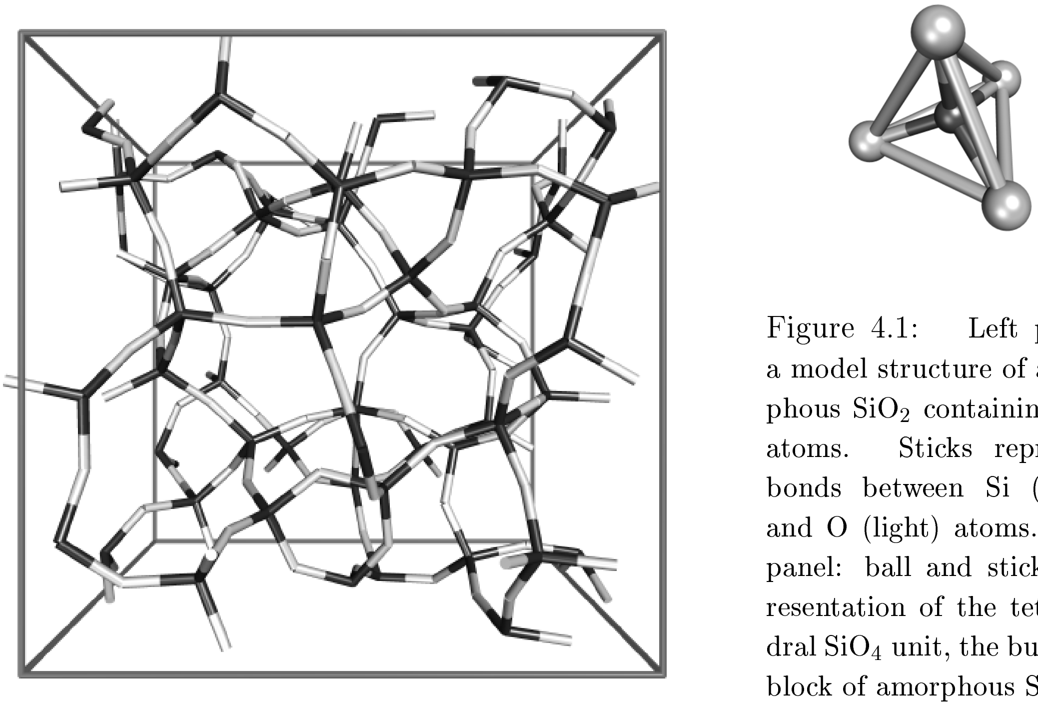

Figure 4.1: Left panel: a model structure of amorphous SiO_2 containing 144 atoms. Sticks represent bonds between Si (dark) and O (light) atoms. Top panel: ball and stick representation of the tetrahedral SiO_4 unit, the building block of amorphous SiO_2.

All the model structures of the oxide consist of a random network of corner-sharing tetrahedral SiO_4 units without coordination defects (Fig. 4.1). The structural parameters in Table 4.1 confirm that the model structures reproduce the typical short-range order of amorphous SiO_2. The Si-O-Si bond angle distribution is characterized by a mean value μ of 152° and a standard deviation σ of 12°, which compare well with the corresponding values extracted from X-ray diffraction (μ=148°, σ=13°) or NMR data (μ=151°, σ=11°) [137, 82]. In addition, the calculated structure factor compares well with neutron diffraction data and shows the characteristic first sharp diffraction peak at about 1.5 Å^{-1} [138]. The agreement stems from a proper description of the intermediate range-order of amorphous SiO_2, even in our smallest model structures (Fig. 4.2).

	Si-Si	Si-O	O-O	Si-O-Si	O-Si-O
μ	3.12	1.61	2.63	152	109.4
σ	0.09	0.02	0.09	12	5.8

Table 4.1: Mean values (μ) and standard deviations (σ) of structural parameters in the model structures of amorphous SiO_2 generated by classical molecular dynamics. Lengths are in angstrom and angles in degrees.

The ring statistics averaged over the full set of model structures has been extracted according to the shortest path analysis [46], and compares well with results of other molecular dynamics simulations (Table 4.2) [136, 139]. In particular, the concentrations of oxygen atoms in three and fourfold rings, 1.2% and 5.3%, respectively, are in fair agreement with recent theoretical estimates derived from Raman spectra of vitreous silica (0.26% and 1.0%) [140].

4.3 Energetics of oxygen species in SiO_2

Thick oxide films (> 200 Å) are opaque to electrons. Electrons and holes might be introduced in the oxide from the conduction or the valence band of the silicon substrate. However, both the conduction-band and the valence-band offsets (~3 and ~4.5 eV, respectively) correspond to high energy barriers which prevent charge carriers to flow through the oxide layer, even at the relatively high temperatures of the oxidation process. Notwithstanding, were electrons available at the SiO_2/O_2 surface, O_2 molecules may become negatively charged and eventually dissociate into charged O ions. In this

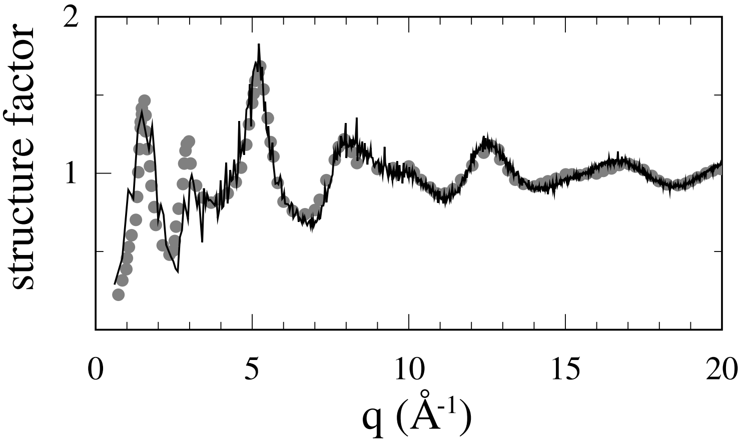

Figure 4.2: Solid line, calculated structure factor for model structures containing 72 atoms. Larger models show the same level of agreement. Grey dots: experimental data [138].

	3	4	5	6	7	8	9	10
present study	0.14	0.63	1.67	1.97	1.24	0.32	0.01	0.00
Ref. [136]	0.09	0.54	1.74	2.10	1.26	0.33	0.03	0.00
Ref. [139]	0.06	0.52	1.40	2.11	1.18	0.40	0.06	0.01

Table 4.2: Average ring statistics in model structures of amorphous SiO_2 generated by classical molecular dynamics. Our results are compared with distributions obtained for larger model structures of 1002 (Ref. [136]) and 648 (Ref. [139]) atoms, generated by similar approaches.

case, electric fields are expected to affect the kinetics of the silicon oxidation process. However, for the oxidation of very thick oxide films, experimental studies have excluded the dependence of growth rates on electric fields, thereby ruling out charged oxygen species as oxidizing agents during silicon oxidation [21, 141, 142, 143, 144]. For this reason, we focus only on neutral oxygen species in the present chapter.

4.3.1 Theoretical approach

To accurately describe the energetics of oxygen species in amorphous SiO_2 we adopt a first-principles scheme based on the density-functional theory [145, 146]. The exchange and correlation energy is accounted for within a generalized gradient approximation [147, 148]. Only valence wave functions are described explicitly while pseudopotentials are used to account for core-valence interactions. We use a normconserving pseudopotential for Si, derived as in Ref. [75], and an ultrasoft pseudopotential for O [76]. Plane-wave energy cutoffs of 24 and 150 Ry are used for the wave functions and the augmented electron density, respectively [72, 73]. Only the Γ-point is used to sample the Brillouin zone. Full structural relaxations are carried out using a damped molecular dynamics scheme [72, 73, 78]. We use a spin-polarized functional to accurately describe the electronic ground state of the oxygen molecule, either in vacuum (its ground state is $^3\Sigma_g$) or in SiO_2 [149, 130]. For the isolated O_2 dimer we find a bond length of 1.26 Å, a dissociation energy of 5.68 eV (the zero-point vibrational energy correction being included), and a vibrational frequency of 1541 cm^{-1}, to be compared with the respective experimental values of 1.22 Å, 5.1 eV and 1578 cm^{-1} [150].

The energy of an oxygen species in an atomistic model for the oxide is referred to the energies of the unperturbed oxide and of the isolated O_2 molecule.

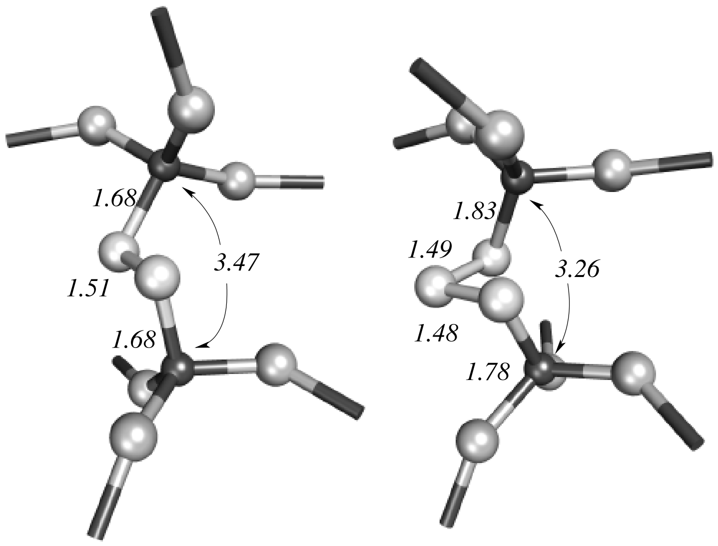

Figure 4.3: Peroxyl (left) and ozonyl (right) linkages in α-quartz. Some bond distances are indicated. Dark and light balls represent Si and O atoms, respectively.

4.3.2 O species in α-quartz

The incorporation of oxygen in the oxide layer from the gas phase can lead to the formation of either molecular or, upon dissociation, atomic O species. Both the atomic and the molecular O species in SiO_2 can give rise to network or interstitial defects. In fact, the additional O atom or O_2 molecule can be inserted within a Si-O-Si bonding structure of the SiO_2 network to form the peroxyl and ozonyl linkage, respectively (see Fig. 4.3) [126, 128]. On the other hand, O and O_2 can maintain their individuality and find equilibrium positions within the interstitial cages of the SiO_2 network (see Fig. 4.4). All these O species have been suggested to play an important role during silicon oxidation [6, 36, 126, 128, 123].

Most theoretical studies usually adopt α-quartz, the most stable crystalline phase of SiO_2 at standard ambient conditions, as a model for amorphous SiO_2 [126, 128, 127, 129, 130, 134]. To allow comparison with previous theoretical studies, we first investigate the relative energetics of the O species described above in this crystalline material. To model α-quartz, we use a periodic orthorhombic cell containing 72 atoms with fixed cell parameters of 9.9422 Å× 8.6099 Å× 10.9085 Å, corresponding to the theoretical lattice constants [151]. We find that the interstitial O_2 molecule with spin S=1 is the most stable O species in α-quartz. The O_2 molecule is found to be approximately oriented along the c-axis, showing a small tilt of 14° (Fig. 4.4). Upon relaxation, the nearby Si and O atoms of the α-quartz network move away from the O_2 molecule by 0.1–0.2 Å and 0.2–0.5 Å, respectively. The energy of the interstitial O_2 is found to be higher than that of the free molecule by 3.4 eV. The spin state S=0 is found to be higher than the S=1

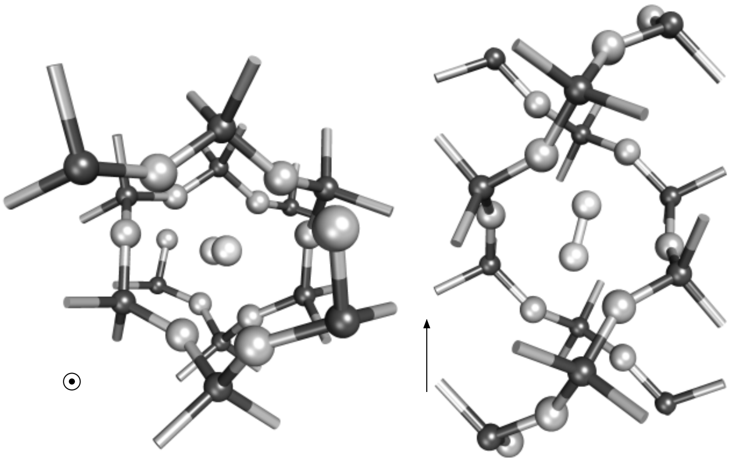

Figure 4.4: Interstitial molecular oxygen in α-quartz. The left (right) panel gives a view along a direction parallel (orthogonal) to the **c**-axis. Dark and light balls represent Si and O atoms, respectively.

state by 0.3 eV. The interstitial molecular species with S=1 is found to be considerably more stable than two isolated interstitial O atoms (ΔE=3.2 and ΔE=3.4 eV for spin states of S=0 and S=1, respectively).

The network oxygen species, the oxzonyl and the peroxyl linkages, are found at higher energies, ΔE=1.0 and ΔE=1.6 eV per pair of O atoms. The relaxed atomic structures of these configurations are illustrated in Fig. 4.3. The lower energy of the ozonyl linkage with respect to the peroxyl bridge is consistent with the distance between the Si atoms which accommodate these oxygen species. For the peroxyl bridge this distance is found to be 3.47 Å, significantly longer than the value of this distance in the non-defected α-quartz model (3.09 Å). The ozonyl linkage gives rise to a Si-Si distance of 3.26 Å, indicating that this species can be more easily accommodated in the α-quartz network.

Our results show overall good agreement with previous first-principles calculations [126, 128, 127, 129, 130, 134]. Nevertheless, the comparison with some theoretical investigations reveals differences which cannot simply be attributed to technicalities [126, 128]. The critical analysis of these discrepancies highlights the importance of spin polarization effects in describing the energy of the interstitial O_2 in SiO_2 [126, 128, 130, 133].

4.3.3 O species in amorphous SiO_2

Since the oxide grown during silicon oxidation is amorphous, the use of α-quartz as a reference model is questionable. In fact, it has already been recognized that α-quartz poorly mimics amorphous SiO_2 as the host matrix for oxygen species [131, 132]. Hence, we extend our investigation in this section adopting amorphous model structures for SiO_2. We use two periodic model structures of amorphous SiO_2 in which the disordered nature of the oxide is modeled by 72 independent atoms at the experimental density. In

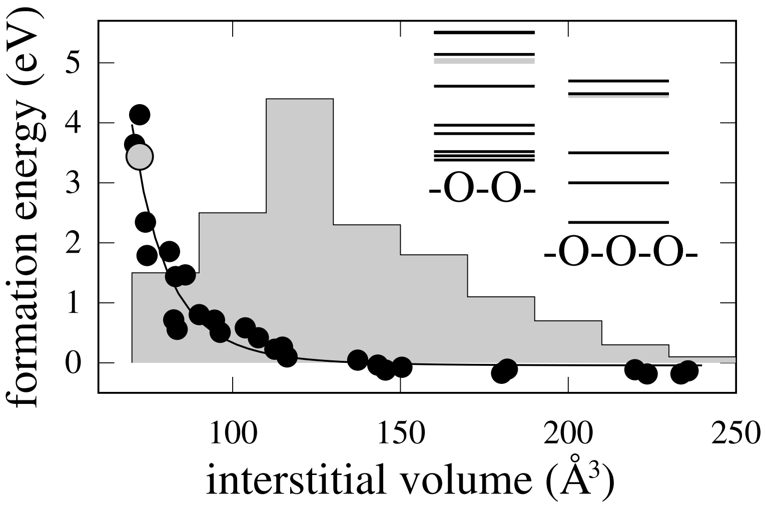

Figure 4.5: Formation energies for oxygen species in amorphous SiO_2 (black) and α-quartz (gray) calculated within a density-functional approach. Discs refer to the energy of the O_2 molecule in interstitials of different volume. The solid line is a guide to the eye. The interstitial volume corresponds to that of the largest ellipsoidal void centered on the O_2 molecule. The distribution of interstitial voids available for the O_2 molecule in amorphous SiO_2 is showed by the shaded histogram. Energy levels of the peroxyl and ozonyl linkages are indicated on the same energy scale.

addition to a model structure, obtained previously by first-principles molecular dynamics [152, 153], we generated a novel model structure by classical molecular dynamics [70, 136] (cf. Sec. 4.2). Structural differences between the two models are essentially limited to the ring statistics and to the distribution of interstitial volumes.

In the case of amorphous SiO_2, we consider the interstitial O_2 molecule and the two network species, the peroxyl (-O-O-) and ozonyl (-O-O-O-) linkages. We disregard the interstitial atomic species on the basis of its high formation energy in α-quartz. To account for the statistical variety of sites, we introduce the oxygen molecule within the available interstitial cages offered by the network, while for the peroxyl and ozonyl linkage, we select a set of Si-O-Si units showing different bond angles for constructing their initial configuration. The defected structures are then relaxed within the first-principles scheme in order to determine the ground state configurations. Formation energies are assigned per pair of O atoms, with respect to the energy of the undefected SiO_2 model structure and of the isolated O_2 molecule. The results of this study are reported in Fig. 4.5.

We find formation energies for the network species, the peroxyl and ozonyl linkages, spread around the values calculated for α-quartz (Fig. 4.5), without any apparent correlation with the Si-O-Si bond angle of the undefected SiO_2 structure [131]. At variance, the formation energy for interstitial molecular oxygen shows a strong correlation with the size of the interstitial void, strongly decreasing for increasing cage sizes (Fig. 4.5). In particular, note that most of the interstitial voids in our amorphous models are significantly larger than in α-quartz (Fig. 4.5). For selected configurations, we also evaluated the formation energy of molecular oxygen in its singlet state. We always found that the singlet state is at higher energies than its corresponding triplet state, by approximately the same amount ($\sim$0.3 eV) as in α-quartz. This result is consistent with a recent first-principles study on the influence of spin on the O_2 diffusion properties in α-quartz [130]. Indeed, in this investigation it is reported that along the diffusion pathway the triplet state lies in energy below the singlet state and the energy differences vary between 0.9 eV and 0.3 eV [130].

From our first-principles calculations we conclude that O_2 is the most stable neutral oxygen species in both crystalline and amorphous SiO_2. Its relative stability with respect to network species is enhanced in amorphous SiO_2 by the presence of larger voids.

4.3.4 Geometrical analysis of void distribution in a-SiO$_2$

The first-principles investigation in the previous sections promotes the interstitial O_2 molecule as the most likely candidate for being the migrating oxygen species during oxidation and shows that equilibrium sites for O_2 are located in interstitial voids. In this section, we characterize the interstitial void distribution in amorphous SiO_2 in order (*i*) to determine the concentration of equilibrium sites for O_2 and (*ii*) to examine whether a diffusion mechanism based on the hopping of an O_2 molecule between such sites is possible. To address these issues, we adopt an extended set of continuous random network models for amorphous SiO_2 (cf. Sec. 4.2) for deriving the interstitial void distribution on the basis of a geometric Voronoi analysis (see [154, 155] and references therein).

In the Voronoi analysis of a disordered network, the space is partitioned in polyhedra, each containing the volume nearest to a given atom. The vertices of these polyhedra have the property of being equidistant to at least four atoms of the SiO_2 network. Thus, the Voronoi analysis associated to a disordered distribution of atoms directly leads to the definition of spheres characterizing the distribution of interstitial voids. Recently, this definition of interstitial voids has also been used to investigate the origin of the first

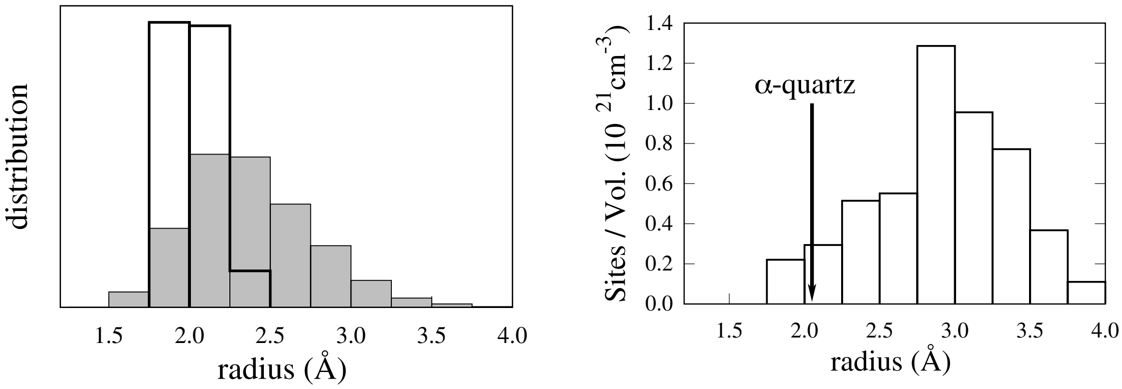

Figure 4.6: Left panel: distribution of radii of interstitial voids in α-quartz (thick-solid line, open histogram) and in the model structures of amorphous SiO_2 generated in this work (filled histogram). The interstitial voids are defined using a Voronoi analysis. Right panel: concentration of interstitial voids, extracted by the Voronoi analysis, whose center is not included in a void of larger radius. The arrow gives the result for α-quartz.

sharp diffraction peak appearing in the structure factor of disordered network-forming materials [155, 156].

We applied the Voronoi analysis on both α-quartz and on our set of model structures of amorphous SiO_2 (see Fig. 4.6). Interstitial voids in α-quartz show radii closely distributed around 2.0 Å. In amorphous SiO_2, the distribution of radii is shifted toward higher values (average radius of 2.4 Å), and is remarkably broader. However, it appears unreasonable to associate, on a one to one basis, interstitial voids defined in this way to equilibrium sites for the O_2 molecule. In fact, careful inspection of the set of such interstitial voids shows that the centers of a large number of voids are located within voids of larger radius. Since such smaller voids are presumably all associated to the same equilibrium site for the interstitial O_2 molecule, it is physically more reasonable to omit these voids from the considered set.

The retained interstitial voids give the distribution of radii shown in the right panel of Fig. 4.6. In α-quartz, this procedure gives a single radius (2.05 Å). In the amorphous models, most of the interstitial voids now have radii larger than in α-quartz, showing an average radius of 2.9 Å, approximately corresponding to an interstitial volume of 110 $Å^3$ and a formation energy of less than 1 eV. In view of the results in Fig. 4.5, this suggests that these voids are good candidates for equilibrium sites of the interstitial O_2 molecule. Under this assumption, we derived the value of $5.1 \cdot 10^{21}$ cm^{-3} for the concentration of equilibrium sites of O_2 in amorphous SiO_2. By considering voids with overlapping spheres as nearest neighbors, we found an average distance between nearest neighbor equilibrium sites of 4.7 Å. The size of this distance is consistent with a diffusion mechanism based on hopping events of the O_2 molecule between equilibrium sites. We note that this consideration is solely made on the basis of the distribution of equilibrium sites. In fact, a conclusive assessment still requires the study of the potential energy landscape connecting these sites.

4.4 Energy landscape for O_2 in *a*-SiO_2

Understanding the properties of the O_2 migration through the oxide layer requires the consideration of its disordered nature. In case of a crystalline material, evaluating the activation energy, for instance, crudely means identifying the energy required to move from one equilibrium site to a neighboring equivalent one [126]. Amorphous SiO_2, however, offers a variety of interstitials as equilibrium sites for O_2 and furthermore, the transition energies required for going to neighboring, non-necessarily equivalent, O_2 minima depend on the local environment. Furthermore, a geometrical issue emerges in treating the O_2 diffusion problem in amorphous SiO_2: the connectivity of the disordered network of interstitials. Therefore, to investigate this diffusion problem, it is necessary to explore both the energetic and geometric properties of the interstitial network. Using a first-principles approach is impracticable and therefore it is appropriate to resort to a simpler and computationally more advantageous scheme.

4.4.1 Energy of the interstitial O_2 molecule in SiO_2: A classical scheme

To extensively sample the properties of the disordered network of interstitials in amorphous SiO_2, we construct a simplified energy scheme based on classical interatomic potentials. For the Si and O atoms of the SiO_2 network, we adopt interatomic potentials used for generating the model structures of amorphous SiO_2 (Sec. 4.2), while a new set of potentials is derived to account for the interaction between the O_2 molecule and the oxide network. In particular, the interaction between the O atoms within the molecule is described by a Morse potential whose parameters are directly obtained from the bond-length, the dissociation energy, and the harmonic force-constant calculated by first-principles (Sec. 4.3.1). For the O_2-SiO_2 interaction, we adopt Lennard-Jones-like potentials. More precisely, for each oxygen atom i (i=1,2) of the O_2 molecule, the potential:

$$V_x^i = \epsilon_x \left(\frac{\sigma_x}{r_{ix}}\right)^{n_x} - \gamma_x \left(\frac{\rho_x}{r_{ix}}\right)^{m_x} \tag{4.1}$$

x	ϵ (eV)	σ (Å)	n	γ (eV)	ρ (Å)	m
O	2.46	1.99	7	1.07	2.11	6
Si	1.44	1.99	9	0.39	0.37	6

Table 4.3: Parameters of the Lennard-Jones-like interatomic potentials describing the interaction between the interstitial O_2 molecule and the SiO_2 network.

describes the interaction with an atom of the species x, x=Si or O, of the SiO_2 network. The free parameters are derived from a fit of the formation energies of interstitial O_2 in amorphous SiO_2 obtained from first-principles (Fig. 4.5). The obtained parameters are reported in Table 4.3.

The full classical scheme well reproduces the energetics of an interstitial O_2 molecule in amorphous SiO_2. In agreement with first-principles data, the classical scheme either reproduces or predicts O_2 local minima within a rms error of about 0.1 eV (Fig. 4.7, left panel). Moreover, to verify the reliability of this simplified scheme in describing transition states, we generate within the classical scheme several O_2 migration paths (Sec. 4.4.2). An energy comparison between the classical and first-principles schemes for a discrete set of configurations along these paths shows that the absolute error raises along the transition path, acquiring its largest value at the transition state (Fig. 4.7, right panel). We note that the error does not derive from the O_2-SiO_2 interaction, which is overall well described by our modeling scheme, but rather from the relaxation of the SiO_2 network which directly results from the adopted interatomic potentials [70]. During the O_2 diffusion process, even for transition energies as high as 2.2 eV, the energy along the migration path is dominated by the O_2-SiO_2 interaction, the SiO_2 deformation contributing by at most 20%. This results in an overall error of about 10% for the classical scheme with respect to the first-principles one. Therefore, the good agreement with the accurate first-principles scheme stems from the accurate description of the O_2-network interaction which dominates the structural relaxation (Fig. 4.7). We refer to Ref. [157] for a more detailed comparison between vibrational energies of SiO_2 as given by first-principles and by the classical potentials in Ref. [70].

4.4.2 Energetics and topological properties

To investigate the potential energy landscape for O_2 in amorphous SiO_2, we use the classical scheme (Sec. 4.4.1) and span the volume represented by the full set of model structures for this material generated by classical molecular dynamics (Sec. 4.2). We first focus on minima. We insert the O_2 molecule randomly in the model structure of the

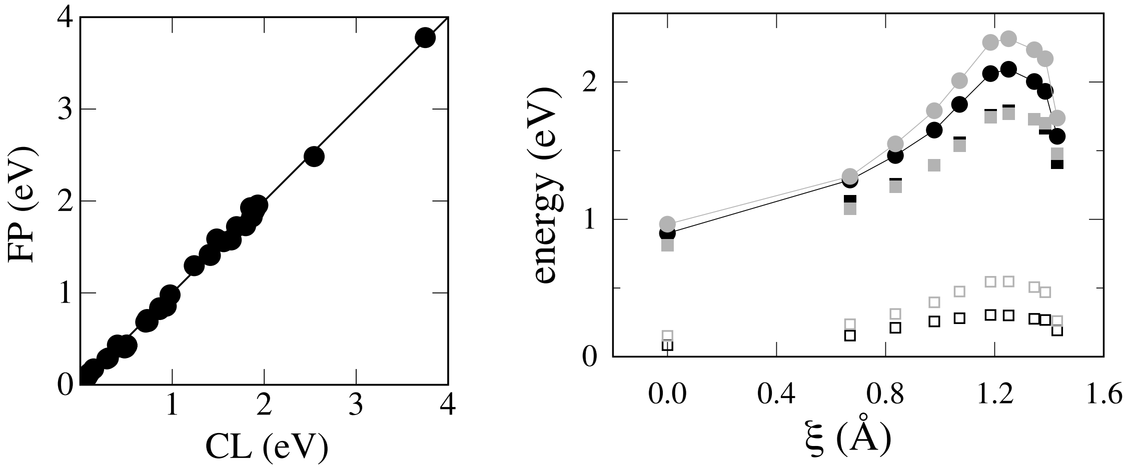

Figure 4.7: Comparison between the classical (CL) and first-principles (FP) schemes. Left panel: O_2 formation energies at the equilibrium sites are compared. The straight line indicates the ideal agreement. Right panel: Comparison between the first-principles (black) and classical (gray) scheme in reproducing the energetics along a transition path between two nearest neighbor minima in amorphous SiO_2. Contributions to the energy (discs) from the SiO_2 relaxation (open squares) and the O_2-SiO_2 interaction (closed squares) are indicated separately.

oxide and adopt a damped molecular dynamics approach for finding the corresponding equilibrium position. For each model structure of amorphous SiO_2, the procedure is repeated until convergence on the number of local minima is reached. As a result of the disordered nature of the oxide, the energy distribution of local minima shows a finite spread (Fig. 4.5). In agreement with the first-principles results obtained for a limited set of cases (Sec. 4.3.3), essentially all these energies remain well below those of network oxygen species. The distribution of O_2 minima in amorphous SiO_2 is well described by an exponential function with a decay constant of 0.58 eV. The mean values of both the energy and the density distribution are similar for the various model structures of the oxide. This suggests that minima are poorly correlated with specific structural features and that they are uniformly distributed in amorphous SiO_2. We find a concentration of local minima for O_2 in amorphous SiO_2 of $5.4 \cdot 10^{21}$ cm^{-3}, corresponding to an average distance between solubility sites of 5.7 Å. We note that this distance is very close to the value of 4.7 Å, extracted on the basis of simple geometrical criteria from the distribution of Voronoi spheres (Sec. 4.3.4). The slight difference should be attributed to the unphysical statistical weight assigned to small interstitials when adopting the geometrical criterion.

The average distance of 5.7 Å between nearest neighbor minima for O_2 in the disordered oxide is considerably smaller than the value of 26 Å reported in Ref. [125] from

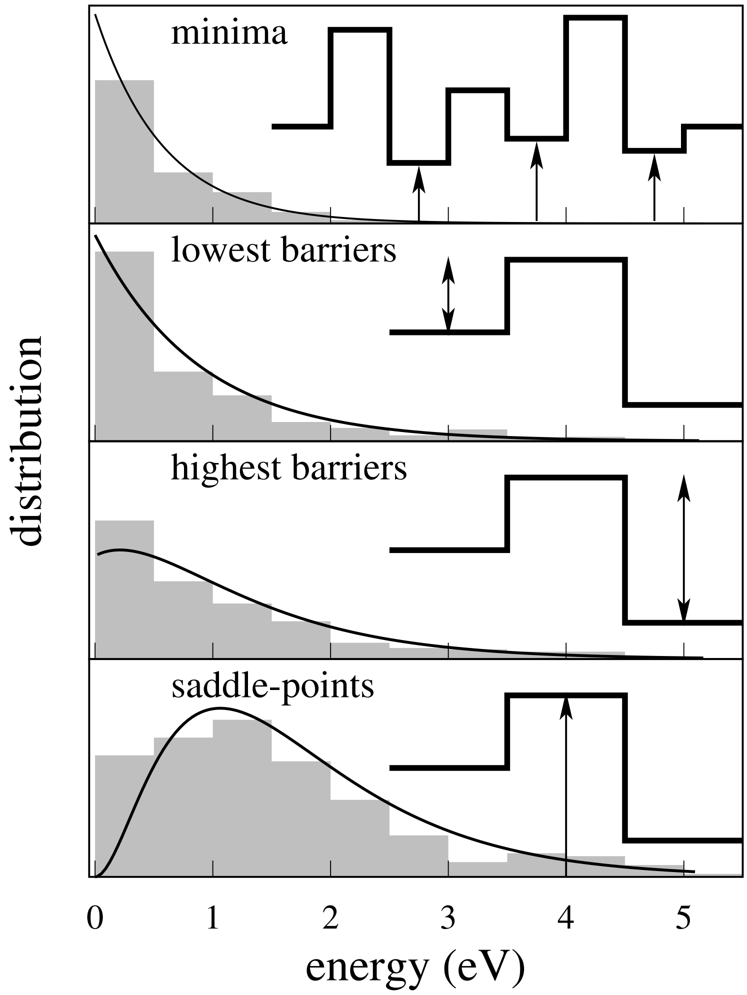

Figure 4.8: From top to the bottom, energy distribution of minima, lowest barriers, highest barriers, and saddle points, for O_2 in amorphous SiO_2. The energy reference is as in Fig. 4.5. Histograms refer to distributions obtained exploring model structures for the oxide within the classical scheme while solid lines correspond to derived continuous distributions. Exponential decaying functions well fit distributions of minima and lowest barriers. Convolutions of these energy distributions give distributions for highest barriers and saddle points (solid lines) in agreement with those extracted from model structures.

which a diffusion mechanism through anomalous crystalline channels was assumed. It is worth noting that the physical picture in Ref. [125] was constructed on the clearly inadequate assumption that all solubility sites have equal energy [125]. Contrarily, our results highlight the existence of a uniform distribution of interstitials in amorphous SiO_2 forming a disordered network of interconnected equilibrium sites whose average distance favor a diffusion mechanism based on hops between neighboring minima.

To explore energy barriers between interstitials and accordingly determine the connectivity features of the disordered network of local minima, we adopt the classical scheme described above for searching saddle points. To this end, we applied two different methods, the activation relaxation technique (ART) [158] and a dragging procedure [159]. In the ART technique, a system is driven from a local minima to a saddle point by partially reversing the restoring force [158]. In our particular case, the transition states can be found by using a reaction coordinate corresponding to the translational motion of the O_2 molecule from a particular equilibrium site to a nearest neighboring one. Therefore, we simplify the ART technique reversing only the forces associated to the translational degrees of freedom of the O_2 molecule. In addition, with respect to the original ART formulation [158], the coefficient controlling the percentage of the reversed force component is varied during the ART evolution in order to execute displacements of the O_2 center of mass of $5{\cdot}10^{-4}$ Å. Such a constant slow evolution rate allowed us to construct transitions pathways for the O_2 molecule in which the SiO_2 network is fully relaxed at each step. In particular, for each local minimum, after having randomly displaced the O_2 molecule from equilibrium, ART is applied to generate the transition path leading across a saddle point to another nearest neighbor local minimum. This procedure is repeated for each local minima until convergence on the number of discovered nearest neighbor minima is reached.

To validate this approach, we also determine saddle points and connections using a constrained molecular dynamics technique [159]. For each pair of local minima, the center of mass of the O_2 molecule is continuously dragged across the SiO_2 network from one local minimum to the other. At each step of the dragging procedure, we reduce the distance between the O_2 molecule and the target minimum by $5{\cdot}10^{-3}$ Å and determine the ground state configuration of the system while the O_2-minimum distance is kept fixed. The paths through the SiO_2 network is interrupted if, during the evolution, the O_2 molecule meets another local minimum. The saddle point energies and number of nearest neighbor minima obtained with the two approaches coincide. The results of this investigation are reported in Fig. 4.8.

Non-equivalent local minima share asymmetric barriers. The distribution of the lowest barriers between nearest neighbor minima is well reproduced by an exponential function with a decay constant of 0.88 eV. Moreover, from the statistical analysis of our data results that minima and lowest barriers are uncorrelated quantities. In fact, we verified that distributions of highest barriers and saddle points are properly reproduced by those obtained by convolving the distributions of minima and lowest barriers (Fig. 4.8).

The search for transition states between nearest neighbor local minima also gives access to a statistical characterization of the geometrical properties of random networks of interstitials in amorphous SiO_2. In fact, we obtain the distribution of distances between nearest neighbor equilibrium sites for O_2 in the oxide (Fig. 4.9, left panel). The average distance between nearest neighbor local minima extracted from this distribution results 5.3 Å, only slightly different from that estimated on the basis of the concentration of minima in amorphous SiO_2 (5.7 Å). Most importantly, we have access to the connec-

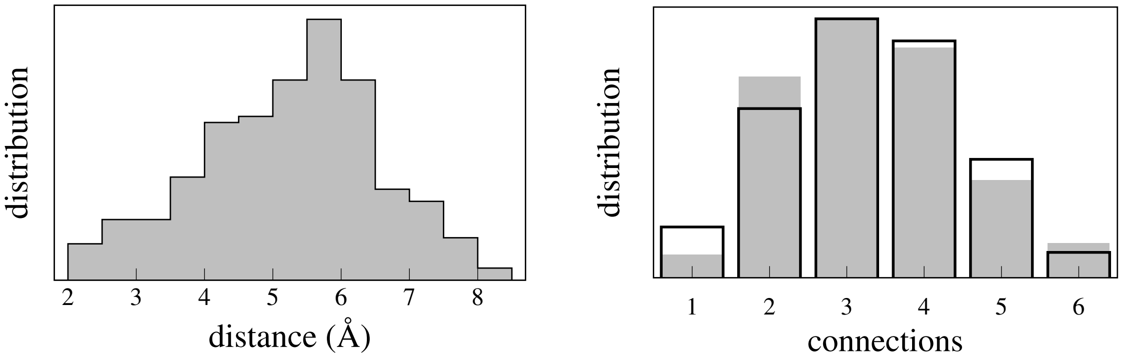

Figure 4.9: Left panel: distribution of distances between nearest neighbor local minima for interstitial O_2 in amorphous SiO_2. Right panel: distribution of connections between nearest neighbor local minima. A sixth-degree binomial distribution with coefficient 0.55 (open histogram) well reproduces data extracted from the model structures of the oxide (filled histogram).

tivity properties of the random network of local minima (Fig. 4.9, right panel). The number of connections per node extends from 2 to 6, with an average number of 3.3. The distribution of connections extracted from the model structures of the oxide is well reproduced by a sixth-degree binomial distribution with coefficient 0.55. This suggests that even connections between nearest neighbor minima are distributed independently.

4.4.3 O_2 solubility in amorphous SiO_2

We now suppose a *gas* of independent O_2 molecules dissolved in the interstitials of amorphous SiO_2 in chemical equilibrium with a gas of free molecules. We aim at obtaining an estimate of the O_2 solubility in amorphous SiO_2 on the basis of the quantities extracted previously for the equilibrium sites. Hence, according to classical thermodynamics [160, 161, 162], we can write:

$$\mu^{O_2}_{\text{vacuum}} = -k_B T \ln\left(\frac{\mathcal{Z}^{O_2}_{\text{vacuum}}}{N^{O_2}_{\text{vacuum}}}\right) = \mu^{O_2}_{SiO_2} = -k_B T \ln\left(\frac{\mathcal{Z}^{O_2}_{SiO_2}}{N^{O_2}_{SiO_2}}\right) \tag{4.2}$$

where $\mu^{O_2}_{\text{vacuum}}$, $\mathcal{Z}^{O_2}_{\text{vacuum}}$, $N^{O_2}_{\text{vacuum}}$ and $\mu^{O_2}_{SiO_2}$, $\mathcal{Z}^{O_2}_{SiO_2}$, $N^{O_2}_{SiO_2}$ are the chemical potential, the partition function and the number of O_2 molecules in vacuum and amorphous SiO_2, respectively. T is the temperature and k_B the Boltzmann constant. From Eq. (4.2), we therefore deduce:

$$N_{SiO_2} = N_{\text{vacuum}} \frac{\mathcal{Z}^{O_2}_{SiO_2}}{\mathcal{Z}^{O_2}_{\text{vacuum}}}. \tag{4.3}$$

Considering a volume $V_{\mathrm{SiO_2}}$ of oxide, we account for the distribution of interstitials where the O_2 molecule has different energies with respect to the vacuum and write $\mathcal{Z}^{\mathrm{O_2}}_{\mathrm{SiO_2}}$ as follows:

$$\mathcal{Z}^{\mathrm{O_2}}_{\mathrm{SiO_2}} = V_{\mathrm{SiO_2}}\mathcal{N}_{\mathrm{SiO_2}}\int m(E)\mathcal{Z}^{\mathrm{O_2}}_{\mathrm{V(E)}}dE, \tag{4.4}$$

where $\mathcal{N}_{\mathrm{SiO_2}}$ is the concentration of solubility sites in $V_{\mathrm{SiO_2}}$, $m(E)$ the energy distribution of local minima for O_2 in the oxide, and $\mathcal{Z}^{\mathrm{O_2}}_{\mathrm{V(E)}}$ the partition function for O_2 in amorphous SiO_2, where the spatial integration is limited to the volume $V(E)$ associated to the equilibrium site of energy E. Evaluating Eq. (4.4) to obtain the solubility $n_{\mathrm{SiO_2}}$ ($n_{\mathrm{SiO_2}} = N_{\mathrm{SiO_2}}/V_{\mathrm{SiO_2}}$) at a certain temperature and pressure is a difficult task [162]. By assuming a uniform distribution of identical solubility sites, early investigations estimated the binding energy of rare gases and inert molecules in amorphous SiO_2 by direct comparison with experiments [163, 164]. More recently, Monte-Carlo simulations based on interatomic potentials addressed the calculation of Eq. (4.3) for rare gases dissolved in amorphous SiO_2 obtaining a qualitative agreement with experiments [161]. Here, our scope is to provide an estimate for the O_2 solubility in amorphous SiO_2 on the basis of crude approximations [162]. In particular, we assume that within a specific volume around each local minima, the molecule is completely free to move, rotate and vibrate, as in vacuum. Such a volume is defined as the sphere centered on the equilibrium site for the O_2 molecule with radius equal to the distance to the closest saddle point. Under such assumptions, the O_2 molecule can occupy a distribution of volumes in amorphous SiO_2 where it has different energies (see Fig. 4.5). From Eqs. (4.3) and (4.4) we finally obtain:

$$n_{\mathrm{SiO_2}} = \frac{p}{k_BT}\mathcal{N}_{\mathrm{SiO_2}}\int m(E)V(E)\exp\left(-\frac{E}{k_BT}\right)dE \tag{4.5}$$

where we used the partition function of an ideal gas of O_2 at pressure p. Adopting the distribution for local minima extracted from the model structures (Fig. 4.8), for a pressure of 1 atm and a temperature of 1078°C, we obtain a solubility of $n_{\mathrm{SiO_2}}$=$15.8\cdot10^{16}$ cm^{-3}. At the same thermodynamic conditions, the experimental value is $5.5\cdot10^{16}$ cm^{-3} [18]. The fact that theory and experiment give the same order of magnitude should be considered very satisfactory. Indeed, the observed error for the solubility corresponds to an error of about 0.1 eV on the energy scale, well within the uncertainty of our level of theory.

4.5 O_2 diffusion in amorphous SiO_2

The average energy barrier between neighboring local minima for O_2 in amorphous SiO_2 is around 0.67 eV. This value is sufficiently high for assuming that, during diffusion, dynamical correlation effects, such as recrossing events or consecutive multiple jumps, are negligibly small [165]. Under this assumption, the transition-state-theory, which defines transition rates according to the relative energy position of minima and saddle points [166], constitutes a suitable approach for studying the diffusion process. In this framework, the statistical properties of the O_2 energy landscape in amorphous SiO_2 (Figs. 4.8 and 4.9) are the only relevant ingredients for studying the diffusion process.

4.5.1 Random lattice model

To represent an extended region of the oxide, we consider a cubic lattice model of 30×30×30 sites. Each site mimics an interstitial void in amorphous SiO_2 where the O_2 molecule finds an equilibrium position, whereas each bond between first nearest neighbor lattice sites represents the transition path between two nearest neighbor local minima for O_2. Energies for local minima (sites) and transition barriers (lowest barriers) are mapped onto the lattice model according to the continuous distributions derived by fitting those extracted from model structures of the disordered oxide (see Fig. 4.8).

The distribution of connections between nearest neighbor local minima is well reproduce by the binomial function:

$$\mathcal{B}_N^p(n) = \frac{N!}{n!(N-n)!}p^n(1-p)^{N-n} \qquad n = 1 \dots N \tag{4.6}$$

with N=6 and p=0.55. Hence, to reproduce the connectivity of the network of interstitials for the O_2 molecule in amorphous SiO_2, we assign finite energy barriers to only 55% of the bonds, while the remaining bonds are omitted (infinite energy barrier) (Fig. 4.9, right panel). Because of the absence of important correlations in the potential energy landscape for O_2 in the oxide, energies and connections are then distributed at random. A schematic representation of the resulting *disordered* lattice model is given in Fig. 4.10. In consideration of the average distance between nearest neighboring equilibrium sites of 5.7 Å, the final random lattice model corresponds to a cubic sample of amorphous SiO_2 with a side of 17 nm.

4.5.2 Monte-Carlo simulations

According to the transition-state theory, transition rates between nearest neighboring equilibrium sites are defined according to the relative energy barriers and attempt frequencies [166]. In our simulations, the attempt frequencies, or equivalently the rattling time within local minima, are supposed to be identical and independent of the energy of the equilibrium site. Distances between equilibrium sites are also assumed to be

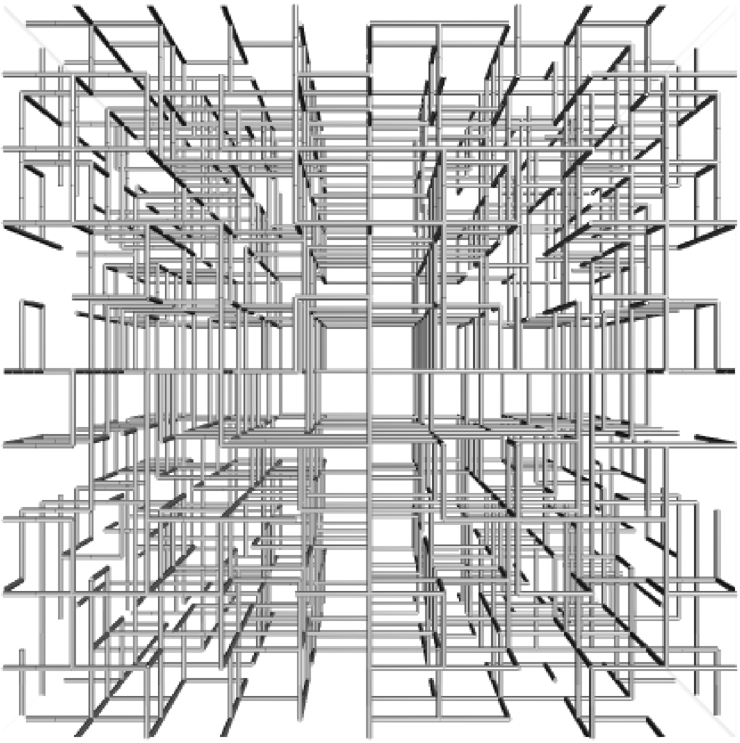

Figure 4.10: A lattice model of 10×10×10 sites on which the distribution of connections between nearest neighbor interstitials for the O_2 molecule in amorphous SiO_2 has been mapped. The original cubic lattice model now appears topologically *disordered.* Another source of disorder comes from the broad spectrum of energies mapped onto the sites (minima) and the bonds (barriers) of this lattice model.

identical to an arbitrary length unit. Of course, rattling times and distances between local minima of course constitute important aspects for describing a diffusion process [165]. However, in normal conditions, namely for distributions of distances and waiting times with finite first and second moments, these elements mainly affect the absolute value of the diffusion coefficient. For the diffusion of O_2 in SiO_2 this condition for the distances is satisfied (see Fig. 4.9, left panel). We assume that this condition also holds for the waiting times. Since the O_2 molecule visits only a very limited set of energies during diffusion (see next section), it is reasonable to assume that the waiting times are distributed closely around a given value. We here aim at calculating the effective activation energy for diffusion, a quantity strictly related to the energetical and topological properties of the potential energy landscape.

To find the effective activation energy for diffusion of O_2 in the oxide, we distribute a set of 1000 independent moving particles (O_2 molecules) on the random lattice model (disordered network of interstitials in amorphous SiO_2). The particles are then evolved at a specified temperature by adopting the Metropolis Monte-Carlo algorithm [167]. In particular, at each Monte-Carlo step, for a specified diffusing particle at the lattice site i, a transition path (bond i_l) toward another nearest neighboring equilibrium site j is chosen at random and the particle is transferred in j according to the probability

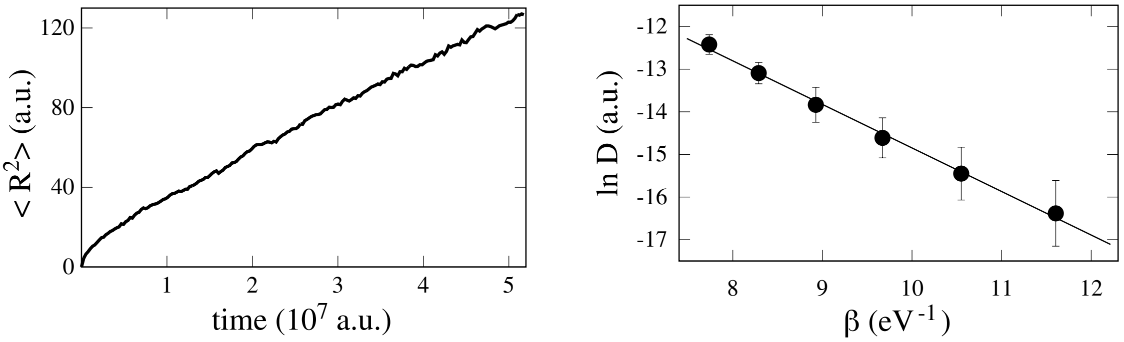

Figure 4.11: Left panel: average mean square displacement of the diffusing particles vs. time at 1200 K. Right panel: logarithm of the diffusion coefficient extracted from Monte-Carlo simulations at different temperatures ($\beta = 1/k_\mathrm{B}T$). Each of the diffusion coefficients (discs) is obtained as an average over eight simulations. The errorbars are the relative rms deviations.

$\exp(-E_b^{i_l}/k_\mathrm{B}T)$, where $E_b^{i_l}$ is the energy barrier associated to the transition $i \rightarrow j$ and T the temperature.

At low temperature, the diffusion coefficient obtained by the Monte-Carlo simulations converges slowly. To increase the efficiency of the scheme, we therefore adopt a modified version of the Monte-Carlo algorithm [168]. The acceleration is achieved by raising the energy values of all minima by a small amount ϵ. This modification does not alter neither the equilibrium distribution of particles in the local minima nor the relative transition rates between nearest neighbor sites. However, absolute values for transition rates has to be renormalized by scaling the unit time length by a factor $\exp(\epsilon/kT)$. The time explored by the Monte-Carlo simulation increases by the same factor. By adopting small values for ϵ, the particle dynamics is altered only at short times because of the modified energy landscape. At variance, the long-range diffusion properties are determined by energy barriers greater than ϵ and are therefore result preserved [168]. We use ϵ=0.17 eV. With this value, diffusion coefficients extracted from Monte-Carlo simulations on modified energy landscapes coincide with those obtained using unmodified ones.

4.5.3 The effective activation energy for O_2 diffusion

During the Monte-Carlo simulations on random lattice models, the average mean position and displacement follows a normal diffusive behavior [169]. After an initial sublinear regime, the average mean-square-displacement increases linearly with time (Fig. 4.11, left panel). Thus, from each Monte-Carlo simulation, we derive a diffusion coefficient using Einstein's relation [169]. At each temperature, several Monte-Carlo simulations

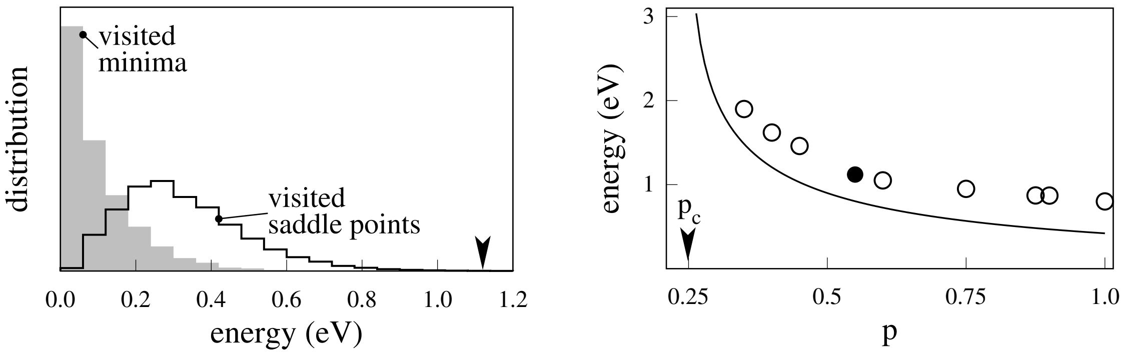

Figure 4.12: Left panel: distributions of minima and saddle points visited during a Monte-Carlo simulation at a temperature of 1200 K on a cubic lattice defined by p=0.55. The arrow indicates the calculated activation energy for temperatures between 1000 and 1500 K. Right panel: activation energy obtained by Monte-Carlo simulations (dots) for the diffusion on a cubic lattice vs. the probability p of introducing connections between neighboring sites. The black dot corresponds to the connectivity in disordered SiO_2 (p=0.55). For comparison, we also consider a model in which all the equilibrium sites are at the same energy (solid), and for which the activation energy can be derived from the distribution of transition energies using the percolation threshold for a cubic lattice (p_c=0.248812) [168].

are performed for different configurations of the random lattice. Results are reported in Fig. 4.11.

Diffusion coefficients are estimated at temperatures ranging from 1000 K to 1500 K, which correspond to typical temperatures adopted during silicon oxidation. In this interval of temperatures, the O_2 diffusion coefficient follows a quasi-Arrhenian behavior with a corresponding effective activation energy of 1.12 eV (Fig. 4.11, right panel). The calculated activation energy is in excellent agreement with experimental values obtained at similar temperatures (1.04-1.26 eV) [18, 170, 171, 172].

During the Monte-Carlo evolution, the diffusing particles visit a distribution of minima and saddle points on the disordered energy landscape according to particular distributions (Fig. 4.12, left panel) [173]. Visited minima are concentrated at the lowest energy values for O_2 in amorphous SiO_2. The energy distribution of the visited saddle points is broader. When the energies are referenced with respect to the most stable minimum in SiO_2, the highest energy values are around the effective activation energy for O_2 diffusion [173]. These results highlight the percolative nature of the O_2 diffusion process in the disordered oxide. The long-range diffusion mainly involves the lowest-energy part of the full disordered energy landscape which allows for percolation throughout the oxide.

The above arguments lead us to assess the influence of both the energetical and topological properties of the energy landscape on the diffusion of interstitial O_2 in amorphous SiO_2. We first generate energy landscapes for the diffusing O_2 molecules with *realistic* energies but arbitrary connectivity properties. In particular, we vary the probability p of inserting bonds in the cubic lattice model between the percolation threshold p_c and 1. Monte-Carlo simulations on these systems confirm that, as the connectivity of the disordered network decreases, the long-range migration pathways involve higher energy values, thereby giving higher effective activation energies for diffusion (see Fig. 4.12, right panel) [173]. This process becomes critical at the percolation threshold where long-range diffusion pathways disappear and the activation energy tends toward infinity. Similar effects are found by perturbing the energetical properties of the disordered landscape. In particular, considering lattice models with all the local minima at the same energy and symmetric energy barriers taken from the distribution of average barriers for O_2 in amorphous SiO_2 (Fig. 4.8), the calculated activation energy for O_2 diffusion reduces to 0.8 eV (Fig. 4.12, right panel), significantly below the experimental estimates (1.04-1.26 eV) [18, 170, 171, 172].

4.6 Dependence of the O_2 diffusion rate on oxide thickness

The growth kinetics of very thin oxide films on silicon appears anomalously accelerated as compared to the prediction of the Deal-Grove model [20, 9] (cf. Chapter 1.2.2). Many interpretations have been put forward to describe this behavior [20, 9, 17]. The most accredited among them assumes that the diffusion rate of the oxidizing species shows a spatial dependence across the oxide layer [20, 9]. As a matter of fact, this assumption is currently adopted in modern models which successfully account for the silicon oxidation kinetics in both the thin and the thick oxide regimes [174, 28]. However, an atomic scale description of the diffusion rate corroborating this behavior is lacking.

The O_2 diffusion rate through thin oxide films ($<$ 20 nm) is expected to increase significantly because of the percolative nature of the diffusion mechanism [174, 28, 173]. In fact, on a short-range scale, amorphous SiO_2 is not homogeneous and the diffusion rate increases due to the occurrence of small-barrier pathways. This effect should be contrasted with the presence of an oxide layer with a higher density in the neighborhood of the silicon substrate, as revealed by x-ray reflectivity experiments [53, 54]. Indeed, this layer is expected to reduce the diffusivity [175]. In this section, we specifically focus on the combined result of these two effects on the O_2 diffusion rate across the thin oxide. We note that, although other mechanisms might be operative in the thin oxide

	a-SiO$_2$	d-SiO$_2$
ρ (g/cm^3)	2.2	2.4
Si-Si (Å)	3.12±0.08	3.08±0.12
Si-O (Å)	1.61±0.02	1.61±0.02
O-O (Å)	2.63±0.09	2.63±0.09
∠ Si-O-Si	152°±12°	149°±13°
∠ O-Si-O	109.4°±5.8°	109.4°±5.8°

Table 4.4: Comparison between average structural parameters of amorphous SiO_2 (a-SiO_2) and densified amorphous SiO_2 (d-SiO_2), as obtained by classical molecular dynamics. The standard deviations are given after the ± sign.

regime [39, 132], we assume here that the interstitial O_2 molecule dominates the oxygen diffusion process across the film, regardless of its thickness.

4.6.1 O_2 diffusion in densified amorphous SiO_2

We describe densified amorphous SiO_2 by a set of atomistic model structures, generated by classical molecular dynamics [70, 136]. We use periodically repeated cubic cells of fixed volume, corresponding to a density of 2.4 g/cm^3, as estimated by x-ray reflectivity measurements for the oxide in the vicinity of the Si-SiO_2 interface [53, 54]. To generate model structures, we adopt the procedure described in Sec. 4.2. We construct 16 model structures with a number of atoms in the periodic cell ranging between 72 and 90. All the model structures consist of random networks of corner-sharing tetrahedral SiO_4 units, without any coordination defect. As compared with amorphous SiO_2 at the experimental density, structural parameters are only slightly affected by the increased density (Table 4.4). The reduced volume per SiO_2 unit appears to be accommodated by the reduction of the mean Si-O-Si bond angle and consequently of the Si-Si next nearest neighbor distance. The calculated structure factor compares well with experimental data and correctly shows a shift of the first sharp diffraction peak toward a value of about 1.7 Å^{-1} [176]. This agreement indicates that the intermediate range order in our model structures is properly described. The increased density only slightly affects the ring statistics (Fig. 4.13).

As for O_2 in amorphous SiO_2 (*cf.* Sec. 4.4), we here explore the potential energy landscape for interstitial O_2 in densified amorphous SiO_2 using an extended set of model structures for this material and adopting the classical scheme presented in Sec. 4.4.1. We first search for equilibrium sites of interstitial O_2 molecules in densified amorphous

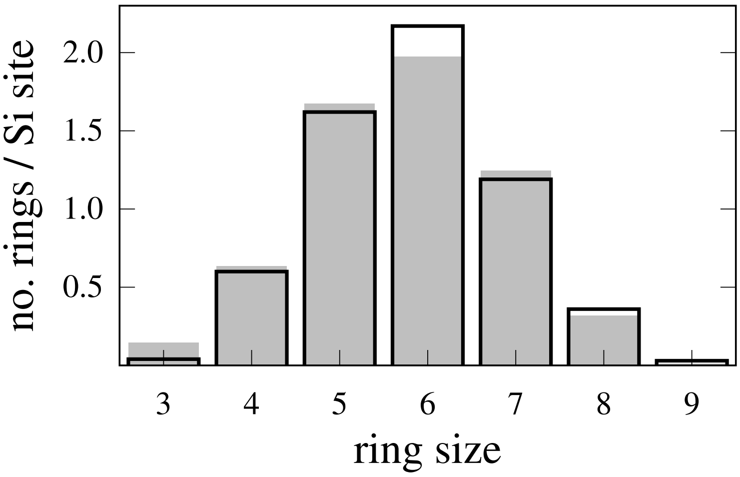

Figure 4.13: Average ring statistics in model structures of densified amorphous SiO_2 (thick solid line) and of amorphous SiO_2 at the experimental density (shaded histogram).

SiO_2. We find a concentration of local minima of $6.7 \cdot 10^{21}$ cm^{-3} and an average distance of about 5.3 Å between nearest neighbor minima. These values differ only slightly from the case of amorphous SiO_2 at regular density ($5.4 \cdot 10^{21}$ cm^{-3}, 5.7 Å) [173]. On the other hand, the energy distribution of local minima undergoes important changes. In particular, the mean value of this distribution shifts to a higher energy by 0.6 eV with respect to the mean value for amorphous SiO_2 at regular density (Fig. 4.14, left panel). This property is consistent with the decrease of the average interstitial volume in densified amorphous SiO_2. In fact, the O_2-network energy increases for decreasing interstitial volumes (*cf.* Sec. 4.5).

We then locate the saddle points of the potential energy landscape and their corresponding energies. The transition states connect neighboring minima by an asymmetric barrier. The energy barrier distribution associated to the low barrier side is well described by a decaying exponential function with a decay constant of 1.72 eV (Fig. 4.14, left panel). This should be compared with the corresponding value of 0.88 eV for amorphous SiO_2 at regular density [173]. These results indicate that the potential energy landscape for O_2 diffusion in densified amorphous SiO_2 is considerably shifted toward higher energies as compared to amorphous SiO_2 at regular density.

The location of the transition states defines an interstitial network for O_2 diffusion. The local minima form the nodes of this network. Our analysis shows that in densified amorphous SiO_2 the number of connections per node can vary between one and 10. The average number of connections per node is found to be 4.1. The associated distribution can be well reproduced by a binomial distribution, characterized by parameters $n = 12$ and $p = 0.34$. This fact further supports the absence of correlations in the potential energy landscape for O_2 diffusion in densified amorphous SiO_2.

To study the O_2 diffusion in densified amorphous SiO_2, we use a periodic fcc lattice

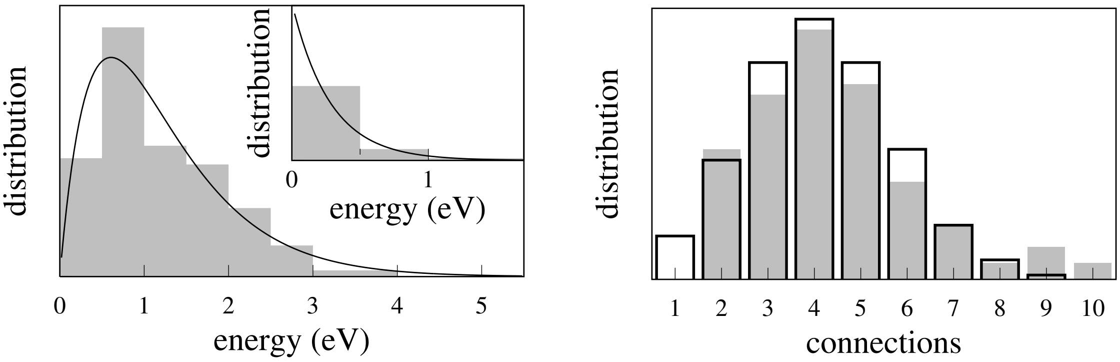

Figure 4.14: Left panel: energy distribution of minima and lowest barriers (inset) for O_2 in densified amorphous SiO_2. Histograms refer to distributions obtained exploring model structures of the oxide with the classical scheme, while solid lines correspond to fitted continuous distributions. As results from the statistical analysis of our atomistic model structures, the energy distributions of local minima and low-barrier-side transitions are uncorrelated. Right panel: distribution of connections between nearest neighbor local minima. A twelfth-degree binomial distribution with a coefficient of 0.34 (open histogram) well reproduces data extracted from the model structures of the densified oxide (filled histogram).

model with 50×50×50 independent sites. For a mean distance between local minima of 5.3 Å, this corresponds to a cubic volume of side ~19 nm. Adopting the independence condition, we transfer the nearest neighbor connectivity and the energy distributions derived from the atomistic structural models onto the lattice model. Monte-Carlo simulations for 2000 diffusing particles were performed at temperatures ranging between 1000 K and 1500 K. Minima and saddle points visited during the diffusion fall below the energies of competitive oxygen species [173], thereby indicating that the interstitial O_2 molecule remains the favorite transported oxygen species also in amorphous SiO_2 with a density 2.4 g/cm^3. The calculated diffusion coefficients are interpolated by an Arrhenius law with an effective activation energy of 2.0 eV, consistent with the experimental estimate of 2.0−2.4 eV for O_2 diffusion in an amorphous SiO_2 sample with a density of about 2.5 g/cm^3 [175].

4.6.2 O_2 diffusion through the oxide layer at the Si-SiO_2 interface

To model the O_2 diffusion through oxide layers of different thickness, we perform Monte-Carlo simulations on periodic lattice models with variable size in the direction z. In particular, we consider fcc lattice models of $50 \times 50 \times N$ sites, where N was varied from 2 to 20, corresponding to oxide thicknesses between 1 and 10 nm. The reduced periodicity in the z direction effectively models the diffusion in a thin oxide layer, as occurs at the Si-SiO_2 interface. In the other directions (x and y), the system is sufficiently large to recover the bulk limit. The diffusion coefficient is calculated at 1300 K, a temperature typically adopted for thermal oxidation of silicon.

At first, we consider the case of homogeneous oxide layers. We assign energies and connections to the lattice model according to distributions extracted for amorphous SiO_2 at regular density [173]. In particular, the correct nearest neighbor connectivity on the fcc lattice is obtained for a binomial function with $p = 0.27$. The results of the Monte-Carlo simulations show that the rate for diffusion along z increases for decreasing oxide thickness (Fig. 4.15). This behavior can be understood in terms of the percolative nature of the diffusion process. In fact, when the layer thickness drops, the number of low-barriers paths increases resulting in an increase of the diffusion coefficient. For thick layers, the bulk value is recovered. We note that an increase of the diffusion coefficient for thin oxide layers *cannot* explain the anomalous deviations from the Deal-Grove model in the initial stages of oxidation [32, 9].

It is interesting to note that the behavior of the diffusion coefficient in the xy plane is very different, showing a decrease for decreasing oxide thickness. This behavior corresponds to the gradual change of the diffusion coefficient when going from three to two dimensions. For example, the critical concentration of bonds for percolation increases from 0.24 to 0.50 when going from a three-dimensional cubic lattice to a two-dimensional square one [177].

X-ray reflectivity experiments indicate the occurrence of a 10-Å-thick oxide layer of higher density (2.4 g/cm^3) in the proximity of the Si-SiO_2 interface [53, 54]. We model the presence of this dense layer by including in our lattice models two planes, on which we map connectivity and energetic properties corresponding to amorphous SiO_2 with a density of 2.4 g/cm^3 (Fig. 4.14). For the remaining $N - 2$ planes, we used the properties appropriate for amorphous SiO_2 at regular density [173]. The two layers are separated by two planes of interlayer connections. For one plane of such connections, we use properties of amorphous SiO_2 and for the other those of densified SiO_2.

The diffusion coefficient for such oxide layers is given as a function of oxide thickness in Fig. 4.15. As expected, the diffusion coefficient is now lower than for homogeneous oxide layers. More interestingly, the diffusion coefficient falls below the bulk limit for oxide thickness larger than about 2 nm. This result indicates that the presence of a densified oxide can indeed account for a lower diffusion coefficient during oxidation. The diffusion coefficient is found to vary as a function of oxide thickness, approaching from below the bulk limit corresponding to amorphous SiO_2 at regular density. As

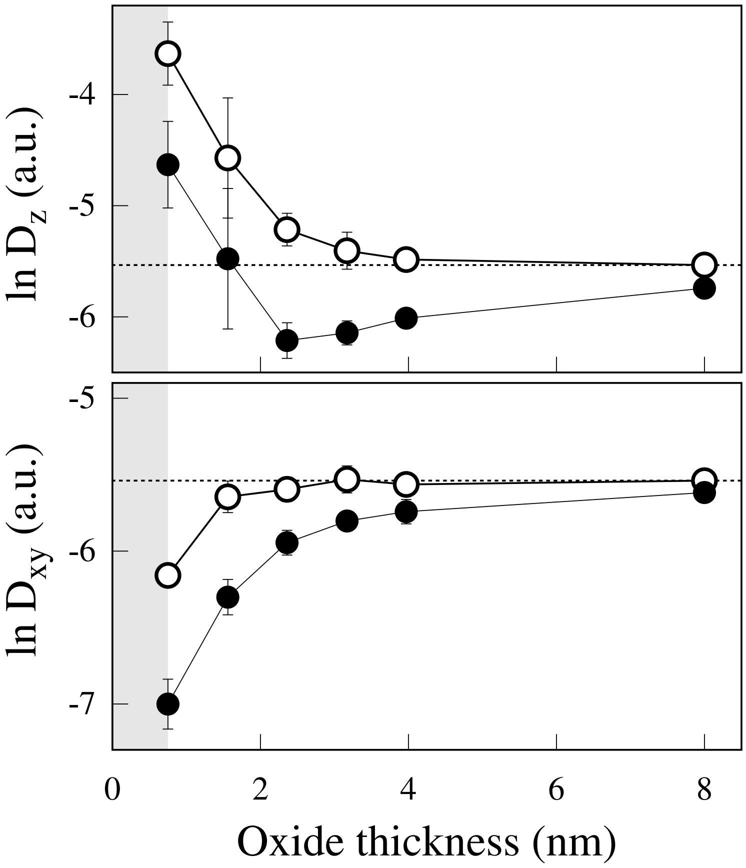

Figure 4.15: Calculated diffusion coefficients for homogeneous (open symbols) and non-homogeneous (closed symbols) oxide layers of varying thickness at Si-SiO$_2$ interfaces. The upper (lower) panel shows the diffusion coefficient in a direction perpendicular (parallel) to the plane of the interface. The dotted line corresponds to the limit of bulk amorphous SiO$_2$ at regular density. In the case of non-homogeneous oxide layers, the shaded region indicates the thickness of the oxide at the interface with a density of 2.4 g/cm^3.

long as the diffusion coefficient significantly differs from the bulk limit, deviations with respect to the Deal-Grove oxidation kinetics can be expected. This behavior of the diffusion coefficient as a function of oxide thickness is in qualitative agreement with experimental data for the oxidation kinetics [17].

For oxide thickness below 2 nm, size effects due to percolation still dominate the diffusion coefficient in our model oxide layers. However, in these early stages of oxidation, other atomic scale processes occur and might invalidate the underlying assumptions of our approach. Such processes include diffusion of peroxy linkages and charged species, exchange processes between gas-phase and network oxygen atoms [39, 132].

For diffusion parallel to the plane of the interface, we find the same qualitative behavior as for the homogeneous oxide. The presence of the dense oxide layer enhances the drop of the diffusion coefficient as the thickness decreases.

Chapter 5

Atomistic processes during growth of thin SiO_2 films on Si(100) substrates

5.1 Introduction

Gate oxides in current complementary metal oxide semiconductor (CMOS) technology are as thin as 15 Å and are expected to be scaled down eventually to a thickness regime of 10-12 Å [178]. The understanding of the mechanisms responsible for the growth of ultrathin SiO_2 films is of significant importance in state-of-the-art silicon microelectronics manufacturing. Despite the amount of work devoted to the investigation of the thermal Si(100)-SiO_2 system, the available atomic-scale information concerning the growth of thin oxide films on silicon is very limited [11].

The Deal and Grove model fails in describing the growth of thin oxide films [16, 20, 17]. In this regime, the oxidation rate appears anomalously accelerated with respect to the prediction of the Deal and Grove model [6, 16, 20, 17] (Sec. 1.2.2). By focusing on the kinetics of the oxide growth, different interpretations have been advanced to explain the failure of the Deal and Grove model [22, 9, 26, 27, 20, 17, 28, 29, 179, 180, 30, 31, 32]. The variety of explanations arises from the absence of direct information on the mechanisms which occur at the Si(100)-SiO_2 interface and are responsible for oxidation.

Isotope depth analysis of sequentially $^{18}O_2$ and $^{16}O_2$ oxidized oxide films provide useful indications on the mechanisms occurring during the thermal oxidation of silicon [33, 34, 36, 37, 39, 40]. For ultrathin films, recent high-resolution ion scattering experiments show overlapping depth profiles of both isotopes during the first 20–25 Å of oxide growth [37]. The occurrence of a mixed region depends on thickness and, for thick oxide films, two separate regions with distinct isotopic contents are observed (Sec. 1.3) [36, 37]. In addition, very recent isotopic Si substitution experiments suggest that, within a depth resolution of the order of 7 Å, Si atoms remain immobile during growth of ultrathin SiO_2 films on Si substrates [41]. These two sets of experimental findings suggest that oxygen is the dominant oxidizing species and that, for very thin films, oxygen exchange processes occur throughout the film.

Only a few theoretical investigations have addressed the atomic processes occurring during the growth of thin oxide films [132]. So far, theoretical studies have mostly focused either on the atomistic mechanisms responsible for network transformation at the Si(100)-SiO_2 interface [42, 181, 69, 43] or on the very early stages of silicon oxidation [182, 183, 184, 149, 185, 186, 187]. Only recently, silicon oxidation has been addressed by studying the reaction of an O_2 molecule with a single Si-Si bond in α-quartz [188]. In this first-principles study, the reaction products have been reported to be dependent on the spin state of the molecule.

We here set out to investigating the atomistic processes which occur at the Si(100)-SiO_2 interface and are responsible for oxide growth. To this end, we adopt an accurate scheme based on the density functional theory. This chapter is organized as follows. First, we focus on the energetics and on the diffusion properties of negatively charged oxygen species in amorphous SiO_2. Then, we use the realistic model structures of the Si(100)-SiO_2 interface presented in the previous chapters to investigate the O_2 dissociation and incorporation processes occurring during the growth of thin oxide films. The role of both the charge and the spin of the O_2 molecule are investigated.

5.2 Negatively charged oxygen species in a-SiO_2

SiO_2 is an insulating material. The conduction-band and valence-band offsets at the Si(100)-SiO_2 interface are 3.15 eV and 4.6 eV, respectively [189]. These high barriers prevent the O_2 molecules from charging when they diffuse in the oxide at large distances from the Si substrate. These arguments are supported by experiments which show that oxidation rates of very thick oxide films are unaffected by an external electric field [21, 141, 142, 143, 144]. However, close to the Si(100)-SiO_2 interface, charge tunneling becomes much more favorable and charged oxygen species may therefore play a more fundamental role in the oxidation process. To understand the role played by these charged species during the growth of thin films, we first consider their physical properties in the oxide.

5.2.1 Energetics of negatively charged O species in a-SiO_2

The calculation scheme employed here is based on the density-functional theory [145, 146]. The adopted technical ingredients are the same as those reported in Sec. 4.3.1. In this scheme, basis sets of plane-waves satisfying periodic boundary conditions are used to describe valence wave functions and charge densities. To prevent the energy from diverging in this framework, the presence of a charged defect in a periodic system is accompanied by the inclusion of a neutralizing uniform background density of opposite sign [190]. As a first approximation [190], the energy of the isolated charged defect in the periodically repeated system can be thus recovered by subtracting the spurious interaction of the charges with the uniform background. Assuming that the added charge is well localized in the simulation cell, the electrostatic energy of the lattice of point charges embedded in the neutralizing jellium corresponds to:

$$E_{\mathrm{corr}}(n) = -\frac{n^2\alpha}{2L\epsilon} \tag{5.1}$$

where α is the lattice-dependent Madelung constant, n is the number of additional or subtracted electrons, ϵ the dielectric constant of the underlying periodic medium, and L the linear size of the cell [190]. Using a cubic cell of side equal to 10.44 Å (corresponding to the cell used for the model structures of amorphous SiO_2 containing 24 SiO_2 units) and accounting for the correction in Eq. (5.1) we estimate an electron affinity of of 1.67 eV and 0.61 eV for the isolated oxygen atom and molecule, respectively. These values are in good agreement with the respective experimental estimates of 1.46 eV and 0.45 eV [150].

We investigate the energetics of negative atomic and molecular oxygen species in amorphous SiO_2, either singly or doubly charged. For the disordered oxide, we use a model structure of silica containing 24 SiO_2 units (Sec. 4.2). Each species is then inserted in several different locations inside the model structure of the oxide. Upon relaxation within our first-principles scheme, the formation energy E_{f} of the charged oxygen species is estimated according to:

$$E_{\mathrm{f}} = E - E_{\mathrm{corr}}(n) - E_0 - e_0 - n\mu \tag{5.2}$$

where E is the energy of the defected system, E_{corr} the correction term in Eq. (5.1), E_0 the energy of the unperturbed SiO_2 network, e_0 the energy of the neutral isolated defect, n the number of electrons added to the system, and μ the electron Fermi energy. The energy of an isolated O_2 molecule is used as reference for both atomic and molecular species. Therefore, the formation energy of an atomic species corresponds to the energy of two identical defect at infinite distance in the oxide. We note that energies for charged defects depend on the position of the electron Fermi energy μ within the gap. To compare charged and neutral defects, μ is usually referred to the position of the valence band edge e_v in the unperturbed periodic system. Hence:

$$\mu = e_v + \chi, \tag{5.3}$$

with χ varying between the valence and conduction band edges of the unperturbed periodic system. We note that, in the framework of first-principles supercell calculations, the energy comparison between neutral and charged defects is accurate only when the perturbation caused by the defect to the host periodic system is localized compared to the size of the simulation cell.

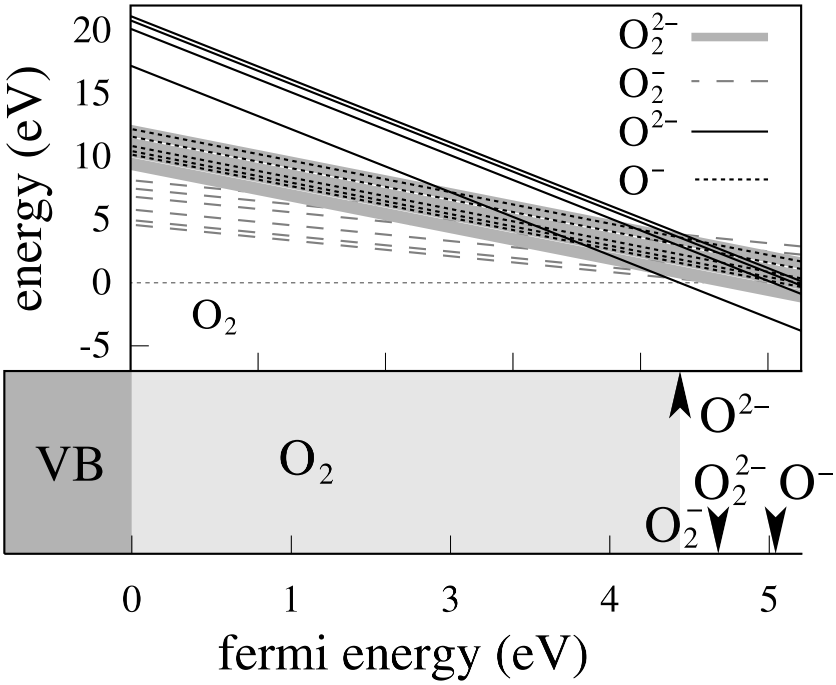

Figure 5.1: Formation energies for negatively charged oxygen species in amorphous SiO_2 as a function of the Fermi energy in the gap. The calculated energy gap is 5.3 eV. At the top right corner, the considered species with their corresponding symbols. Energies are referred to that of the O_2 molecule in the vacuum. The neutral O_2 molecule in large interstitials in a-SiO_2 has similar energies. At the bottom, arrows indicate for each species the position of the Fermi level in the gap above which they become more stable than the neutral O_2 molecule. The shaded region highlights the range of Fermi energies for which the neutral O_2 molecule is the most stable species in amorphous SiO_2.

In Fig. 5.1, the formation energies for the negatively charged oxygen species are reported as a function of the Fermi energy in the gap (χ) and are compared to the lowest energy for the neutral O_2 molecule in amorphous SiO_2 (Sec. 4.3.3). Neutral O_2 remains the most stable species until the Fermi energy reaches a value of about 4.3 eV. Above this value, the negatively charged oxygen species become more stable. Due to the disordered nature of the oxide, the formation energies of the negative species are spread over a wide interval. These intervals overlap for Fermi energies χ between 4.3 eV and 5.3 eV (Fig. 5.1). Hence, on the basis of the present framework, it remains unclear which charged species is most stable in amorphous SiO_2 for $\chi > 4.3$ eV. Nevertheless, due to the larger slope of E_f with χ, the O^{2-} species appears to be energetically favored for Fermi energies close to the conduction band. The diffusion properties of O^{2-} in α-quartz have been carefully investigated in a recent study [134].

At variance with the neutral O_2 molecule which occupies interstitial positions in the oxide, negatively charged species prefer to incorporate in the SiO_2 network (Fig. 5.2). Because of the disordered nature of a-SiO_2, we find several different local minima for each species. We can recognize some general features in the binding properties of the negatively charged O species. O^- incorporates in the oxide network in correspondence of Si atoms which become 5-fold coordinated with O. The additional O^- atom constitutes a dangling appendix of the oxide network protruding toward the nearest interstitial void. The O^{2-} species behaves similarly but its lowest energy configuration is formed when the O appendix bends toward a nearest neighbor O atom of the network to form a supplementary bond with a nearest neighbor Si atom. The final configuration corresponds to an oxygen double-bridge structure [134] (Fig. 5.2). Negatively charged molecular oxygen species tend to incorporate the network by forming bonds with Si atoms. O_2^- and O_2^{2-} like to form one and two Si-O bonds, respectively (Fig. 5.2).

A bond energy picture is generally applicable to SiO_2 networks [79, 74, 59]. Within this description, the energy of the network can be expressed as a sum of bond and strain energies [79, 74, 59]. On the basis of this picture and assuming that the additional charge is well localized on the defect oxygen species, we can split the formation energy in Eq. (5.2) in different contributions. In particular, we aim at obtaining a qualitative estimate for both the binding energy and the corresponding induced strain energy of the charged species. These quantities carry relevant information on the properties of the energy landscape for the charged oxygen species in amorphous SiO_2. We here only focus on molecular species. For negatively charged atomic species this separation is much more delicate. Indeed, upon incorporation in the network, we often find configurations in which the additional O atom is equivalent to next-nearest neighbor O atom of the oxide.

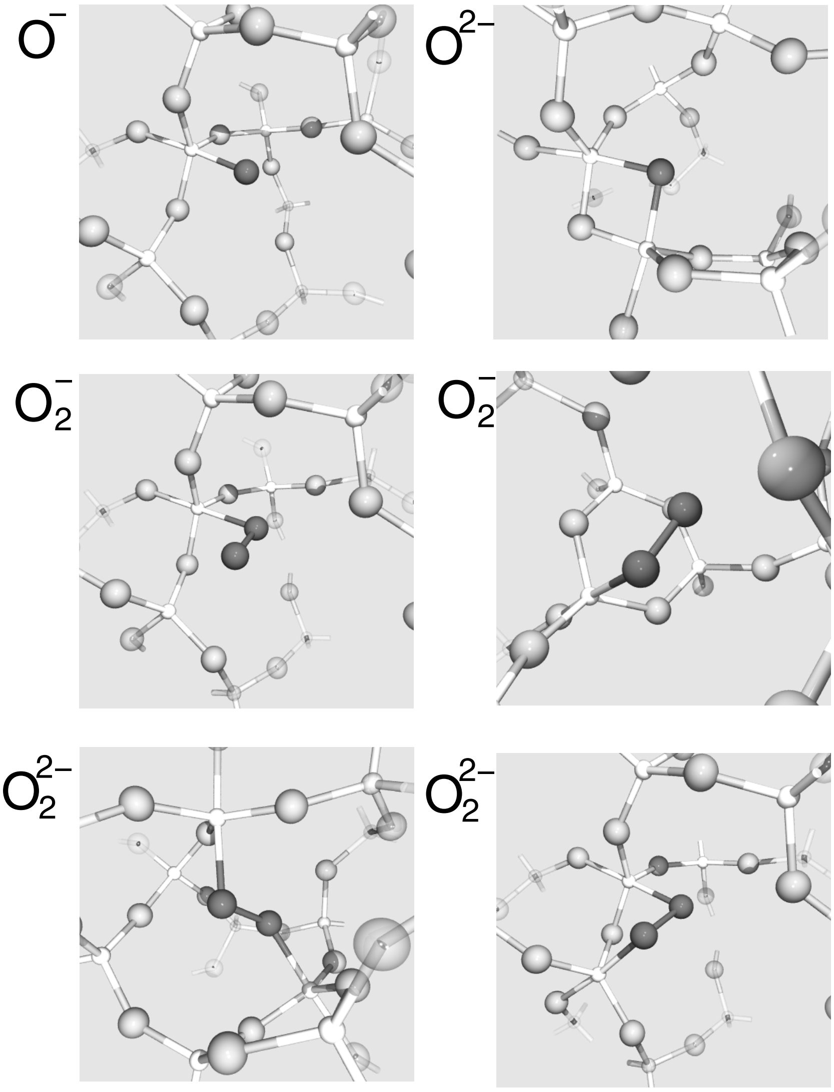

Figure 5.2: Ball and stick representation of the most stable configurations of negatively charged oxygen species in amorphous SiO_2. Relaxed structures are obtained by using the first-principles scheme described in Sec. 4.3.1. Light (shaded) spheres refer to Si (O) atoms of the oxide network. O atoms belonging to the charged defects are represented by darker spheres.

Referring the formation energy E_f for O_2^- and O_2^{2-} to μ and 2μ, respectively, we now write Eq. (5.2) in the following way:

$$E_\mathrm{f} = [E - E_\mathrm{corr}(n) - E_{\mathrm{SiO}_2} - e_0] + (E_{\mathrm{SiO}_2} - E_0) \tag{5.4}$$

where E_{SiO_2} accounts for the relaxation energy of the oxide network due to the incorporation of the charged molecular species. The energy E_{SiO_2} can easily be calculated by removing the charged molecular defect from the relaxed system without allowing for further structural relaxation. The term $E - E_{\mathrm{SiO}_2} - e_0$ corresponds to the gain in energy of the system upon capture of n electrons and consequent binding of the molecular species to the oxide network. In the following, we will refer to this term as to the electronic binding energy. Instead, the term $E_{\mathrm{SiO}_2} - E_0$ is the strain energy of the oxide network induced by the incorporation of the charged species. The deformation of the molecule is negligible.

The first-principles evaluation of E_{SiO_2} for various configurations of the charged molecular species in amorphous SiO$_2$ shows that the electronic binding energy ranges between -0.7 eV and -1.2 eV for O_2^-, and between -0.7 eV and -4.2 eV for O_2^{2-}. Instead, the strain energy of the oxide network takes values ranging between 1.5 eV and 4.7 eV for O_2^-, and varies between 3.8 eV and 6.3 eV for O_2^{2-}. These results suggest that negative charged molecular species strongly perturb the oxide network. The oxide deformation energy induced by their incorporation in the network contributes significantly to the formation energy. Moreover, the range of values for both the electronic binding and oxide strain energy suggests that their energy landscape is strongly affected by the disordered nature of the oxide.

5.2.2 Energy landscape for O_2^- and O_2^{2-} in a-SiO$_2$

O_2^- and O_2^{2-} significantly bind and deform the oxide network in correspondence of local minima configurations (Sec. 5.2.1). This behavior is opposite to that of the neutral O_2 molecule which finds local minima in interstitials barely perturbing the surrounding oxide network (Sec. 4.4).

We here carry further the analysis of the energy landscape by exploring transition states for O_2^- and O_2^{2-} migration in amorphous SiO$_2$. To this end, we apply a new method for moving the molecular species along migration pathways. We start from an equilibrium configuration of the charged species in the model structure of the oxide. Then, we introduce an external short-range repulsive potential acting on the center of mass of the molecule. The strength and the range of this potential increase slowly and gradually with time. At the same time, the center of mass of the oxide matrix is kept fixed and energy is constantly extracted from the full system by damping the electronic degrees of freedom [191]. In this way, the molecular species is moved through the oxide network. We note that the rate at which the energy is provided to the diffusing molecule is small compared to the damping rate of the electronic degrees of freedom. By satisfying this requirement, the oxide network relaxes consistently during the evolution of the O_2

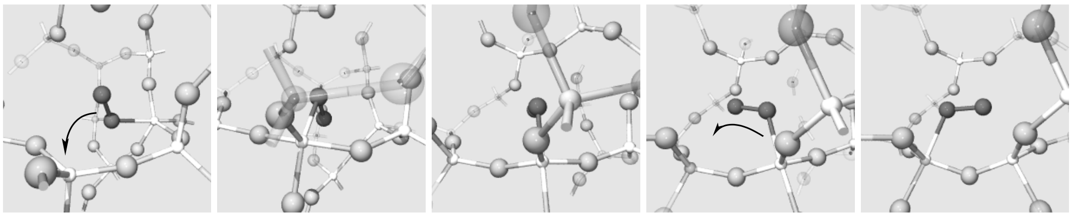

Figure 5.3: Sequence of frames picturing transition states for O_2^- migration in a-SiO_2. The arrows in the first and fourth frame indicate the next Si atom of the network with which the charged species forms a bond. Light (shaded) spheres are used for Si (O) atoms of the oxide network. O atoms belonging to the molecular species are represented by dark spheres. The same conventions are used throughout this chapter for representing the oxide network and the O species.

molecule without acquiring kinetic energy. Moreover, although this method suffers from hysteresis effects, the translational evolution is imposed to be sufficiently slow that the motion of the molecule occurs on a minimum energy transition pathway. To support this argumentation we note that, while more flexible, this method closely resembles the activation relaxation technique [158]. Indeed, we verify that in the case of the neutral O_2 in a-SiO_2 described within the classical scheme (Sec. 4.4.1), our method gives the same saddle points identified by adopting the activation relaxation technique (Sec. 4.4.2).

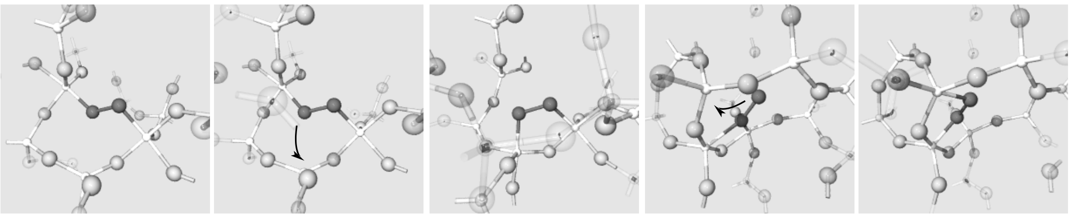

Figure 5.4: Sequence of frames picturing transition states for O_2^{2-} migration in a-SiO_2. The arrows in the second and fourth frame indicate the next Si atom of the network to which the charged species attaches.

We generate by first-principles a diffusion pathway for the O_2, O_2^-, and O_2^{2-} molecules in a model structure of amorphous SiO_2. Starting from an equilibrium configuration, we move the molecular species through the disordered oxide for a length of about 24 Å. As expected, the neutral O_2 molecule diffuses easily through the interstices of the network. Along the migration pathway, the highest transition barrier is encountered when crossing a fivefold ring (Fig. 5.5). Because of the percolative nature of the diffusion, these high barriers are usually avoided during diffusion at finite temperature (Sec. 4.5). In contrast with neutral O_2, charged molecular species show more complicated energy profiles along the migration pathways. O_2^- proceeds by sequentially switching the O atom of the molecule which binds with Si atoms of the network. The motion may be pictured as O_2^- walking over the Si atoms of the oxide network (Fig. 5.3). In the case of O_2^{2-}, both atoms of the molecule tend to form bonds with Si atoms of the network. Accordingly, migration appears to be strongly hindered (Fig. 5.4). Indeed, the energy profile along the migration pathway extends over about twice the range of energies determined for O_2^- (Fig. 5.6). These results are consistent with the range of values for the electronic binding and the oxide strain energy estimated in the previous section for O_2^- and O_2^{2-} local minima.

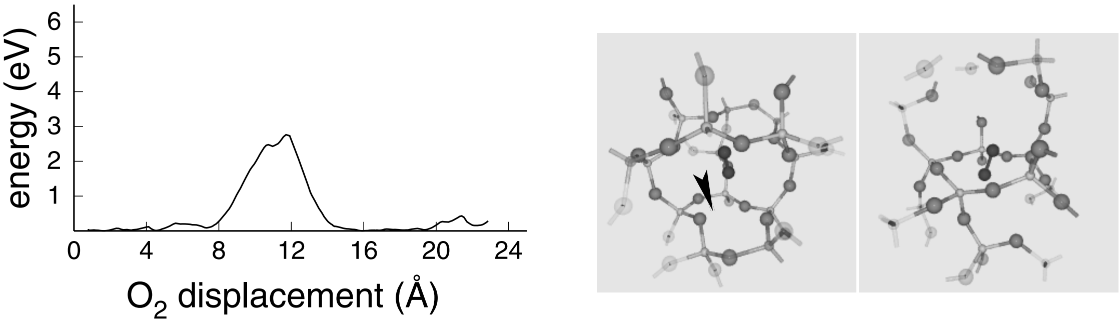

Figure 5.5: Left: energy profile along the diffusion pathway for neutral O_2 in a model structure of amorphous SiO_2. The pathway is generated using first-principles simulations and the procedure described in Sec. 5.2.2. Right: ball and stick representation of the O_2 molecule in proximity of the fivefold ring (middle panel) and at the transition state (right panel).

We note that, due to the its particularly strong attitude to bind and deform the oxide network, the O_2^{2-} species is able to generate defects. Indeed, in two occasions during the migration pathway, we find stable configurations for O_2^{2-} associated to the formation of a non-bridging oxygen defect (Fig. 5.6). In these configurations, the Si-O bonds formed by the O atoms of the O_2^{2-} species with the oxide network appear to be sufficiently strong for breaking one Si-O bond of the preexisting network. Indeed, the distance between the Si and O atoms of the broken Si-O bond increases up to a value of 3 Å in correspondence of the equilibrium configuration (Fig. 5.6).

5.2.3 O_2^- and O_2^{2-} dissociation in a-SiO$_2$

The negatively charged molecular species can dissociate into two atomic species. In a-SiO$_2$, O_2^- can give raise to an O ion (O^-) and a peroxyl linkage (Fig. 5.7) while the

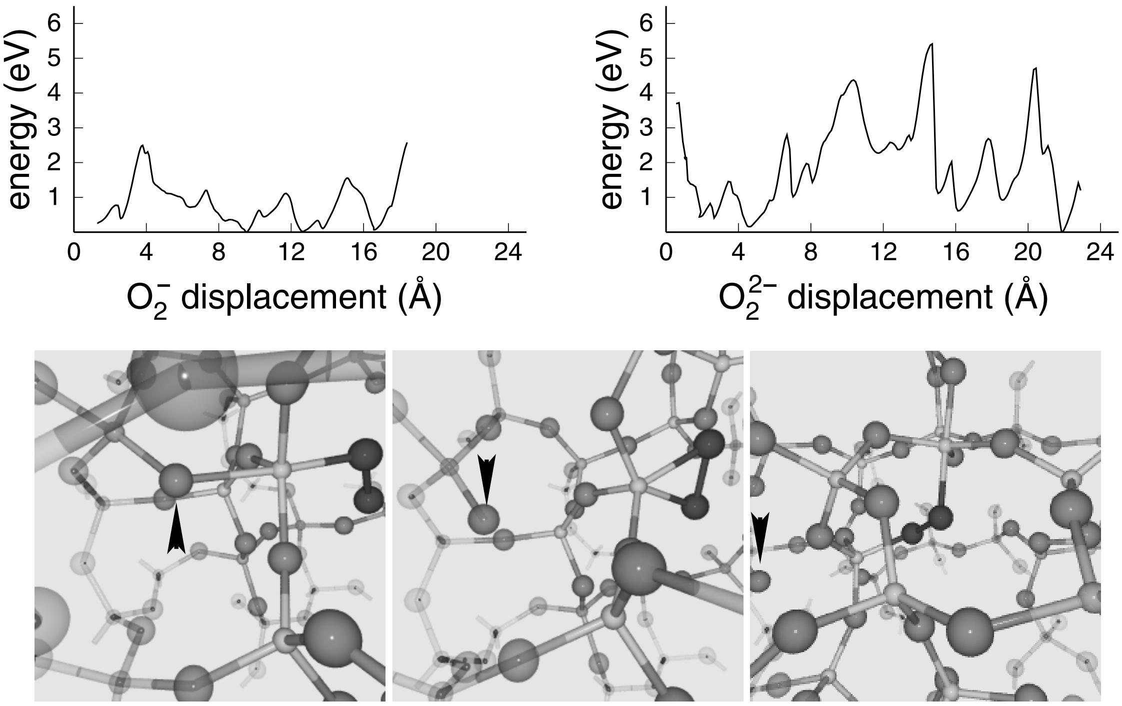

Figure 5.6: Top: energy profiles along the migration pathways for O_2^- and O_2^{2-} in a model structure of amorphous SiO_2. Bottom: formation of a non-bridging oxygen defect (indicated by the arrow) by the O_2^{2-} migration.

O_2^{2-} species can dissociate into either two separated O^- or into a O^{2-} and a peroxyl linkage (Fig. 5.8). We here address the energetics of these reactions using first principles calculations. In particular, to evaluate transition barriers we use the scheme presented in the previous section. In this case, the external potential stimulates dissociation. Hence, at each step of the procedure, the origin of the spherical repulsive potential is located at the center of mass of the molecular species. Moreover, it acts independently on each of the O atoms of the molecule.

We consider several equilibrium configurations for both the O_2^- and O_2^{2-} defects in a-SiO_2. For O_2^-, we find dissociation energies between 2.4 eV and 3.2 eV while they range between 1.2 eV and 1.8 eV for O_2^{2-}. The disordered nature of the oxide spreads the energies required for dissociation over an interval of about 0.7 eV. Nevertheless, it is possible to recognize that dissociation energies for O_2^{2-} are approximately half of those for O_2^-. This is consistent with the weakening of the O-O bond with the increase of negative charge carried by the molecule. In the case of an isolated molecule, we calculate dissociation energies of 5.6 eV, 4.8 eV and 1.78 eV for the O_2, O_2^-, and O_2^{2-}, respectively. Corresponding experimental values for O_2 and O_2^- are 5.1 eV and 4.1 eV, respectively [150].

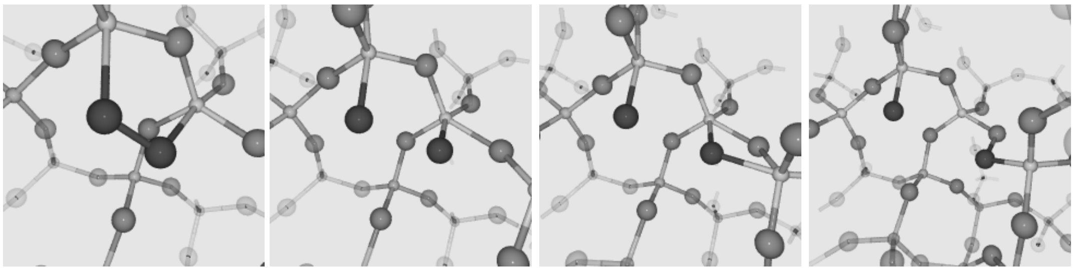

Figure 5.7: Ball and stick representation of the dissociation process of O_2^- into a O^- and a peroxyl linkage.

The dissociation process of O_2^- and O_2^{2-} leads to a couple of neighboring atomic oxygen defects in amorphous SiO_2 (Figs. 5.7 and 5.8). We find that the products of dissociation are higher in energy with respect to the initial charged molecular species. In particular, the formation of a O^- and a peroxyl group by O_2^- dissociation is endothermic by 1.8–2.8 eV. In the case of O_2^{2-} dissociation, the reaction products (Fig. 5.8) raise the energy by an amount between 1.0 eV and 1.7 eV. Again, we observe that structural disorder of the oxide is responsible for a finite range of values [131]. Moreover, we note that the more negative charge is carried by the molecular species, the less are the dissociation barrier and the energy of the reaction products. These results suggest that the dissociation of molecular species is favored by a sequential capture of electrons.

5.3 Oxygen incorporation processes at the Si(100)-SiO_2 interface

We here explore the atomistic mechanisms occurring at the Si(100)-SiO_2 interface responsible for oxidation. For this purpose, we use several realistic model structures for the interface which reproduce atomic-scale properties derived from X-ray reflectivity, photoemission, and ion-scattering experiments (Chap. 2 and 3). These models present different interfacial transition structures and thereby should be considered as representative of separated regions of the Si(100)-SiO_2 interface. Thus, by using first-principles calculations, we focus on both energetics and atomistic mechanisms associated with oxygen species reacting at the interface and incorporating in the network. In this investigation, we account for both spin [188] and charge effects [132].

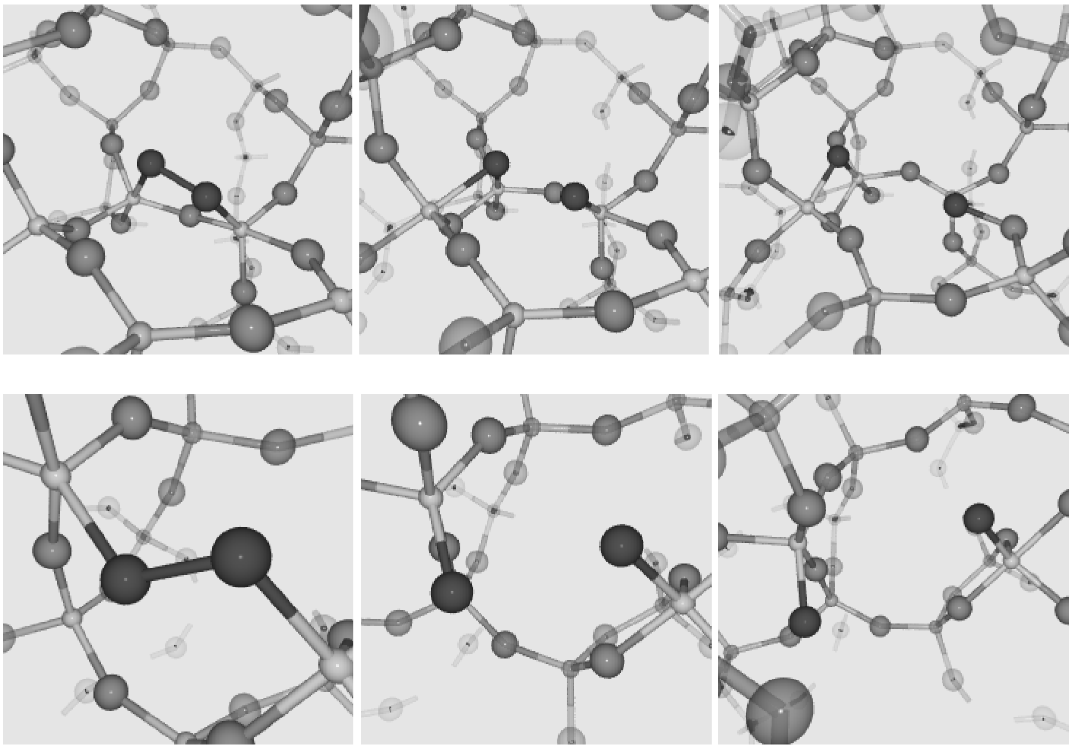

Figure 5.8: Ball and stick representation of the dissociation process of O_2^{2-} into a O^{2-} and a peroxyl linkage (top), and into two separated O^- (bottom).

5.3.1 Theoretical approach

We consider the model interfaces referred to as B, C and C′ in Chapter 3. These models reproduce atomic-scale properties derived from a variety of experiments [63, 64, 53, 54, 49, 50]. In particular, they are consistent with ion-scattering data. These models reproduce the structural properties of the transition region at the Si(100)-SiO_2 interface to the best of our current knowledge (Sec. 3.4.2).

To minimize the computational workload, the model interfaces are simplified by reducing both the thickness of the oxide layer and the number of Si monolayers in the substrate. In particular, the retained oxide layers are about 5-6 Å thick and include the full suboxide regions of the original models (Sec. 3.4.1). The Si(100) substrate is modeled by 7 monolayers. On both sides, the unsaturated bonds are terminated by H atoms. First-principles structural relaxations show that the structural properties of the interfacial region do not appear significantly perturbed by these modifications. Other technicalities related to the first-principles simulations correspond to those reported in

Sec. 2.3.

For each model interface, we locate a molecular oxygen species in several configurations on top of the oxide component, at the oxide-vacuum interface. The initial positions are chosen in correspondence of oxide interstices in proximity of the vacuum. Adopting the same initial conditions, first-principles simulations are performed for the neutral O_2 molecule, in both the triplet and singlet spin state, and for the O_2^- and O_2^{2-} species. Each molecular species is moved toward the Si(100)-SiO_2 interface adopting the method described in Sec. 5.2.2. In some occasions, we also apply the methods described in Sec. 5.2.3 for investigating the dissociation process. Here below, we report the results of this first-principles investigation. The results are essentially independent of the model structure adopted for the Si(100)-SiO_2 interface.

5.3.2 Neutral O_2 at the Si(100)-SiO_2 interface

We first consider the O_2 molecule in the singlet spin state ($S = 0$). Our first-principles calculations show that the O_2 readily incorporates in the oxide network at the Si(100)-SiO_2 interface. We find that, as the O_2 molecule reaches the suboxide region near the interface, it attacks Si atoms in intermediate oxidation states and incorporates in the oxide network (Fig. 5.9). We find configurations in which the molecule penetrates within Si-Si bonds to form peroxyl-like oxygen defects (≡Si-O-O-Si≡) (Fig. 5.9 and 5.11). The incorporation process in Si-Si bonds in direct contact with the Si substrate is spontaneous. These Si-Si bonds comprise either nonoxidized Si atoms or Si atoms in oxidation states +1 and +2. When the Si-Si bond contains Si^{+3} moieties an is located at distances of about two or three Si-O bond lengths from the upper layer of the Si substrate, we observe that the incorporation process requires energies less than about 0.4 eV (Table 5.1). We find that the incorporation of the O_2 molecule in the oxide network decreases the energy of about 2.8–4.8 eV. This finite range of energy values appears to be related only to the structural disorder of the network.

Within the oxide interstitials, the most stable spin state for the O_2 molecule corresponds to the triplet one ($S = 1$) [130]. Nevertheless, the barrierless incorporation process of O_2 in Si-Si bonds at the Si(100)-SiO_2 interface does not appear to be severely influenced by spin effects. Indeed, the O_2 molecule in the triplet state still attacks of Si atoms in intermediate oxidation state and incorporates in the oxide network (Fig. 5.10). However, the incorporation process preferentially occurs in proximity of the Si substrate. The configuration resulting from the O_2 incorporation in the network depends on the local structure. Indeed, we generally find that the O_2 molecule penetrates into a Si-Si bond (Fig. 5.11, top panels). However, in some occasion, the system ends

Model	Si^{+n}–Si^{+m}	B_{incorp}	E_{incorp}	B_{diss}	E_{diss}
B	Si^{+2}–Si^{+2}	0.10	4.80	0.20	5.00
C	Si^{0}–Si^{0}	0.00	2.80	0.07	5.00
C	Si^{+3}–Si^{+2}	0.40	3.00	0.40	4.00
C	Si^{0}–Si^{0}	0.00	4.30		
C′	Si^{+3}–Si^{+2}	0.40	3.00	0.40	4.00
C′	Si^{+3}–Si^{+2}	0.40	3.50	0.30	5.00

Table 5.1: Reactions of a neutral O_2 molecule in the singlet spin state at the Si(100)-SiO_2 interface. The model interfaces used for the simulations are identified in the first column. The O_2 molecule incorporates in a Si^{+n}–Si^{+m} bond of the oxide network, where n and m assume the following values: 0, +1, +2, +3. According to the conventional interpretation scheme [47, 48, 51, 52, 192], the Si^{+n} moiety refers to a Si atom with n nearest neighbor O atoms. The incorporation (dissociation) process requires the system to overcome an energy barrier B_{incorp} (B_{diss}) and results in an energy gain of E_{incorp} (E_{diss}). Energies are given in eV.

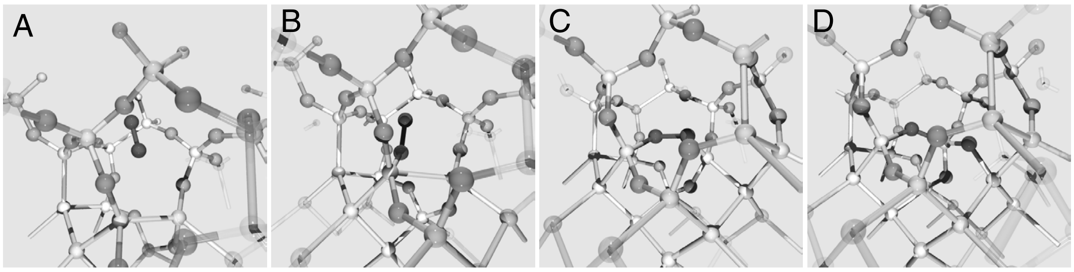

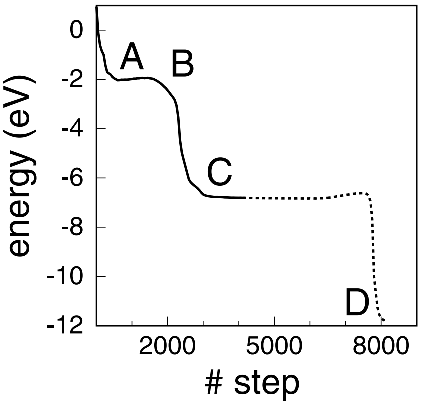

Figure 5.9: Top panels: sequential frames picturing the neutral O_2 molecule in the singlet spin state diffusing through the oxide layer (A), attacking a Si atom in an intermediate oxidation state (B), incorporating in the oxide network at a Si-Si bond (C), and dissociating (D). Side panel: energy profile vs. simulation step along the migration pathway across the oxide (solid) and during the subsequent dissociation process (dotted).

up in a defected configuration, showing a Si dangling bond in the upper layer of the Si substrate. The O_2 molecule then binds to the oxide through two Si atoms, one of which is fivefold coordinated by oxygen (Fig. 5.10). The incorporation process gives rise to a

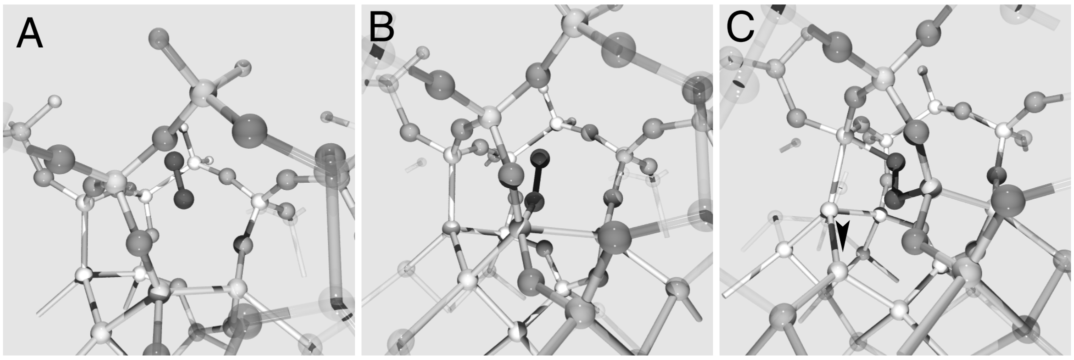

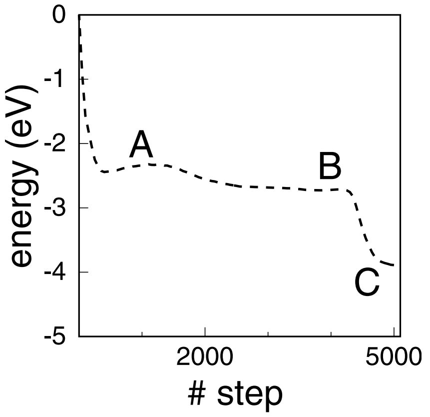

Figure 5.10: Top panels: sequential frames picturing the neutral O_2 molecule in the triplet spin state diffusing through the oxide layer (A), attacking a Si atom in an intermediate oxidation state (B), incorporating in the oxide network at a Si-Si bond (C). The incorporation process leads to a defected configuration, comprising a Si dangling bond (indicated by the arrow) and a 5-fold coordinated Si atom. Left panel: energy profile vs. simulation step along the migration pathway across the oxide (dashed).

decrease in energy of about 1.0-1.5 eV (Table 5.2). Subsequent spin conversion would decrease the energy of the system even more.

Model	Si^{+n}–Si^{+m}	B_{incorp}	E_{incorp}
C	Si^{+0}–Si^{+0}	0.10	1.00
C′	Si^{+2}–Si^{+2}	0.10	1.00
B		0.06	1.50

Table 5.2: Reactions of a neutral O_2 molecule in the triplet spin state at the Si(100)-SiO$_2$ interface. The model interface used for studying the incorporation process is identified in the first column. B_{incorp} is the energy barrier while E_{incorp} corresponds to the energy gain, both associated to the incorporation process in the oxide network. The energies are given in eV. The last row reports energies associated to an incorporation process which leads to the formation of a defected structure comprising a 5-fold and 3-fold coordinated Si atoms.

In a recent first-principles investigation, the oxidation of a Si-Si bond in α-quartz has been addressed [188]. The Si-Si bond in α-quartz has been created by removing

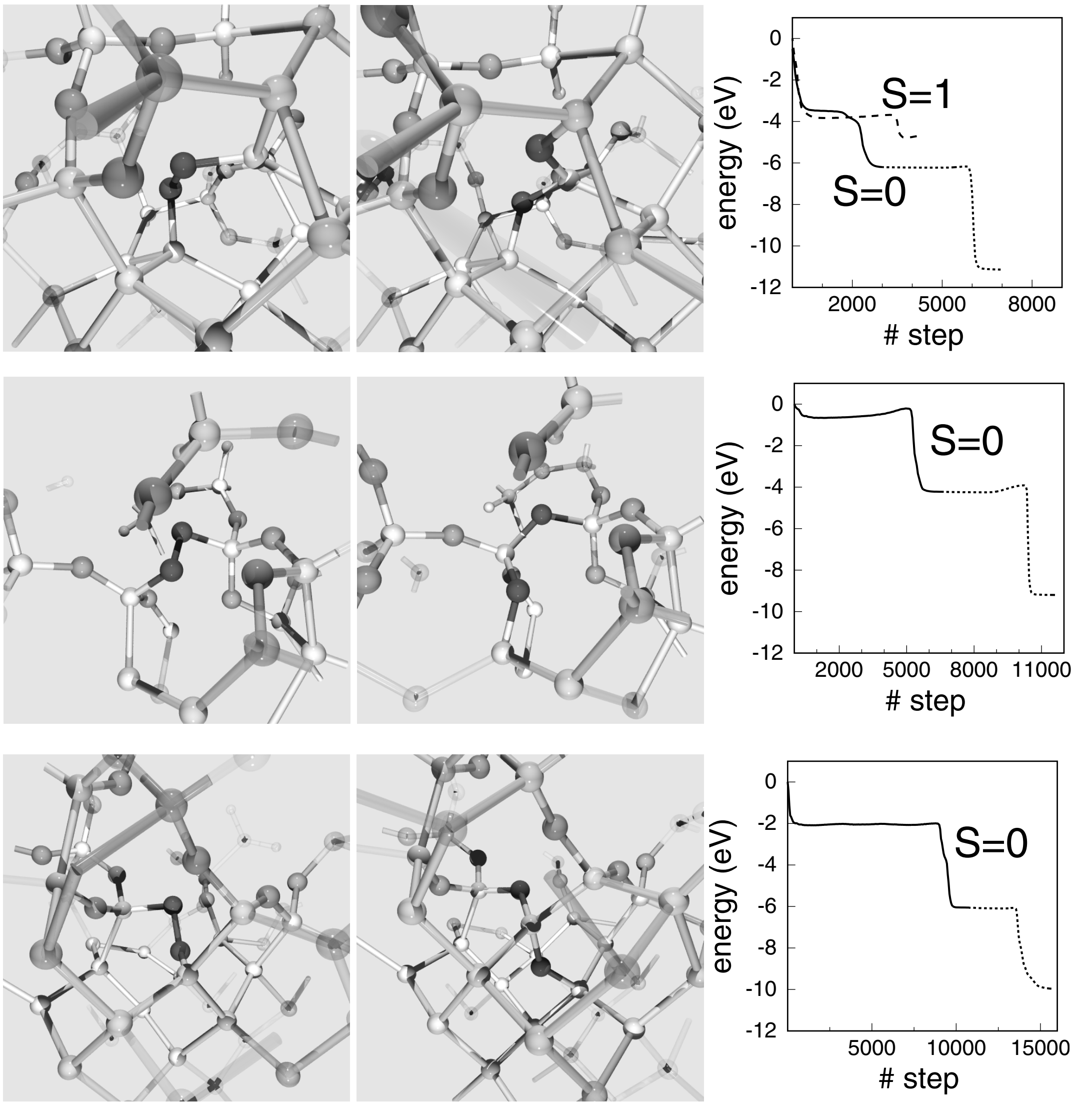

Figure 5.11: Left panels: the peroxyl-like structures resulting from the insertion of a neutral O_2 molecule into a Si-Si bond. Middle panels: configurations resulting from O_2 dissociation. Right panels: energy profile vs. simulation step during the migration process which leads to incorporation (solid). After incorporation of the O_2 molecule in the singlet state, the energy profile refers to the dissociation process (dotted). Top row: pathways generated for the O_2 molecule in the triplet and singlet spin state both lead to the configuration shown in the left panel. The energy profile obtained for the incorporation process of the O_2 molecule in the triplet state is reported in the right panel by a dashed line.

a O atom from a Si-O-Si structural unit. The O_2 reaction with the Si-Si bond in this environment has been shown to be dependent on the spin state of the molecule. In the singlet spin state, the O_2 molecule incorporates the Si-Si bond with an energy barrier of 0.2 eV. In the triplet spin state, the reaction occurs with a barrier of about 0.8 eV and leads to regular α-quartz structure with an additional interstitial atomic oxygen.

We observe that the energy difference between the triplet and singlet state for a peroxyl-linkage in α-quartz is about 5 eV. This difference in energy explains why the O_2 incorporation process in the Si-Si bond in α-quartz is not favorable when the triplet spin state is considered. In fact, the incorporation process for forming a peroxyl-linkage in α-quartz in the triplet state would have raised the energy of the full system by about 1.3 eV, with respect to the initial configuration (an interstitial O_2 molecule and a Si-Si bond in α-quartz). Therefore, the system prefers breaking the molecular bond and ending up in the reaction products found in Ref. [188].

Our results are consistent with those reported in Ref. [188]. Indeed, when the O_2 molecule is in the singlet state, we still find small energy barriers for the incorporation in Si-Si bonds. Moreover, when the O_2 molecule is in the triplet state, it avoids isolated Si-Si bonds embedded in the oxide and prefers reaching the Si substrate. However, in contrast to Ref. [188], we find that the presence of the Si substrate allows for spontaneous incorporation of the O_2 in the network, regardless of the spin state of the molecule. We argue that the charge transfer from the Si substrate to the molecular species favors the incorporation process. We note that spin effects play a role in narrowing the channels for incorporation in the network. In fact, when the molecule is in the triplet spin state, it preferentially reaches the Si substrate before incorporating in the network.

Upon O_2 incorporation in a Si-Si bond at the Si(100)-SiO_2 interface, further oxidation proceeds readily. Starting from several configurations obtained after O_2 incorporation, we apply the methodology presented in Sec. 5.2.3 and investigate the dissociation process. We find that dissociation is spontaneous for peroxyl-like oxygen defects in contact with the Si substrate (Fig. 5.11). Peroxyl-like oxygen defects at a distance of about three Si-O bond lengths from the upper layer of the Si substrate require an energy of about 0.3 for dissociation (Table 5.1) This barrier is small compared to the energy gain obtained from the O_2 incorporation in the Si-Si bond. Therefore, the energy required for dissociation can be provided by the incorporation process.

5.3.3 O_2^- and O_2^{2-} at the interface

When the O_2 molecule approaches the Si(100)-SiO_2 interface, electrons may be transferred from the Si substrate to the molecular species. We here investigate incorporation and dissociation processes of the O_2^- and O_2^{2-} species in proximity of the Si(100)-SiO_2 interface. We find that O_2^- and O_2^{2-} incorporate in the oxide by forming bonds with Si atoms of the network. This is consistent with the results obtained for O_2^- and O_2^{2-} in amorphous SiO_2. More noticeably, we observe that dissociation of these species is either spontaneous or requires energies less than 0.5 eV. These results suggest that, also in the case of the O_2^- and O_2^{2-} species, dissociation is favored by the vicinity of the Si substrate. We find that dissociation leads to both oxidation of Si-Si bonds and formation of charged atomic oxygen defects.

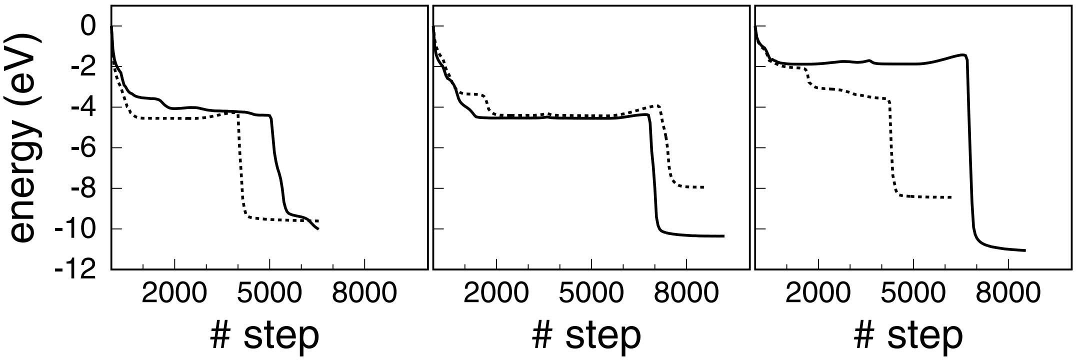

Figure 5.12: Energy profile vs. first-principles simulation step for the incorporation and dissociation process of the O_2^- (solid) and O_2^{2-} (dotted) species. The three panels refer to different initial locations of the charged species. In correspondence of a plateau, the charged molecular species are incorporated in the network and the dissociation process is started.

5.4 Summary

The understanding of the *atomic scale* mechanisms occurring during the growth of oxide films is here addressed in two sequential steps. First we focus on the properties of negative oxygen species in amorphous SiO_2. These species have been proposed to play a fundamental role during the growth of thin oxide films on a Si substrate [132]. Hence, we initially consider the relative energetics of neutral and negative oxygen species in both the atomic and the molecular state. The energy landscape and the dissociation properties of the O_2^- and O_2^{2-} are also considered. We find that in amorphous SiO_2 the negative oxygen species incorporate in the oxide network by forming additional Si-O bonds. The oxide network accommodates the negative oxygen species by undergoing significant distortions. Both electronic binding and network deformation energy values extend over a wide interval. In particular, for the O_2^{2-} species, the competition between these two energy contributions can lead to the formation of defects in the oxide. The investigation of the dissociation process of negatively charged molecular oxygen species in amorphous SiO_2 highlights the dependence of the dissociation energies on the disordered nature of the network and on the charge carried by the oxygen species.

In a second stage, we address the mechanisms responsible for oxidation at the Si(100)-SiO_2 interface. We consider the neutral O_2 molecule and the negatively charged molecular species, namely O_2^- and O_2^{2-}. In the case of the neutral O_2 molecule, effects associated to the spin state are also accounted for [188]. All these species are driven from the vacuum to the Si(100)-SiO_2 interface for studying sequentially the incorporation in the network and the dissociation process. We find that at the Si(100)-SiO_2 interface all these species incorporate in the network either spontaneously or by crossing small energy barriers. In particular, the neutral O_2 molecule attacks Si atoms in intermediate oxidation states in the vicinity of the interface and penetrates into Si-Si bonds forming peroxyl-like defects. This process is favored by the charge transfer from the Si-Si bonds to the molecular species. The triplet spin state of the O_2 molecule narrows the channels for network incorporation. Indeed, molecules in the triplet spin state incorporate in the network preferentially in correspondence of the upper layer of the Si substrate. Negatively charged species spontaneously incorporate in the oxide network at any distance from the substrate. Their incorporation is often associated to the formation of network defects, confirming their ability to modifying the oxide network, as already found for their interaction with amorphous SiO_2. After incorporation in the network, the dissociation and hence the oxidation of Si-Si bonds corresponds to barrierless processes. In particular, as in the case of the incorporation process, we find that dissociation requires either vanishing or very small energies. The energy required for crossing the small barriers is provided by the energy gained during the incorporation process. These results support an oxidation kinetics entirely governed by the diffusion process. Indeed, the incorporation and the dissociation processes occur in the vicinity of the Si(100)-SiO_2 interface and are nearly spontaneous. These results are consistent with experimental evidence for a layer-by-layer growth of the oxide [193]. In fact, according to our results, oxidation appears to be a spontaneous process at the Si substrate. Incorporation in the oxide in a region distant from the Si(100)-SiO_2 interface seems to require either charge transfer or, in correspondence of Si-Si bonds, spin conversion. For the same reasons, our results are consistent with the experimentally observed location of partially oxidized Si atoms [49, 50]. Moreover, the accumulation of negative charge at the interface during growth [178] might be an indication of the present of negatively charged species in the vicinity of the interface. Similarly, the occurrence of negatively charged species near the

Si(100)-SiO_2 interface is consistent with the occurrence of oxygen exchange processes during growth of thin oxide films [37].

Conclusion

First-principles and classical schemes are combined to carry out an *atomic-scale* investigation of the silicon oxidation process and the properties of the Si(100)-SiO_2 interface. We first address the atomic structure of the interface. We construct atomistic models of the Si(100)-SiO_2 interface in accord with available experimental data. In particular, we generate transition structures from crystalline silicon to disordered SiO_2 accounting for the density of coordination defects, the amount and location of partially oxidized Si atoms, and the mass density profile, as measured in electron-spin-resonance, photoemission, and X-ray reflectivity experiments, respectively. A variety of model interfaces are obtained, differing by the degree of complexity in the transition region. Then, we further characterize the transition structure at Si(100)-SiO_2 interface by addressing the inverse ion-scattering problem. For this purpose, we refer to a new set of ion-scattering measurements carried out in the channeling geometry in order to achieve sensitivity to Si displacements at the interface. To interpret these experimental results, we perform ion-scattering simulations on a selected set of model interfaces presenting different atomic-scale features in the transition region at the Si(100)-SiO_2 interface. Silicon displacements larger than 0.09 Å are found to propagate for three layers layers into the Si substrate. Transition structures consistent with these distortions include Si-Si in-plane dimers, O-protrusion, and/or a disordered bond pattern at the Si(100)-SiO_2 interface. A transition structure with regularly ordered O bridges is ruled out.

We then address the silicon oxidation process. We first focus on the diffusion limited regime occurring during the growth of thick oxide films. In particular, we provide an atomic-scale description for the long-range oxygen migration through the disordered SiO_2 oxide. The O_2 molecule is firmly identified as the transported oxygen species and is found to percolate through interstices without exchanging oxygen atoms with the network. The interstitial network for O_2 diffusion is statistically described in terms of its potential energy landscape and connectivity. The associated activation energy is found in agreement with experimental values. Then, we address the O_2 diffusion rate through the thin oxide layer at the Si-SiO_2 interfaces. In particular, we investigate the combined effect of a percolative diffusion mechanism and of a dense oxide layer located close to the silicon substrate. We first extend our atomic-scale description of O_2 diffusion in amorphous SiO_2 to the case of a densified oxide. This yields an activation energy which compares well with the experimental result. Next, we investigate the dependence of the O_2 diffusion rate on oxide thickness at Si-SiO_2 interfaces. We consider both homogeneous and non-homogeneous oxide layers. The non-homogeneous oxide is composed of two layers, a regular and a densified one. The thickness and the mass density of the densified layer are taken from experiment. In the case of a regular oxide, we find that the O_2 diffusion rate increases for decreasing thickness, as a result of the percolative nature of the diffusion mechanism. When a densified layer is inserted, the diffusion coefficient drops below its value for bulk amorphous SiO_2, for oxide thicknesses larger than 2 nm. These results are consistent with the experimental behavior of the oxidation kinetics and support the *blocking layer* [9] model for explaining the failures of the Deal and Grove model [16, 20, 17].

The description of the *atomic scale* mechanisms occurring during growth of ultrathin oxide films is addressed. This last investigation is carried out in two sequential steps. First, we focus on the properties of negative oxygen species in amorphous SiO_2. These species have been proposed to play a fundamental role during growth of thin oxide films on Si substrates [132]. Hence, we consider amorphous SiO_2 and focus on the relative energetics of neutral and negative oxygen species in both the atomic and the molecular state. The energy landscape and dissociation properties of the O_2^- and O_2^{2-} are also considered. We find that, in amorphous SiO_2, the negative oxygen species incorporate in the oxide network by forming additional Si-O bonds. Accordingly, the oxide network accommodates the negative oxygen species by undergoing significant distortions. Both binding and network deformation energies extend over a wide interval of values. In particular, for the O_2^{2-} species, the competition between these two energy contributions can lead to the formation of defects in the oxide. The investigation of the dissociation processes of negatively charged molecular oxygen species in amorphous SiO_2 highlights the dependence of the dissociation energies on the disordered nature of the network and on the charge carried by the oxygen molecule.

Finally, we address the mechanisms responsible for oxidation at the Si(100)-SiO_2 interface. We consider the neutral O_2 molecule and the negatively charged molecular species, namely O_2^{2-} and O_2^{2-}. In the case of the neutral O_2 molecule, different spin states have been considered. For all these species we study sequentially the incorporation in the network and the dissociation process. We find that at the Si(100)-SiO_2 interface all these species incorporate in the network either spontaneously or by crossing small energy barriers. In particular, the neutral O_2 molecule attacks Si atoms in intermediate oxidation state in the vicinity of the interface and penetrates into Si-Si bonds forming peroxyl-like defects. This process is favored by the charge transfer from the Si-Si bonds to the molecular species. The triplet spin state of the O_2 molecule narrows the channels for network incorporation. Indeed, molecules in the triplet spin state preferentially incorporate in the network in correspondence of the upper layer of the Si substrate. Negatively charged species spontaneously incorporate in the oxide network, at any distance from the interface. Their incorporation is often associated to the formation of network defects thereby confirming their ability to modify the network. After incorporation in the network, the dissociation and hence the oxidation of Si-Si bonds corresponds to barrierless processes. In particular, as in the case of the incorporation process, we find that dissociations requires either vanishing or very small energies. The energy required for crossing these barriers is provided by the energy gained during the incorporation process. These results support an oxidation kinetics entirely governed by the diffusion process. Indeed, the incorporation and dissociation processes occur in the vicinity of the Si(100)-SiO_2 interface and are nearly spontaneous. These results are consistent with (i) the experimental evidence of a layer-by-layer growth of the oxide [193], (ii) the accumulation of negative charge at the interface during growth [178], (iii) the occurrence of Si atoms in intermediate oxidation states within a few Si-O bond lengths from the Si substrate [49, 50] and (iv) the occurrence of oxygen exchange processes in a region near the Si(100)-SiO_2 interface [37].

Bibliography

[1] L.C. Feldman, E.P. Gusev, and E. Garfunkel, in *Fundamental Aspects of Ultrathin Dielectrics on Si-based Devices*, edited by E. Garfunkel *et al.* (Kluwer, Dordrecht, 1998), pp. 1–24.

[2] D.A. Muller, S. Moccio, F.H. Baumann, K. Evans-Lutterodt, and G. Timp, Nature **399**, 758 (1999).

[3] M.L. Green, E.P. Gusev, R. Degraeve, and E.L. Garfunkel, J. Appl. Phys. **90**, 2057 (2001).

[4] M. Schulz, Nature **399**, 729 (1999).

[5] E.A. Irene, Critical Rev. in Solid State and Mat. Sci. **14**, 175 (1988).

[6] B.E. Deal and A.S. Grove, J. Appl. Phys. **36**, 3770 (1965).

[7] F. Rochet, S. Rigo, M. Froment, C. d'Anterroches, C. Maillot, H. Roulet, and G. Dufour, Adv. Phys. **35**, 237 (1986).

[8] A.M. Stoneham, C.R. Grovenor, and A. Cerezo, Philos. Mag. B **55**, 201 (1987).

[9] N.F. Mott, S. Rigo, F. Rochet, and A.M. Stoneham, Philos. Mag. B **60**, 189 (1989).

[10] N.F. Mott, Proc. R. Soc. Lond. A **376**, 207 (1981).

[11] A. Atkinson, Rev. Mod. Phys. **57**, 437 (1985).

[12] N.F. Mott, Philos. Mag. B **55**, 117 (1987).

[13] C.R. Helms and E.H. Poindexter, Rep. Prog. Phys. **57**, 791 (1994).

[14] I.J.R. Baumvol, Surf. Sci. Rep. **36**, 1 (1999).

[15] R. Ghez and Y.J. van der Meulen, J. Electrochem. Soc. **119**, 1100 (1972).

[16] M.A. Hopper, R.A. Clarke, and L. Young, J. Electrochem. Soc. **122**, 1216 (1975).

[17] H.Z. Massoud, J.D. Plummer, and E.A. Irene, J. Electrochem. Soc. **132**, 1745 (1985).

[18] F.J. Norton, Nature **191**, 701 (1961).

[19] A.J. Moulson and J.P. Roberts, Trans. Faraday Soc. **57**, 1208 (1961).

[20] A. Fargeix, G. Ghibaudo, and G. Kamarinos, J. Appl. Phys. **54**, 2878 (1983).

[21] P.J. Jorgensen, J. Chem. Phys. **37**, 874 (1962).

[22] A.G. Revesz and R.J. Evans, J. Phys. Chem. Solids **30**, 551 (1969).

[23] E.P. EerNisse, Appl. Phys. Lett. **30**, 290 (1977).

[24] E.P. EerNisse, Appl. Phys. Lett. **35**, 8 (1979).

[25] E. Kobeda and E.A. Irene, J. Vac. Sci. Technol. B **5**, 15 (1987).

[26] J. Blanc, Appl. Phys. Lett. **33**, 424 (1978).

[27] E.A. Irene, Appl. Phys. Lett. **40**, 74 (1982).

[28] L. Verdi and A. Miotello, Phys. Rev. B **51**, 5469 (1995).

[29] S. Dimitrijev and H.B. Harrison, J. Appl. Phys. **80**, 2467 (1996).

[30] K.-Y. Peng, L.-C. Wang, and J.C. Slattery, J. Vac. Sci. Technol. B **14**, 3316 (1996).

[31] D.R. Wolters and A.T.A. Zengers van Duijnhoven, Microelect. Reliab. **38**, 259 (1998).

[32] R.M.C. de Almeida, S. Gonçalves, I.J.R. Baumvol, and F.C. Stedile, Phys. Rev. B **61**, 12992 (2000).

[33] E. Rosencher, A. Straboni, S. Rigo, and G. Amsel, Appl. Phys. Lett. **34**, 254 (1979).

[34] F. Rochet, B. Agius, and S. Rigo, J. Electrochem. Soc. **131**, 914 (1984).

[35] J.A. Costello and R.E. Tressler, J. Electrochem. Soc. **131**, 1944 (1984).

[36] I. Trimaille and S. Rigo, Appl. Surf. Sci. **39**, 65 (1989).

[37] E.P. Gusev, H.C. Lu, T. Gustafsson, and E. Garfunkel, Phys. Rev. B **52**, 1759 (1995).

[38] H.C. Lu, T. Gustafsson, E.P. Gusev, and E. Garfunkel, Appl. Phys. Lett. **67**, 1742 (1995).

[39] J.-J. Ganem, I. Trimaille, P. Andrè, S. Rigo, F.C. Stedile, and J.R. Baumvol, J. Appl. Phys. **81**, 8109 (1997).

[40] T. Åkermark, L.G. Gosset, J.-J. Ganem, I. Trimaille, and S. Rigo, J. Electrochem. Soc. **146**, 3389 (1999).

[41] I.J.R. Baumvol, C. Krug, F.C. Stedile, F. Gorris, and W.H. Schulte, Phys. Rev. B **60**, 1492 (1999).

[42] A. Pasquarello, M.S. Hybertsen, and R. Car, Nature **396**, 58 (1998).

[43] Y. Tu and J. Tersoff, Phys. Rev. Lett. **89**, 086102 (2002).

[44] A. Pasquarello and M.S. Hybertsen, in *The Physics and Chemistry of* SiO_2 *and the Si-*SiO_2 *Interface*, edited by H.Z. Massoud, I.J.R. Baumvol, M. Hirose, and E.H. Poindexter (Electrochemical Soc., Pennington, 2000), Vol. 4, p. 271.

[45] F.L. Galeener and J.C. Mikkelsen, Solid State. Commun. **37**, 719 (1981).

[46] S.V. King, Nature **213**, 1112 (1967).

[47] P.J. Grunthaner, M.H. Hecht, F.J. Grunthaner, and N.M. Johnson, J. Appl. Phys. **61**, 629 (1987).

[48] F.J. Himpsel, F.R. McFeely, A. Taleb-Ibrahimi, J.A. Yarmoff, and G. Hollinger, Phys. Rev. B **38**, 6084 (1988).

[49] F. Rochet, Ch. Poncey, G. Dufour, H. Roulet, C. Guillot, and F. Sirotti, J. of Non-Crystal. Solids **216**, 148 (1997).

[50] J.H. Oh, H.W. Yeom, Y. Hagimoto, K. Ono, M. Oshima, N. Hirashita, M. Nywa, and A. Toriumi, Phys. Rev. B **63**, 205310 (2001).

[51] A. Pasquarello, M.S. Hybertsen, and R. Car, Phys. Rev. Lett. **74**, 1024 (1995).

[52] A. Pasquarello, M.S. Hybertsen, and R. Car, Phys. Rev. B **53**, 10942 (1996).

[53] N. Awaji, S. Ohkubo, T. Nakanishi, Y. Sugita, K. Takasaki, and S. Komiya, Jpn. J. Appl. Phys. **35**, L67 (1996).

[54] S.D. Kosowsky, P.S. Pershan, K.S. Krish, J. Bevk, M.L. Green, D. Brasen, L.C. Feldman, and P.K. Roy, Appl. Phys. Lett. **70**, 3119 (1997).

[55] S.T. Pantelides and M. Long, in *The Physics of* SiO_2 *and its Interfaces*, edited by S.T. Pantelides (Pergamon, New York, 1978), p. 339.

[56] I. Ohdomari, H. Akatsu, Y. Yamakoshi, and K. Koshimoto, J. Appl. Phys. **62**, 3751 (1987).

[57] T. Watanabe and I. Ohdomari, Thin Solid Films **343-344**, 370 (1999).

[58] K.-O. Ng and D. Vanderbilt, Phys. Rev. B **59**, 10132 (1999).

[59] Y. Tu and J. Tersoff, Phys. Rev. Lett. **84**, 4393 (2000).

[60] M.P. Allen and D.J. Tildesley, *Computer Simulation of Liquids* (Oxford University Press, Oxford, 1987).

[61] S. Tyagi, M. Alavi, R. Bigwood, T. Bramblett, J. Branderburg, W. Chen, M. Hussein, P. Jacob, C. Kenyon, C. Lo, B. Mcintyre, Z. Ma, P. Moon, P. Nguyen, L. Rumaner, R. Schweinfurth, S. Sivakumar, M. Stettler, S. Thompson, B. Tufts, J. Xu, S. Yang, and M. Bohr, Tech. Dig. - Int. Electron Devices Meet. **2000**, 567 (2000).

[62] A.C. Diebold, D. Venables, Y. Chabal, D. Muller, M. Weldon, and E. Garfunkel, Mat. Sci. Semic. Proc. **2**, 103 (1999).

[63] S.C. Witczak, J.S. Suehle, and M. Gaitan, Solid-State Electron. **35**, 345 (1992).

[64] A. Stesmans and V.V. Afanas'ev, J. Phys.: Condens. Matter **10**, L19 (1998).

[65] Z.H. Lu, M.J. Graham, D.T. Jiang, and K.H. Tan, Appl. Phys. Lett. **63**, 2941 (1993).

[66] R. Buczko, S.J. Pennycook, and S.T. Pantelides, Phys. Rev. Lett. **84**, 943 (2000).

[67] T. Yamasaki, C. Kaneta, T. Uchiyama, T. Uda, and K. Terakura, Phys. Rev. B **63**, 115314 (2001).

[68] M. Hane, Y. Miyamoto, and A. Oshiyama, Phys. Rev. B **41**, 12637 (1990).

[69] A.A. Demkov and O.F. Sankey, Phys. Rev. Lett. **83**, 2038 (1999).

[70] B.W.H. van Beest, G.J. Kramer, and R.A. van Santen, Phys. Rev. Lett. **64**, 1955 (1990).

[71] P. Vashishta, R.K. Kalia, J.P. Rino, and I. Ebbsjö, Phys. Rev. B **41**, 12197 (1990).

[72] A. Pasquarello, K. Laasonen, R. Car, C. Lee, and D. Vanderbilt, Phys. Rev. Lett. **69**, 1982 (1992).

[73] K. Laasonen, A. Pasquarello, R. Car, C. Lee, and D. Vanderbilt, Phys. Rev. B **47**, 10142 (1993).

[74] A. Bongiorno and A. Pasquarello, Phys. Rev. B **62**, R16326 (2000).

[75] A. Dal Corso, A. Pasquarello, A. Baldereschi, and R. Car, Phys. Rev. B **53**, 1180 (1996).

[76] D. Vanderbilt, Phys. Rev. B **41**, 7892 (1990).

[77] J.P. Perdew and Y. Wang, Phys. Rev. B **46**, 12947 (1992).

[78] R. Car and M. Parrinello, Phys. Rev. Lett. **55**, 2471 (1985).

[79] D.R. Hamann, Phys. Rev. B **61**, 9899 (2000).

[80] A. Pasquarello, M.S. Hybertsen, and R. Car, Appl. Phys. Lett. **68**, 625 (1996).

[81] A. Pasquarello, M.S. Hybertsen, and R. Car, Appl. Surf. Sci. **104/105**, 317 (1996).

[82] F. Mauri, A. Pasquarello, B.G. Pfrommer, Y.G. Yoon, and S.G. Louie, Phys. Rev. B **62**, 4786 (2000).

[83] L.C. Feldman, P.J. Silverman, J.S. Williams, T.E. Jackman, and I. Stensgaard, Phys. Rev. Lett. **41**, 1396 (1978).

[84] T.E. Jackman, J.R. MacDonald, L.C. Feldman, P.J. Silverman, and I. Stensgaard, Surf. Sci. **100**, 35 (1980).

[85] L.C. Feldman, Critical Reviews in Solid State and Materials Science **10**, 143 (1981).

[86] L.C. Feldman, J.W. Mayer, and S.T. Picraux, in *Materials analysis by ion channeling*, edited by L.C. Feldman (Academic press, Inc., New York, 1982).

[87] J.F. Van der Veen, Surf. Sci. Rep. **5**, 199 (1985).

[88] I. Stensgaard, L.C. Feldman, and P.J. Silverman, Surf. Sci. **77**, 513 (1978).

[89] N.W. Cheung, L.C. Feldman, P.J. Silverman, and I. Stensgaard, Appl. Rev. Lett. **35**, 859 (1979).

[90] I. Stensgaard, L.C. Feldman, and P.J. Silverman, Surf. Sc. **102**, 1 (1981).

[91] R.J. Culbertson, L.C. Feldman, and P.J. Silverman, Phys. Rev. Lett. **45**, 2043 (1980).

[92] R.J. Culbertson, L.C. Feldman, and P.J. Silverman, J. Vac. Sci. Technol. **20**, 868 (1982).

[93] R. Haight and L.C. Feldman, J. Appl. Phys. **53**, 4884 (1982).

[94] P.A. Bennett, L.C. Feldman, Y. Kuk, E.G. McRae, and J.E. Rowe, Phys. Rev. B **28**, R3656 (1983).

[95] R.J. Culbertson, Y. Kuk, and L.C. Feldman, Surf. Sci. **167**, 127 (1986).

[96] F.C. Stedile, I.J.R. Baumvol, I.F. Oppenheim, I. Trimalle, J.-J. Ganem, and S. Rigo, Nucl. Instr. and Meth. in Phys. Res. B **118**, 493 (1996).

[97] H. Yamada, J. Vac. Sci. Technol. A **19**, 627 (2001).

[98] H. Yamada, J. Appl. Phys. **91**, 1108 (2002).

[99] D.S. Gemmell, Rev. Mod. Phys. **46**, 129 (1974).

[100] J.H. Barrett, Phys. Rev. B **3**, 1527 (1971).

[101] M.T. Robinson and I.M. Torrens, Phys. Rev. B **9**, 5008 (1974).

[102] O.B. Firsov, Sov. Phys. JEPT **6**, 534 (1958).

[103] J.H. Barrett and D.P. Jackson, Nucl. Instrum. Methods **170**, 115 (1980).

[104] O.S. Oen, Nucl. Instr. and Meth. **194**, 87 (1982).

[105] O.S. Oen, in *Proc. 7th Intern. Conf. on Atomic Collisions in Solids*, edited by Y.V. Bulgakov and A.F. Tulinov (Moscow State University Publishing Hause, Moscow, 1981), Vol. 2, p. 124.

[106] C. Flensburg and R.F. Stewart, Phys. Rev. B **60**, 284 (1999).

[107] P.P. Pronko, B.R. Appleton, O.W. Holland, and S.R. Wilson, Phys. Rev. Lett. **43**, 779 (1979).

[108] J.H. Barrett, B.R. Appleton, and O.W. Holland, Phys. Rev. B **22**, 4180 (1980).

[109] O.H. Crawford, Phys. Rev. Lett. **44**, 185 (1980).

[110] M.M. Jakas and R.A. Baragiola, Phys. Rev. Lett. **44**, 424 (1980).

[111] B.R. Appleton, O.W. Holland, and J.H. Barrett, Nucl. Instr. and Meth. **191**, 507 (1981).

[112] O.W. Holland and J.H. Barrett, Phys. Rev. B **35**, 6495 (1987).

[113] J.H. Barrett, O.S. Oen, and O.W. Holland, Phys. Rev. B **43**, 2471 (1991).

[114] H. Ellmer, W. Fisher, A. Klose, and D. Semrad, Phys. Rev. B **55**, 2867 (1997).

[115] J.E. Northrup, Phys. Rev. B **44**, 1419 (1991).

[116] M. Copel, R.J. Culbertson, and R.M. Tromp, Appl. Phys. Lett. **65**, 2344 (1994).

[117] P.N. Keating, Phys. Rev. **145**, 637 (1966).

[118] A. Pasquarello, Phys. Rev. B **61**, 3951 (2000).

[119] I. Polishchuk and C. Hu, Symposium on VLSI Circuits, Digest of Technical Papers **2001**, 51 (2001).

[120] N.D. Arora and L.M. Richardson, in *VLSI Electronic Microstructure Science*, edited by N.G. Einspruch and G.S. Gildenblat (Academic Press, San Diego, 1989), Vol. 18, p. 237.

[121] W.G. Perkins and D.R. Begal, J. Chem. Phys. **54**, 1683 (1971).

[122] T. Åkermark, J.-J. Ganem, I. Trimaille, I. Vickridge, and S. Rigo, J. Phys. Chem. B **103**, 9910 (1999).

[123] T. Åkermark, J. Electrochem. Soc. **147**, 1882 (2000).

[124] N.F. Mott, Philos. Mag. A **45**, 323 (1982).

[125] A.G. Revesz and H.A. Schaeffer, J. Electrochem. Soc. **129**, 357 (1982).

[126] D.R. Hamann, Phys. Rev. Lett. **81**, 3447 (1998).

[127] M.A. Szymanski, A.M. Stoneham, and A.L Shluger, Microelect. Reliab. **40**, 567 (2000).

[128] J.R. Chelikowsky, D.J. Chadi, and N. Binggeli, Phys. Rev. B **62**, 2251 (2000).

[129] G. Roma, Y. Limoge, and S. Baroni, Phys. Rev. Lett. **86**, 4564 (2001).

[130] W. Orellana, A.J.R. da Silva, and A. Fazzio, Phys. Rev. Lett. **87**, 155901 (2001).

[131] M.A. Szymanski, A.L. Shluger, and A.M. Stoneham, Phys. Rev. B **63**, 224207 (2001).

[132] A.M. Stoneham, M.A. Szymanski, and A.L. Shluger, Phys. Rev. B **63**, R241304 (2001).

[133] A. Bongiorno and A. Pasquarello, Microelect. Reliab. **59**, 167 (2001).

[134] Y. Jin and K.J. Chang, Phys. Rev. Lett. **86**, 1793 (2001).

[135] T. Bakos, S.N. Rashkeev, and S.T. Pantelides, Phys. Rev. Lett. **88**, 55508 (2002).

[136] K. Vollmayr, W. Kob, and K. Binder, Phys. Rev. B **54**, 15808 (1996).

[137] R.L. Mozzi and B.E. Warren, J. Appl. Crystallogr. **2**, 164 (1969).

[138] S. Susman, K.J. Volin, D.L. Price, M. Grimsditch, J.P. Rino, R.K. Kalia, P. Vashishta, G. Gwanmesia, Y. Wang, and R.C. Liebermann, Phys. Rev. B **43**, 1194 (1991).

[139] J.P. Rino, I. Ebbsjö, R.K. Kalia, A. Nakano, and P. Vashishta, Phys. Rev. B **47**, 3053 (1993).

[140] P. Umari, X. Gonze, and A. Pasquarello, Phys. Rev. Lett. **90**, 027401 (2003).

[141] D.O. Raleigh, J. Electrochem. Soc. **113**, 782 (1966).

[142] P.J. Jorgensen, J. Electrochem. Soc. **114**, 820 (1967).

[143] D.O. Raleigh, J. Electrochem. Soc. **115**, 111 (1968).

[144] D.N. Modlin and W.A. Tiller, J. Electrochem. Soc. **132**, 1659 (1985).

[145] P. Hohenberg and W. Kohn, Phys. Rev. **9**, B864 (1964).

[146] W. Kohn and L.J. Sham, Phys. Rev. **15**, A1133 (1965).

[147] D.R. Hamann, Phys. Rev. Lett. **76**, 660 (1996).

[148] J.P. Perdew, J.A. Chevary, S.H. Vosko, K.A. Jackson, M.R. Pederson, D.J. Singh, and Carlos Fiolhais, Phys. Rev. B **46**, 6671 (1992).

[149] K. Kato, T. Uda, and K. Terakura, Phys. Rev. Lett. **80**, 2000 (1998).

[150] *CRC Handbook of Chemistry and Physics*, edited by D. R. Lide and H.P.R. Frederikse (CRC Press, New York, 1998).

[151] Andrea Trave, Ph.D. thesis, Geneva, 2001.

[152] J. Sarnthein, A. Pasquarello, and R. Car, Phys. Rev. Lett. **74**, 4682 (1995).

[153] J. Sarnthein, A. Pasquarello, and R. Car, Phys. Rev. B **52**, 12690 (1995).

[154] V.A. Luchnikov, N.N. Medvedev, A. Appelhagen, and A. Geiger, Mol. Phys. **88**, 1337 (1996).

[155] M. Wilson and P.A. Madden, Phys. Rev. Lett. **80**, 532 (1998).

[156] C. Massobrio and A. Pasquarello, J. Chem. Phys. **114**, 7976 (2001).

[157] M. Benoit and W. Kob, Europhys. Lett. **60**, 269 (2002).

[158] G.T. Barkema and N. Mousseau, Phys. Rev. Lett. **77**, 4358 (1996).

[159] M.J.S. Dewar, E.F. Healy, and J.J.P. Stewart, J. Chem. Soc. Faraday Trans. **80**, 227 (1984).

[160] Federick Reif, in *Fundamentals of statistical and thermal physics*, edited by E.U. Condon (McGraw-Hill, iSingapore, 1965).

[161] B. Guillot and Y. Guissani, J. Chem. Phys. **105**, 255 (1996).

[162] R. Kirchheim, J. Am. Ceram. Soc. **84**, 2699 (2001).

[163] P.L. Studt and J.F. Shackelford R.M. Fulrath, J. Appl. Phys. **41**, 2777 (1970).

[164] J.F. Shackelford, P.L. Studt, and R.M. Fulrath, J. Appl. Phys. **43**, 1619 (1972).

[165] A.F. Voter, Phys. Rev. Lett. **63**, 167 (1989).

[166] G.H. Vineyard, J. Phys. Chem. Solids **3**, 121 (1957).

[167] N. Metropolis, A.W. Rosenbluth, M.N. Rosenbluth, A.H. Teller, and E. Teller, J. Chem. Phys. **21**, 1087 (1953).

[168] B. Roling, Phys. Rev. B **61**, 5993 (2000).

[169] J.W. Haus and K.W. Kehr, Phys. Rep. **150**, 263 (1987).

[170] E.L. Williams, J. Am. Ceram. Soc. **48**, 190 (1965).

[171] H.A. Schaeffer, J. Non-Cryst. Solids **38**, 545 (1980).

[172] M.A. Lamkin and F.L Riley, J. Eur. Ceram. Soc. **10**, 347 (1992).

[173] A. Bongiorno and A. Pasquarello, Phys. Rev. Lett. **88**, 125901 (2002).

[174] L. Verdi, A. Miotello, and R. Kelly, Thin Solid Films **241**, 383 (1994).

[175] R.A.B. Devine, J.J. Capponi, and J. Arndt, Phys. Rev. B **35**, 770 (1987).

[176] Y. Inamura, M. Arai, N. Kitamura, S.M. Bennington, and A.C. Hannon, Physica B **241**, 903 (1998).

[177] D. Stauffer, *Introduction to Percolation Theory* (Taylor & Francis, London, 1985).

[178] J. Wang, P. Roman, E. Kamieniecki, and J. Ruzyllo, Electrochem. Solid-State Lett. **6**, G63 (2003).

[179] A. Stockhausen, T.U. Kampen, and W. Mönch, Appl. Surf. Sci. **56**, 795 (1992).

[180] J. Westermann, H. Nienhaus, and W. Mönch, Surf. Sci. **311**, 101 (1994).

[181] H. Kageshima and K. Shiraishi, Phys. Rev. Lett. **81**, 5936 (1998).

[182] Y. Miyamoto and A. Oshiyama, Phys. Rev. B **41**, 12680 (1990).

[183] Y. Miyamoto and A. Oshiyama, Phys. Rev. B **43**, 9287 (1991).

[184] B.B. Stefanov and K. Raghacachari, Surf. Sci. **389**, L1159 (1997).

[185] K. Kato and T. Uda, Phys. Rev. B **62**, 15978 (2000).

[186] Y.J. Chabal, K. Raghavachari, X. Zhang, and E. Garfunkel, Phys. Rev. B **66**, 161315 (2002).

[187] Y. Widjaja and C.B. Musgrave, J. Chem. Phys. **116**, 5774 (2002).

[188] W. Orellana, A.J.R. da Silva, and A. Fazzio, Phys. Rev. Lett. **90**, 16103 (2003).

[189] V.V. Afanas'ev, Microelect. Eng. **48**, 241 (1999).

[190] G. Markov and M.C. Payne, Phys. Rev. B **51**, 4014 (1995).

[191] F. Tassone, F. Mauri, and R. Car, Phys. Rev. B **50**, 10561 (1994).

[192] A. Bongiorno and A. Pasquarello, Mat. Sci. Eng. B **96**, 102 (2002).

[193] H. Watanabe, K. Kato, T. Uda, K. Fujita, M. Ichikawa, T. Kawamura, and K. Terakura, Phys. Rev. Lett. **80**, 345 (1998).

Acknowledgements

This thesis work would not have been possible without the help and support of many people. First of all I am grateful to Professor Alfredo Pasquarello who gave me the opportunity to become a Ph.D. student at IRRMA. He was always an inspiring source during the scientific discussions. Without his experience and guidance the works presented in this thesis would not have reached such a scientific level. I am also grateful to Professor Alfonso Baldereschi, who gave me the opportunity to practice teaching and for the his scientific supervision through the years spent at IRRMA. Special thanks go also to Carol Bonzon and Suzanne Claudet. A special thank goes to L.C. Feldman and Mark S. Hybertsen. It has been a pleasure to work with you. Moreover, I am also thankful to all the people met at IRRMA during these last four years, here listed in alphabetic order: Jerome Bürki, Giovanni Cangiani, Alessandro De Vita, Stéphane Dommange, Vincent Dubois, Reiner Härle, Luigi Giacomazzi, Paolo Giannozzi, Feliciano Giustino, John Karadamoglou, Thomas Maxisch, Carlo Massobrio, Felix Naef, Tatsuki Oda, Gian-Marco Rignanese, Claudia Sgiarovello, Alain Sewer, Zeljko Sljivancanin, Massimiliano Stengel, Federica Trudu, Paolo Umari, Matthieu Vertraete, Mascha Vladimirova, Xenophon Zotos. Last, but certainty not least, the biggest thank you goes to my wife Elisa, to whom also I dedicate my thesis.

Curriculum Vitae

First/Last name	Angelo Bongiorno
Date/Place of birth	August 10th 1970 , Milan (Italy)
Work address	Institut de Théorie des Phénomènes Physiques (ITP), Institut Romand de Recherche Numérique en Physique des Matériaux (IRRMA), Ecole Polytechnique Fédérale de Lausanne (EPFL), CH-1015 Lausanne, Switzerland. Tel.: +41 21 6934600. Fax : +41 21 6936655.
E-mail	Angelo.Bongiorno@epfl.ch

1999−2003	Ph.D. in Physics at the Ecole Polytechnique Fédérale de Lausanne (EPFL), Lausanne, Switzerland. Dissertation: *Simulation of atomistic processes during silicon oxidation.*
1998−1999	Employed by TAU Controllo processi S.p.A., Via Tortona 33, Milan, Italy.
1996−1998	Master degree in Material Science and Technology. University of Milan, Milan, Italy. Dissertation: *Aggregation and interaction of native defects in silicon.* Honors: 70/70 *cum laude.*
1995−1996	Civil service in Bologna, Italy.
1989−1995	Diploma thesis in Physics. University of Milan, Milan, Italy. Dissertation: *Simulation of the hydrogen diffusion process in* SiO_2 *by molecular dynamics.* Honors: 110/110 *cum laude.*

List of publications

Peer-reviewed articles in scientific journals

Angelo Bongiorno, Alfredo Pasquarello, Mark S. Hybertsen and L. C. Feldman, *Transition structure at the Si(100)-SiO_2 interface*, Phys. Rev. Lett., **90** 186101 (2003).

Angelo Bongiorno and Alfredo Pasquarello, *Dependence of the O_2 diffusion rate on oxide thickness during silicon oxidation*, J. Phys.: Condens. Matter, **15**, S1553 (2003).

Feliciano Giustino, Angelo Bongiorno and Alfredo Pasquarello, *Si 2p-core-level shift at the Si(100)-$Zr_xSi_{1-x}O_2$ interface*, Appl. Phys. Lett., **81**, 4233 (2002).

Angelo Bongiorno and Alfredo Pasquarello, *Energetics of oxygen species in crystalline and amorphous SiO_2: A first-principles investigation*, Solid State Electron., **46**, 1873 (2002).

Angelo Bongiorno and Alfredo Pasquarello, *Atomic structure at the Si(001)-SiO_2 interface: From the interpretation of Si 2p core-level shifts to a model structure*, Mater. Sci Eng. B, **96**, 102 (2002).

G.-M. Rignanese, F. Detraux, X. Gonze, Angelo Bongiorno, and Alfredo Pasquarello, *Dielectric constants of Zr silicates: A first-principles study*, Phys. Rev. Lett. **89**, 117601 (2002).

Angelo Bongiorno and Alfredo Pasquarello, *Oxygen diffusion through the disordered oxide network during silicon oxidation*, Phys. Rev. Lett. **88**, 125901 (2002).

Angelo Bongiorno and Alfredo Pasquarello, *Oxygen species in SiO_2: a first-principles investigation*, Microelect. Eng. **59**, 167 (2001).

Angelo Bongiorno and Alfredo Pasquarello, *Validity of the bond-energy picture for the energetics at Si-SiO*$_2$ *interfaces*, Phys. Rev. B **62**, R16326 (2000).

Angelo Bongiorno, L. Colombo, F. Cargnoni, C. Gatti, and M. Rosati, *Evolution of energetics and bonding of compact self-interstitial clusters in Si*, Europhys. Lett. **50**, 608 (2000).

Angelo Bongiorno, L. Colombo, T.D. De la Rubia, *Structural and binding properties of vacancy clusters in silicon*, Europhys. Lett. **43**, 695 (1998).

Angelo Bongiorno and L. Colombo, *Interaction between a monovacancy and a vacancy cluster in silicon*, Phys. Rev. B **57**, 8767 (1998).

M.I. Trioni, Angelo Bongiorno and L. Colombo, *Structural properties of silica surface: A classical molecular dynamics study*, J. Non-Cryst. Solids **200**, 164 (1997).

Angelo Bongiorno, L. Colombo and M.I. Trioni *Migration of atomic hydrogen in crystalline and amorphous SiO*$_2$*: a molecular dynamics study*, J. Non-Cryst. Solids **216**, 30 (1997).

L. Colombo and Angelo Bongiorno, *Modelling point defects diffusion and interaction in silicon: The tight-binding molecular dynamics approach*, Ber. Bunsen. Phys. Chem. *101*, 1211 (1997).

Angelo Bongiorno and L. Colombo, Migration of atomic hydrogen in SiO$_2$: A molecular dynamics study, Ber. Bunsen. Phys. Chem. **101**, 1229 (1997).

Angelo Bongiorno, L. Colombo and F. Cargnoni, *Hydrogen diffusion in crystalline SiO*$_2$, Chem. Phys. Lett. **264**, 435 (1997).

Conference proceedings

Angelo Bongiorno and Alfredo Pasquarello, *Atomic processes during silicon oxidation: Oxygen diffusion through the oxide layer*, ICPS 2002.

Angelo Bongiorno and Alfredo Pasquarello, *New evidence for reconstruction at the Si(100)-*SiO_2 *interface from analysis of ion scattering*, ICPS 2002.

Angelo Bongiorno and Alfredo Pasquarello, *Oxygen species in amorphous* SiO_2*: Relative energetics and concentration of equilibrium sites*, in *Alternatives to* SiO_2 *as Gate Dielectrics for Future Si-Based Microelectronics*, edited by J. Morais and I.J.R. Baumvol, MRS Workshop Series (Material Research Society, 2001), p. 31.

Angelo Bongiorno and L. Colombo, *Hydrogen diffusion in quartz: a molecular dynamics investigation*, Material Research Symposium Proceedings, **408**, 515 (1996).

Angelo Bongiorno and L. Colombo, *Formation and binding energies of vacancy clusters in silicon*, Material Research Symposium Proceedings, **469**, 205 (1997).